NUCLEATION AND GROWTH OF ATMOSPHERIC NANOPARTICLES AT MOLECULAR SCALE

A Dissertation

by

WEN XU

Submitted to the Office of Graduate and Professional Studies
Texas A&M University
in partial fulfillment of the requirements for the degree of

DOCTOR OF PHILOSOPHY

Chair of Committee, Renyi Zhang
Committee Members, Robert R. Lucchese
Simon W. North
Sarah D. Brooks
Head of Department, David H. Russell

May 2014

Major Subject: Chemistry

ABSTRACT

Atmospheric aerosols are fine liquid droplets or solid particles of various chemical compositions suspended in the air. They influence the Earth radiation budget, impact cloud formation, cause or enhance diseases on humans, and change photochemical chemistry and partitioning of trace gas species. Atmospheric aerosols are classified into two categories, primary and secondary, on the basis of their formation mechanisms. Although a large portion of atmospheric aerosols is secondary, the mechanisms for secondary aerosol formation remain highly uncertain, preventing the development of physically based representations of their formation in atmospheric models. So far it is known that secondary aerosol formation consists two consecutive steps, nucleation to form critical nucleus and subsequent growth of freshly nucleated nanoparticles. Unfortunately, our current knowledge of these two steps is very limited.

In the current study, the dicarboxylic acids (organic acid) assisted nucleation is investigated both experimentally and theoretically. First, nucleation and partitioning theories are presented as the theoretical framework for data analysis and explanation. Subsequently, quantum chemistry calculations are performed to evaluate the hydrogen bonding strength of dicarboxylic acids with common atmospheric nucleation precursors, including sulfuric acid, water, ammonia, and amines. Then, succinic acid (dicarboxylic acid) assisted nucleation experiment is carried out to assess the nucleation enhancement ability of dicarboxylic acids. Next, the growth contributions from epoxides vapors are determined using a combination of Nano-tandem differential mobility analyzer (n-TDMA) and thermo desorption ion drift chemical ionization mass spectrometer (TD-ID-CIMS). Finally, the hygroscopicity and CCN properties of atmospheric polymers are characterized.

Our results show that dicarboxylic acids bind strongly with sulfuric acid and enhance nucleation rate by 5-13 times with a concentration of 1 ppb. Dicarboxylic acids also react with amines under hydration to form non-volatile aminium carboxylate ion pairs, which contribute to nanoparticles growth. The n-TDMA and TD-ID-CIMS results show that epoxides contribute to freshly nucleated nanoparticle (sulfuric acid nanoparticles) growth through forming non-volatile organosulfates and oligomers, which subsequently changes the cloud-forming properties of aerosols.

DEDICATION

This dissertation is dedicated to my family: my wife, Huan.

ACKNOWLEDGEMENTS

I would like to thank my advisor, Dr. Renyi Zhang, for his support and guidance throughout my Ph.D. studies. I wish to thank my committee members, Dr. Robert R. Lucchese, Dr. Simon W. North, and Dr. Sarah D. Brooks for their helpful comments and discussions.

I also want to thank my former colleagues, Drs. Lin Wang, Jun Zheng, Chong Qiu, and Yuan Wang for their generous help and teamwork. Thanks also to my current group members, Dr. Song Guo, Mr. Mario Gomez, Mr. Yun Lin, Ms. Misti Levy, Mr. Jeremiah Secrest, Ms. Brittany Turner, and Ms. Li Shen. Special thanks to Dr. Alexei F. Khalizov, who helped me in building particle size magnifier and gave me much help with my dissertation research. Thanks to Dr. Don Collins and Mr. Nathan Taylor for letting me use their h-TDMA and CCN, and teaching me how to use these instruments. Thanks to the staff in glass shop and machine shop in Chemistry and electronics shop in Physics for their help. Thanks to Dr. Lisa Perez for her help on Quantum Chemistry calculations. I would also like to thank the departmental office staff in both Chemistry and Atmospheric Science for helping me with both academic and non-academic stuff and making my study a happy journey at Texas A&M.

I am thankful to my wife, Huan, for her support and patience during my study.

The author also acknowledges financial support from Robert A. Welch Foundation (Grant A-1417) and the US National Science Foundation (AGS-0938352) and additional support from the Texas A&M University Supercomputing Facilities and the use of the Laboratory for Molecular Simulations at Texas A&M University.

TABLE OF CONTENTS

Page

LIST OF FIGURES

Page

LIST OF TABLES

Page

1. INTRODUCTION

1.1 Overview of nucleation theory

1.1.1 Classical nucleation theory

Nucleation is a non-equilibrium process in which the system undergoes a phase transition from a metastable state to a stable state. Homogeneous gas phase nucleation is an important way of forming atmospheric nanoparticles from various gas phase species in the atmosphere. Due to its non-equilibrium nature, nucleation is not so well understood as other equilibrium processes, such as partitioning. The theoretical research on nucleation can be traced back to the pioneering work by Volmer and Weber,[1] Becker and Döring,[2] Frenkel,[3] and Zeldovich[4] in the early 1920-1940s. Based on their theory, the rate of nucleation is described by an Arrhenius type of equation (1.1),

$$J = J_0 e^{-\beta \Delta G^*} \tag{1.1}$$

where J is the nucleation rate; J_0 is the pre-factor (the expression of J_0 as function of molecular properties can be found latter in the chapter); ΔG^* is the Gibbs free energy change of critical nuclei formation; β is the inverse temperature.

The value of ΔG^* can be derived from the following procedure. Generally, the formation of a cluster (A_n) containing n monomers from isolated n monomers (A_1) can be expressed as the following reaction scheme,

$$n\, A_1 = A_n \tag{R1}.$$

The Gibbs free energy change of (R1) is composed of two parts, bulk and surface contributions, which can be expressed as the following equation (1.2),

$$\Delta G(n) = -n(\mu_g - \mu_l) + \sigma_n S_n \tag{1.2}$$

where $\Delta G(n)$ is Gibbs free energy change of R1; μ_g and μ_l are the chemical potential of A_1 in gas phase and liquid phase, respectively; σ_n is the surface tension of cluster A_n; S_n is the surface area of cluster A_n. Assuming a spherical shape for the cluster A_n and within the capillary approximation, the following equations hold,

$$\sigma_n \equiv \sigma \tag{1.3.a}$$

$$nv_0 = \frac{4}{3}\pi R_n^3 \tag{1.3.b}$$

$$S_n = 4\pi R_n^2 \tag{1.3.c}$$

where σ is the surface tension of a flat surface; R_n is the radius of cluster A_n; v_0 is the volume of monomer A_1. Substitute equation 1.3(a-c) into equation (1.2), one obtains equation (1.4).

$$\Delta G(n) = -n\Delta\mu_{g-l} + \sigma\left(36\pi {v_0}^2\right)^{\frac{1}{3}} n^{\frac{2}{3}} \tag{1.4}$$

Thus, the formation free energy of cluster A_n is a function of cluster size n.

It is shown in Figure 1.1 that there is a maximum of Gibbs free energy of formation ($\Delta G(n)$) along the size coordinate (n). Taking the derivative of equation (1.4) and setting it to zero, the cluster size n^* of maximum formation free energy can be easily obtained as shown in the following equations,

$$n^* = \frac{32\sigma^3\pi v_0^2}{3\Delta\mu_{g-l}^3} \tag{1.5a}$$

$$\Delta G^* = \frac{16\pi v_0^2\sigma^3}{3\Delta\mu_{g-l}^2} \tag{1.5b}$$

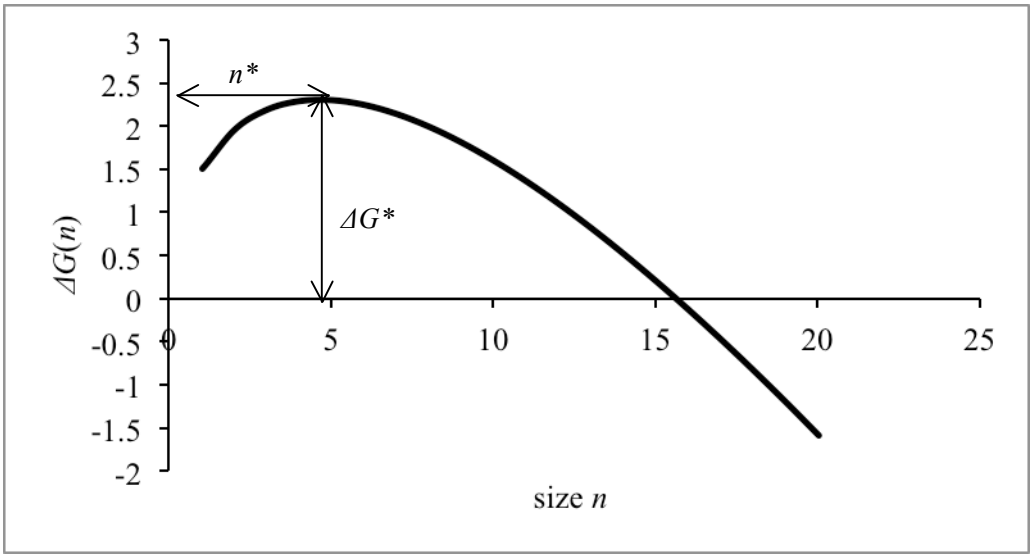

Figure 1.1. Plot of Gibbs free energy of formation against the cluster size

Taking the derivative of equation 1.5b with respect to $\Delta\mu_{g\text{-}l}$, the following equation can be obtained,

$$\frac{\partial \Delta G^*}{\partial \Delta \mu_{g-l}} = -\frac{32\pi v_0^2 \sigma^3}{3\Delta \mu_{g-l}^3} = -n^* \tag{1.6}$$

If J_0 is taken as a constant, combing equation (1.1) and (1.6), the following equation can be obtained,

$$\frac{\partial \ln J}{\partial \ln S} = -\frac{\partial(\beta \Delta G^*)}{\partial(\beta \Delta \mu_{g-l})} = n^* \tag{1.7}$$

where S denotes the supersaturation of the gas phase monomer A_1. The above equation (1.7) is commonly known as the first nucleation theorem.

1.1.2 Kinetic approach to obtain the pre-factor J_0

It is impossible to obtain the pre-factor J_0 only from the above thermodynamic procedure. The following procedure has been described extensively in the literature.[5-8] Considering

nucleation from monomers A_1, the cluster A_n can be formed either by collision induced growth of small clusters ($A_{i<n}$) or by fission of large clusters ($A_{i>n}$). Since collisions involving three body or above are rare in the gas phase, it is reasonable to assume that all the collisions forming cluster A_n are two-body collisions. In addition, in the gas phase the concentration of monomer *A1* is much larger than that of cluster $A_{i>1}$. As a result, the collision formation pathway of A_n can be further simplified as the collision between cluster A_{n-1} and A_1. If the major fission pathway of A_n is assumed to be the formation of A_{n-1} and A_1, the nucleation process can be denoted as the following reaction scheme (R2),

$$A_1 \Leftrightarrow A_2 \Leftrightarrow A_3 \Leftrightarrow A_4 \Leftrightarrow \ldots \Leftrightarrow A_{n-1} \Leftrightarrow A_n \Leftrightarrow A_{n+1} \Leftrightarrow \ldots \Leftrightarrow A_M \qquad \text{(R2)}.$$

The flux J_n away from size n can be expressed as the following equation on the basis of R2,

$$J_n = \alpha_n C_n - \gamma_{n+1} C_{n+1} \qquad (1.8)$$

where C_i is the concentration of cluster A_i; α_i is the collision coefficient α_i' times the monomer concentration C_1; γ_i is the evaporation coefficient of cluster A_i.

Assuming a constrained equilibrium is reached, the equation below holds,

$$0 = J_n = \alpha_n Z_n - \gamma_{n+1} Z_{n+1} \qquad (1.9)$$

where Z_n is the constrained equilibrium concentration of cluster A_n.

Combine equation (1.8) and (1.9),

$$J_n = \alpha_n C_n - \frac{\alpha_n Z_n}{Z_{n+1}} C_{n+1} = -\alpha_n Z_n \left(\frac{C_{n+1}}{Z_{n+1}} - \frac{C_n}{Z_n}\right) = -\alpha_n Z_n \frac{\partial}{\partial n}\left(\frac{C_n}{Z_n}\right) \qquad (1.10)$$

Appling the continuity equation and equation (1.10), the following equation holds,

$$\frac{\partial C_n}{\partial t} = J_{n-1} - J_n = -\frac{\partial J}{\partial n} = \frac{\partial}{\partial n}\left[\alpha_n Z_n \frac{\partial}{\partial n}\left(\frac{C_n}{Z_n}\right)\right] \qquad (1.11)$$

The above equation (1.11) is called Fokker Planck equation. Since nucleation is a non-equilibrium process, it is not surprising that it can be described by the Fokker Planck equation.

At steady state condition, the LHS of equation (1.11) is zero and $J_n \equiv J$ for every n. Substitute $J_n \equiv J$ into equation (1.10), divide both sides by $\alpha_n Z_n$ and integrate, then

$$J\int_0^M \frac{1}{\alpha_n Z_n} dn = \frac{C_0}{Z_0} - \frac{C_M}{Z_M} = 1 \tag{1.12}$$

The last equality in equation (1.12) utilizes the boundary conditions $C_0=Z_0$ and $C_M=0$. As a result, the steady state nucleation rate can be calculate using the following equation,

$$J = 1/\int_0^M \frac{1}{\alpha_n Z_n} dn \tag{1.13}$$

Based on equation (1.4) and Boltzmann distribution, Z_n can be calculated using equation (1.14)

$$Z_n = C_0 \exp[-\Delta G(n)/kT] \tag{1.14}$$

Since $\Delta G(n)$ has a maximum value at n^*, the integration in equation (1.13) can be approximated using the steepest decent method.

$$\begin{aligned} J = 1/\int_0^M \frac{1}{\alpha_n Z_n} dn &= 1/\int_0^M \frac{1}{\alpha_{n^*} C_0 \exp(-\beta \Delta G^*) \exp[-\frac{1}{2}\beta \frac{d^2 \Delta G(n^*)}{dn^{*2}}(n-n^*)^2]} dn \\ &= \alpha_{n^*} C_0 \exp(-\beta \Delta G^*) / \int_0^M \exp[\frac{1}{2}\beta \frac{d^2 \Delta G(n^*)}{dn^{*2}}(n-n^*)^2] dn \end{aligned} \tag{1.15}$$

Because $\frac{1}{2}\frac{d^2 \Delta G(n^*)}{dn^{*2}} < 0$, the integration on the RHS of equation (1.15) can be evaluated using the gamma function. Therefore,

$$J = \alpha_{n^*} C_0 \exp(-\beta \Delta G^*) Z \tag{1.16a}$$

$$Z = 1/\int_0^M \exp[\frac{1}{2}\beta \frac{d^2 \Delta G(n^*)}{dn^{*2}}(n-n^*)^2] dn = \frac{\sqrt{-1/2\beta \frac{d^2 \Delta G(n^*)}{dn^{*2}}}}{\Gamma(1/2)} \tag{1.16b}$$

where Z is the commonly known Zeldovich factor in honor of J. B. Zeldovich who obtained the expression in 1942. Comparing equation (1.16) with equation (1.1), the pre-exponential factor J_0 in (1.1) can be obtained.

$$J_0 = \alpha_{n^*} C_0 Z \tag{1.17}$$

Therefore, J can be expressed as the following equation,

$$J = \alpha_{n^*} C_0 Z \exp(-\beta \Delta G^*) = \varpi_{n^*} S C_{1,s} C_0 \exp(-\beta \Delta G^*) = \varpi_{n^*} S C_{1,s} Z_{n^*} \tag{1.18}$$

where ω_{n^*} is the collision rate; $C_{1,s}$ is the saturation concentration of monomer A_1. Since J_0 is not a constant with respect to lnS, the first nucleation theory in equation (1.7) must be modified accordingly.

$$\frac{\partial \ln J}{\partial \ln S} = -\frac{\partial(\beta \Delta G^*)}{\partial(\beta \Delta \mu_{g-l})} + \frac{\partial \ln J_0}{\partial \ln S} = n^* + 1 \tag{1.19}$$

Recently, a more accurate expression for nucleation rate J was obtained by solving the equations (1.10) and (1.11) accurately. Fortunately, the new expression for J does not change the expression for first nucleation theorem (1.19).

1.1.3 Nucleation theorem for multicomponent system

The theory for multicomponent nucleation can be obtained on the basis of generalizing the equations of mono-component nucleation.[8] The Fokker Planck equation (1.11) and Boltzmann distribution equation (1.14) still hold in multicomponent nucleation. The counterparts of (1.11) and (1.14) are shown in the following equations,

$$\frac{\partial C_{\mathbf{n}}}{\partial t} = -\nabla \mathbf{J} = \nabla[\boldsymbol{\alpha}_{\mathbf{n}} Z_{\mathbf{n}} \nabla(\frac{C_{\mathbf{n}}}{Z_{\mathbf{n}}})] \tag{1.20a}$$

$$Z_{\mathbf{n}} = C_0 \exp[-\Delta G(\mathbf{n}) / kT] \tag{1.20b}$$

where $\mathbf{n}=(n_1,n_2,\ldots,n_k)$ is the size space coordinate and $\nabla = \frac{\partial}{\partial \mathbf{n}}$. In equation (1.20a), $\boldsymbol{\alpha}_\mathbf{n}$ is a n×n diagonal matrix attributable to condensation. Equation (1.20b) can be expanded as a Taylor series at the saddle point ($\mathbf{n}^*$) of the Gibbs free energy of formation ($\Delta G(\mathbf{n})$). If only the first three terms are used, Z_n can be expressed as,

$$Z_\mathbf{n} = C_0 \exp[-\Delta G(\mathbf{n}^*)/kT - \frac{1}{2}\beta(\Delta\mathbf{n})^T \underline{\mathbf{G}}\Delta\mathbf{n}] \tag{1.21}$$

where $\Delta\mathbf{n}=\mathbf{n}-\mathbf{n}^*$, $\underline{\mathbf{G}}$ is the Hessian matrix of Gibbs free energy of formation at $\mathbf{n}^*$. Substitute (1.21) into (1.20a), we obtain (1.22)

$$\frac{\partial C_\mathbf{n}}{\partial t} = \nabla[\boldsymbol{\alpha}_{\mathbf{n}^*} \exp(-\frac{1}{2}\beta(\Delta\mathbf{n})^T \underline{\mathbf{G}}\Delta\mathbf{n})\nabla[\exp(\frac{1}{2}\beta(\Delta\mathbf{n})^T \underline{\mathbf{G}}\Delta\mathbf{n})C_\mathbf{n}] \tag{1.22}$$

After transformation by changing of variables from $\mathbf{n}$ to $\mathbf{v}$ according to the following equations,

$$\Delta\mathbf{n} = (\boldsymbol{\alpha}_{\mathbf{n}^*})^{1/2}\mathbf{v},\ \frac{\partial}{\partial \mathbf{n}} = (\boldsymbol{\alpha}_{\mathbf{n}^*})^{-1/2}\frac{\partial}{\partial \mathbf{v}},\ \boldsymbol{\Gamma} = ((\boldsymbol{\alpha}_{\mathbf{n}^*})^{1/2})^T \underline{\mathbf{G}}(\boldsymbol{\alpha}_{\mathbf{n}^*})^{1/2} \tag{1.23}$$

equation (1.22) can be written in the new coordinates $\mathbf{v}$.

$$\frac{\partial C_\mathbf{n}}{\partial t} = \frac{\partial}{\partial \mathbf{v}}[\exp(-\frac{1}{2}\beta\mathbf{v}^T\boldsymbol{\Gamma}\mathbf{v})\frac{\partial}{\partial \mathbf{v}}[\exp(\frac{1}{2}\beta\mathbf{v}^T\boldsymbol{\Gamma}\mathbf{v})C_\mathbf{n}] \tag{1.24}$$

Since $\boldsymbol{\Gamma}$ is a real symmetric matrix, it is diagonalizable and its eigenvalues are all real. It can be proved that $\boldsymbol{\Gamma}$ has and only has one negative eigenvalue and all the rest are positive due to the Hessian at saddle point. Assuming the negative eigenvalue is λ and the corresponding unit eigenvector pointing away from the origin is $\boldsymbol{\tau}$, equation (1.24) can be solved by separation of variables in the normal mode coordinate. At steady state the LHS of (1.24) equals 0. Therefore, in the direction of $\boldsymbol{\tau}$ from ($\mathbf{n}^*$), C_n and $\mathbf{J}_\mathbf{n}$ can be expressed as the following equations, respectively.

$$C_\mathbf{n} = C_\mathbf{0}\exp(-\beta\Delta G(\mathbf{n}^*))\exp(\frac{1}{2}|\lambda|\beta\xi^2)\sqrt{\frac{|\lambda|\beta}{2\pi}}\int_\xi^\infty \exp(-\frac{1}{2}|\lambda|\beta x^2)dx \tag{1.25a}$$

$$\mathbf{J_n} = C_0 \sqrt{\frac{|\lambda|\beta}{2\pi}} \exp(-\beta \Delta G(\mathbf{n}^*))(\boldsymbol{\alpha}_{\mathbf{n}^*})^{1/2} \boldsymbol{\tau} \qquad (1.25b)$$

In equation (1.25a), ξ is the coordinate in the direction of $\boldsymbol{\tau}$. Equation (1.25b) shows that the direction of nucleation past from the saddle point is different from the steepest decent direction proposed by Reiss *et al.*, since $\mathbf{J_n}$ is an eigenvector of $\boldsymbol{\alpha}_{\mathbf{n}^*}\underline{\mathbf{G}}$ instead of $\underline{\mathbf{G}}$.[6,8,9] If the number of component is 1, equation (1.25b) will be reduced to equation (1.18).

There are also other simpler ways to derive the first nucleation theorem for multicomponent system. In the work by McGraw and Zhang, they showed that the first nucleation theorem took the following form,[10]

$$\left(\frac{\partial \ln J}{\partial \ln S_i}\right)_{sj,j\neq i,T} = n_i^* + \delta_i,\ 0 \le \delta_i \le 1 \qquad (1.26)$$

1.1.4 Nucleation from microscopic point of view

The Gibbs free energy of formation determined from equation (1.4) is based on macroscopic surface tension, which is not well defined as the cluster size approaches molecular scale. There are many studies focusing on obtaining the ΔG from microscopic properties without using the surface tension. One of the approaches is monomer density functional theory (DFT), which is an analogy for the commonly known DFT for electronic structure calculations. In the monomer DFT, the Gibbs free energy of formation (ΔG) is expressed as the functional of monomer spatial distribution density ($\rho(\mathbf{r})$).[11-18] However, the intermolecular potential used in the monomer DFT is typically L-J or other simplified spherical potentials, as a result the monomer DFT is only applicable to the homogeneous nucleation of a small range of systems, such as Argon, Krypton, *etc.* More recently, the aggregation-volume-bias Monte Carlo (AVBMC) has been used to calculate the Gibbs free energy of formation of more realistic systems, such as water, acetic acid, and alkanes.[19-22] In addition, the dynamical nucleation theory (DNT) has also been applied to calculate the nucleation rate.[23-27] The main idea of DNT is to calculate the

evaporation coefficient (γ_i) in equation (1.8) (see section 1.1.2) using the variational transition state theory (vTST). The hard sphere model can be used to calculate the collision coefficient (α_i) in (1.8). As a result, the equation (1.8) for all i can be solved at steady state. At the critical size i^*, evaporation coefficient (γ_i) and collision coefficient (α_i) are equal. The deficiency of DNT is that to calculate the steady state nucleation rate J, the evaporation rate of each cluster A_i needs to be obtained. As the cluster size increases, it requires too much calculation resources to obtain each γ_i, which makes the calculation impractical.

There are also some other attempts to obtain the Gibbs free energy of cluster formation using first principle calculations. This approach was widely applied to the nucleation system of atmospheric importance, such as the binary nucleation of sulfuric acid - water, ternary nucleation of sulfuric acid - water - ammonia/amines, and organic acids assisted nucleation.[28-48] In these studies, the interaction energy between the nucleation precursors, such as sulfuric acid, water, amines, and organic acids, were calculated using the electronic density functional theory (DFT) and resolution identity Møller-Plesset perturbation (RI-MP2) theory. It is an advantage that these approaches do not need empirical intermolecular potentials and macroscopic surface tension. However, as cluster size increases the calculation burden increases dramatically and all the aforementioned studies failed to show the existence of a barrier in the nucleation coordinate. More efforts are needed to link the results obtained in the DFT and RI-MP2 calculations to the Gibbs free energy of formation of clusters in the future.

Due to the semi-empirical nature of monomer DFT, complexity of DNT, and unsuccessfulness of first principle calculations, the classical and kinetic nucleation theories are still the most widely used approaches in the explanation of experimental observations.

1.2 Overview of nucleation experiments

1.2.1 Experimental techniques in the early days

Nucleation phenomena were ubiquitous in the nature. Many daily observations can be categorized as nucleation, such as crystallization, freezing, condensation, and bubble formation in boiling water. Initial measurements of nucleation rates are made by adiabatic expansion to create highly supersaturated vapor phases.[49-51] The high supersaturation then drives the formation of critical nucleus A_{n*} and the following compression cycle decreases the supersaturation, which decreases the nucleation rate to a negligible value. However, the remaining supersaturation is still large enough to permit the growth of nucleated critical nucleus to an optically detectable size. The number density of particles [52] formed in the expansion-compression process can be measured using Mie scattering. The during time of nucleation process (Δt) can be estimated from the expansion-compression cycles. As a result, the nucleation rate can be calculated as $N_p/\Delta t$.

Another type of adiabatic expansion is the shock tube technique which increases the quality of nucleation rate data significantly.[53] The shock tube consists of two sections, driver and driven sections, separated by a diaphragm, with the driver section filled with high pressure vapor and the driven section maintained at low pressure. As the diaphragm ruptures, the vapor inside the driver section undergoes adiabatic expansion, which generates the supersaturation in the driven section and initiates nucleation. The nucleation process is terminated by the reflection of shock water inside the shock tube. The adiabatic expansion technique is limited to high nucleation rate (10^3 to 10^{17} cm^{-3} s^{-1}) measurement. The total nucleation pressure of adiabatic expansion is typically between 100 kPa to 7MPa. These two limitations make the adiabatic expansion technique unsuitable for measuring low nucleation rate (10^{-2} cm^{-3} s^{-1}) and low nucleation pressure (below 100 kPa).

The static diffusion chamber (SDC) can be used to solve the problem encountered in the adiabatic expansion nucleation experiment. The SDC consists of two vertically arranged parallel plates, with the bottom and top plates kept at warmer and cooler temperatures, respectively.[54] The bottom plate is covered with liquid which evaporates and because of the concentration gradient, the vapor moves towards the top plate. Due to the temperature gradient, the vapor gets supersaturated as it rises from the bottom plate to the top plate. The supersaturated vapor nucleates to particles which grow to sizes that are optically detectable. Driven by the gravitational force, the particles eventually drop down to the bottom plate, making the process cycling. By adjusting the temperature of the bottom plate, a nucleation rate of 10^{-3} and 10^{4} cm^{-3} s^{-1} can be achieved. The SDC method is only suitable for single component nucleation systems and generates inaccurate results for multicomponent nucleation. It is due to that different component achieves same saturation ratio at different height in the SDC. In addition, continuous evaporation and condensation alters the liquid content which further changes the vapor phase composition, based on the Raoult's law.

Besides the adiabatic expansion and SDC, laminar flow chamber is also widely used in the early studies of nucleation.[55] In the laminar flow chamber, the carrier gas is saturated with the nucleating vapor in the hot section and then cooled down abruptly in the condenser section, which produce supersaturation and leads to nucleation. The freshly nucleated particles then grow to optically detectable sizes in the condenser section. The nucleation rate in the laminar flow chamber is typically 10^{2} to 10^{8} cm^{-3} s^{-1}. The laminar flow chamber is only suitable for nucleation system composed of large molecular weight species. For low molecular weight species, such as water, due to the closeness of molecular and thermal diffusivity, the nucleation zone is not well defined and there is significant loss of vapor on the wall, which makes the nucleation rate measurement more complicated.

The aforementioned techniques were widely applied to study the nucleation of alcohols, alkanes, water, and noble gases. In some of the previous studies, the experimentally measured nucleation rates and supersaturation were compared with the CNT predictions. For instance, in the work of Strey *et al.*, the nucleation rates of Xe, Ar, and He (Figure 9 therein) and n-butanol (Figure 11 therein) were measured and compared with CNT.[56] For the noble gases, the agreement was not very well, but the dependence of critical nucleus size on the supersaturation was consistent with the prediction of CNT. For n-butanol, the agreement of measurement with the CNT predictions was surprisingly well. All the aforementioned techniques used in the early studies of nucleation fails in the study of nucleation of trace gas species, because of the extremely low concentration of trace gases, such as sulfuric acid, organic acids, ammonia, and amines. In the next section, a new method that has been widely applied recently will be described.

1.2.2 Atmospheric nucleation measurements

Nucleation has not only theoretical importance in advancing our understanding of the dynamics of the non-equilibrium process but also practical importance in colloidal chemistry, especially in atmospheric sciences. Nucleation or new particle formation (gas-to-particle conversion) process is an important source of atmospheric aerosols besides the primary emissions. Atmospheric aerosols impact the Earth-Atmosphere system in several aspects. They influence the Earth radiation budget, impact cloud formation, cause or enhance diseases on humans, and change photochemical chemistry and partitioning of trace species by providing surfaces for heterogeneous chemical reactions.[57-62] The effects of aerosols are recognized as one of the key issues in the climate system and the hydrological cycle. Atmospheric aerosols cool the atmosphere by directly scattering a fraction of the incoming solar radiation back to space, which is often referred to as the aerosol direct effect. While acting as cloud condensation nuclei (CCN)

and ice nuclei (IN), aerosols play an important role in controlling cloud formation, development and precipitation on local, regional and global scales,[57,59] which is often referred to as the aerosol indirect effect. Presently, the aerosol direct and indirect effects represent the largest uncertainty in climate predictions.[57]

Atmospheric aerosols are typically divided into two categories, i.e., primary and secondary, on the basis of their formation in the atmosphere. Primary aerosols are emitted directly into the atmosphere from natural or anthropogenic sources, while secondary aerosols are formed via gas-to-particle conversion. Although a large portion of atmospheric aerosols is secondary and formed through nucleation and growth of nanoparticles, the mechanism of secondary aerosol formation remains highly uncertain, preventing the development of physically-based representation of those processes in atmospheric models.[63] New particle formation occurs in two distinct stages, i.e., nucleation to form critical nuclei and subsequent growth of freshly nucleated particles to larger sizes. Formation of the critical nucleus is restricted by entropy and a Gibbs free energy barrier exists prior to spontaneous transformation into the new phase. Also, there exists a large Kelvin effect for the growth of nanoparticles, because of elevated equilibrium vapor pressures above curved surfaces, which acts as another major limitation in the new particle formation process.

Several mechanisms have been proposed to explain nucleation events in the continental troposphere, including binary H_2SO_4/H_2O and ternary $H_2SO_4/H_2O/NH_3$ nucleation,[64,65] ion-mediated nucleation,[66,67] and nucleation enhanced by organic compounds.[45,46,68] Studies of atmospheric nucleation typically involve simultaneous measurements of the concentration, size distribution of aerosol particles and concentration of gaseous species.[44,45,51,65,68-83] In these experiments, flow chambers consisting of a turbulent mixing section followed by a laminar flow nucleation section have been developed. Typically, two or more gas flows carrying the

nucleating vapors are mixing together in the mixing zone which is heated up to more than 100 Celsius. As a result nucleation does not happen in mixing zone. Right after leaving the mixing zone, the gas flow in the laminar flow section is chilled to room temperature or below. Therefore, supersaturation of nucleating vapors is achieved and nucleation happens. The concentration of aerosol particles is measured using the condensation particle counter (CPC), which utilizes the light scattering technique. Recently, the particle size magnifier (PSM) is developed to detect sub 3 nm particles, which the traditional CPC has failed to detect. It has been suggested that the development of PSM is important, since the critical nuclei in the atmospheric nucleation is about 1.5 nm in size. The traditional CPC might have significantly underestimated the nucleation rate.[75,83-86] Finally, the nucleation rate can be calculated through dividing the total aerosol particle concentration by the nucleation time. The gaseous species concentration in the mixing zone can be measured by a mass spectrometer whose inlet is located inside the mixing zone.[44-46]

1.3 Growth of nucleation mode nanoparticles

1.3.1 Kinetics of nanoparticle growth

After nanoparticles are formed from nucleation, they usually encounter some other organics, such as glyoxal, amines, and methylglyoxal, which make the nanoparticles grow. The growth of nucleated small nanoparticles is an important first step for the formation of cloud condensation nuclei (CCN), since the freshly nucleated nanoparticles (below 20 nm) are too small to act as CCN (ca. 100 nm) directly. The flux of gaseous species towards the nanoparticle can be calculated via the following equation,

$$J = \frac{\rho_p}{M_A}\frac{d}{dt}\left(\frac{4}{3}\pi R_p^3\right) \tag{1.27}$$

where ρ_p is the density of the nanoparticle; M_A is the molecular weight of the gaseous species; R_p=1/2D_p is the radius of the nanoparticle. For freshly nucleated nanoparticles, the kinetic regime

applies to the growth equation, since the Knudsen number *Kn*, which is the ratio between mean free path (λ) and the nanoparticle diameter (D_p), is significantly larger than 1.[87] As a result,

$$J = J_k = \pi R_p^2 \omega \gamma (c_\infty - c_s) \tag{1.28}$$

where c_∞ is the molar concentration of gas species at infinity distance from the nanoparticle; c_s is the molar concentration of gas species near the surface of nanoparticles; ω is the thermal speed of gas species; γ is the uptake coefficient of gas species on nanoparticle surface.

Combining equation (1.27) and (1.28), the growth rate can be obtained as,

$$\frac{dR_p}{dt} = \frac{\gamma \omega M_A}{4\rho_p}(c_\infty - c_s) \tag{1.29}$$

As time increases, the concentration of gas species c_∞ and c_s decreases and increases, respectively. At time infinity these two quantities equal each other and the growth rate becomes 0.

1.3.2 Partitioning theory of particle growth

At time infinity, the equilibrium has been reached and the growth of nanoparticle stops. The partitioning of the chemical species between the gas phase and the nanoparticles phase can be derived from thermodynamic equilibrium laws.[88,89] At equilibrium, the chemical potentials of species *i* in the gas phase ($\mu_{i,g}$) and aerosol phase ($\mu_{i,OA}$) are equal.

$$\mu_{i,g} = \mu_{i,OA} \tag{1.30}$$

Assuming all the components in the aerosol phase are well mixed (no phase separation happens in the aerosol phase), the chemical potentials of species *i* in the gas phase and aerosol phase can be expressed in the equations (1.31a) and (1.31b), respectively.

$$\mu_{i,g} = \mu_{i,g}^0 + RT \ln(\frac{P_i}{P_{i,L}^0}) \tag{1.31a}$$

$$\mu_{i,OA} = \mu_{i,pure}^0 + RT \ln(\zeta_i X_{i,OA}) \tag{1.31b}$$

Where P_i is the vapor pressure of i; $P_{i,L}^{\ 0}$ is the saturation vapor pressure of i over its pure liquid state; ζ_i is the activity coefficient; $X_{i,OA}$ is the mole fraction of component i in the aerosol phase. In reality the previous assumption of no phase separation is questionable, since most atmospheric aerosols are composed of both organic and inorganic species, which are known to be immiscible with each other. In such cases, the above equations (1.31a-b) become invalid and more advanced techniques, such as AIOMFAC (Aerosol Inorganic-Organic Mixtures Functional Groups Activity Coefficients) model developed by Zuend *et al.* need to be used.[90-92] For the sake of simplicity, in the following discussions, only the situation of no-phase separation is considered.

For chemical equilibrium of component i pure liquid state and its gaseous state, equation (1.32) holds.

$$\mu_{i,g}^{0} = \mu_{i,pure}^{0} \tag{1.32}$$

Combining equations from (1.30),(1.31), and (1.32), the following equation can be obtained.

$$\frac{P_i}{P_{i,L}^{0}} = \zeta_i X_{i,OA} = \frac{n_{i,g}}{VP_{i,L}^{0}} RT = \zeta_i \frac{n_{i,OA}}{n_{OA}} \tag{1.33}$$

Where $n_{i,g}$ is the number of moles of i in the gas phase; $n_{i,OA}$ is the number of moles of i in the aerosol phase; n_{OA} is the number of moles of the total aerosols. Therefore,

$$\frac{n_{i,g}}{VP_{i,g}^{0}} RT = \frac{A_i}{P_{i,L}^{0} MW_i} RT \tag{1.34a}$$

$$\zeta_i \frac{n_{i,OA}}{n_{OA}} = \zeta_i \frac{F_{i,om}}{MW_i} \frac{1}{TSPf_{om} / MW_{om}} \tag{1.34b}$$

$$\frac{A_i}{P_{i,L}^{0} MW_i} RT = \zeta_i \frac{F_{i,om}}{MW_i} \frac{1}{TSPf_{om} / MW_{om}} \tag{1.34c}$$

Where Ai is the mass concentration of i in the gas phase; $F_{i,om}$ is the mass concentration of i in the aerosol phase; TSP is the total mass of particulate; MW_{om} is the average molecular weight of the aerosol phase; f_{om} is the soluble mole fraction in the aerosol phase.

Define the partitioning coefficient $K_{p,i}$ via the following equation (1.35)

$$K_{p,i} = \frac{F_{i,om}/TSP}{A_i} = \zeta_i \frac{f_{om}}{TSPf_{om}/MW_{om}} \tag{1.35}$$

Assuming the total concentration of component i in the gas and aerosol phase is T_i, the following equation holds,

$$T_i - F_{i,om} = A_i = \frac{F_{i,om}/TSP}{K_{p,i}} = \frac{K_{p,i}^{-1}F_{i,om}}{TSP(...,F_{i,om},...)} \tag{1.36a}$$

$$TSP(...,F_{i,om},...) = \sum_i F_{i,om} \tag{1.36b}$$

The above equation (1.36a) and (1.36b) can be solved iteratively for $F_{i,om}$ if the values of $K_{p,i}$ and T_i are known. Dividing both sides of equation (1.36a) by T_i, the following equations are obtained,

$$f_i = \frac{F_{i,om}}{T_i} = \frac{1}{1+\frac{K_{p,i}^{-1}}{TSP(...,f_i,...)}} = \frac{1}{1+\frac{C_i^*}{TSP(...,f_i,...)}} \tag{1.37a}$$

$$TSP(...,f_i,...) = \sum_i f_i T_i \tag{1.37b}$$

Where f_i is the fraction of component i in the gas phase to the total concentration; C_i^* defined as volatility and is the inverse of $K_{p,i}$. The equations (1.37a) and (1.37b) can also be solved iteratively if C_i^* and T_i are known. If compounds with similar C_i^* are grouped into one bin, a new T_i can be defined and f_i can be calculated. This grouping method does not change the formulas (1.37a) and (1.37b). After grouping of the compounds, T_i is the total concentration of i^{th} group. Since in the atmosphere, it is easier to determine the value of C_i^* than to determine the identities of the compounds, it is natural to group the compounds via volatility to reduce the complexity of

partitioning problem. The grouping method is called Volatility Basis Set (VBS), which is due to the work of Donahue and co-workers.[93-95]

1.3.3 The special partitioning of water: hygroscopicity

Due to the large quantity of water vapor in the atmosphere, the partitioning of water is usually treated separately from the partitioning of other trace organic species. At chemical equilibrium the water activity in the aerosol phase is related to the water vapor pressure via the following equation,

$$\begin{aligned} S_w &= \frac{P}{P_s} = a_w \exp\left(\frac{4\sigma M_w}{RT\rho_w D}\right) \\ &= \frac{(1/6\pi D^3 - 1/6\pi D_d^3)\rho_w / M_w}{\nu\rho_d / 6\pi D_d^3 / M_d + (1/6\pi D^3 - 1/6\pi D_d^3)\rho_w / M_w} \exp\left(\frac{4\sigma M_w}{RT\rho_w D}\right) \\ &= \frac{1}{1 + \frac{\nu\rho_d}{\rho_w}\frac{M_w}{M_d}\frac{1}{(D/D_d)^3 - 1}} \exp\left(\frac{4\sigma M_w}{RT\rho_w D}\right) \end{aligned} \tag{1.38}$$

Where S_w is the supersaturation of water vapor; P is the vapor pressure of water; P_s is the saturation vapor pressure of water; a_w is the water activity in the aerosol phase; D is the diameter of the aerosol particle; D_d is the diameter of dry aerosol particle; σ is the surface tension of aerosol particle.

Define a parameter κ as $1/a_w = 1 + \kappa\frac{V_d}{V_w}$.[96] Assume the average molecular weight of aerosol is M_d and the density of aerosol particle is ρ_d. Therefore,

$$\kappa = \frac{\nu\rho_d}{\rho_w}\frac{M_w}{M_d} \tag{1.39}$$

The above equation serves as the definition of κ. If the aerosol contains multicomponent and for each of the component molecular weights and densities are M_i and ρ_i, respectively, the total effective κ can be expressed as the linear combination of κ_i as equation (1.40) and (1.41) demonstrate,

$$\frac{1}{a_w} = 1 + \frac{\nu n_d}{n_w} = 1 + \frac{\nu \rho_d M_w}{M_d \rho_w} \frac{V_d}{V_w} = 1 + \kappa \frac{V_d}{V_w}$$
$$= 1 + \sum_i \frac{\nu_i n_i}{n_w} = 1 + \sum_i \varepsilon_i \frac{\nu_i \rho_i M_w}{M_i \rho_w} \frac{V_d}{V_w} = 1 + \sum_i \varepsilon_i \kappa_i \frac{V_d}{V_w} \quad (1.40)$$

$$\kappa = \sum_i \varepsilon_i \kappa_i \quad (1.41)$$

where ε_i is the volume fraction of component *i* in the aerosol particle. The equation (1.41) can be used to calculate the κ value if every single κ_i and their corresponding volume fraction ε_i are known. This is referred as the bottom up approach for calculation of κ.

The total κ value can also be calculated through top down approaches. There are two top down approaches based on CCN activity and hygroscopic factor measurements. First, CCN activity measurement approach is discussed below.

The critical supersaturation of CCN activation (Sc) is the maximum value of (Sw) along the coordinate of D. Define $A = \frac{4\sigma M_w}{RT\rho_w}$, as a result the equation (1.38) can be rewritten as,

$$S_w = \frac{1}{1 + \kappa \frac{1}{(D/D_d)^3 - 1}} \exp(A/D) \quad (1.42)$$

Take the first derivative of S_w with respect to D and set it to zero. The following equations can be obtained.

$$0 = (1 + \kappa \frac{1}{(D/D_d)^3 - 1})^{-2} \kappa [(D/D_d)^3 - 1]^{-2} 3(D/D_d)^2 (1/D_d) \exp(A/D)$$
$$- (1 + \kappa \frac{1}{(D/D_d)^3 - 1})^{-1} \exp(A/D) A/D^2 \quad (1.43a)$$

$$[1 + \kappa \frac{1}{(D/D_d)^3 - 1}]^{-1} \kappa [(D/D_d)^3 - 1]^{-2} 3(D/D_d)^3$$
$$= A/D \quad (1.43b)$$

Since $D >> D_d$, the (1.43b) can be solved approximately.

$$3\kappa[(D/D_d)^3]^{-1} = A/D \tag{1.43c}$$

$$D = (3\kappa D_d^3/A)^{1/2} \tag{1.43d}$$

As a result, the critical supersaturation S_c and κ can be calculated as,

$$\begin{aligned}
&\ln S_c = \ln a_w + A/D = \ln[1-(1-a_w)] + A/D = -(1-a_w) + A/D \\
&= \{1-\kappa[(D/D_d)^3-1]^{-1}\}^{-1}\kappa[(D/D_d)^3-1]^{-2}3[(D/D_d)^3] - \kappa[(D/D_d)^3-1]^{-1} \\
&= \kappa[(D/D_d)^3]^{-2}3[(D/D_d)^3] - \kappa[(D/D_d)^3]^{-1} = 2\kappa[(D/D_d)^3]^{-1} \\
&= 2\kappa[(\frac{3\kappa D_d}{A})^{3/2}]^{-1} = 2\kappa(\frac{A}{3\kappa D_d})^{3/2}
\end{aligned} \tag{1.43e}$$

$$\kappa = \frac{4A^3}{27{D_d}^3 \ln^2 S_c} \tag{1.43f}$$

Second, the hygroscopic factor measurement approach is discussed below. Define $D/D_d=Gf$, the equation (1.42) can be rewritten as,

$$S_w = RH = \frac{1}{1+\kappa\dfrac{1}{Gf^3-1}}\exp(A/D) \tag{1.44}$$

Therefore, κ can be calculated through the RH dependence of Gf.

$$\kappa = [\frac{1}{RH}\exp(A/D)-1](Gf^3-1) \tag{1.45a}$$

$$Gf = \{1+[\frac{1}{RH}\exp(A/D_d)-1]^{-1}\kappa\}^{1/3} \tag{1.45b}$$

The κ values calculated through the two top down approaches can be compared with the bottom up approach.

1.3.4 Growth attributable to chemical reactions

Besides liquid-liquid phase separation, the above partitioning theory also does not take into account the chemical reactions between the gas phase species and the aerosol particles. For instance, some organic species, such as amine and glyoxal, have high C^* values. According to equations (1.37a) and (1.37b), the fraction of amine and glyoxal in the aerosol phase (f_i) is

negligible. However, due to the chemical reactions, the effective C^* decreases for amines and glyoxal. Amines and glyoxal can partition significantly into the aerosol phase, since amines and glyoxal, instead of existing as original form, react with species in the aerosol phase to form low volatile organic salts and polymers. A few tandem differential mobility analyzer (TDMA) experiments have shown that amines and glyoxal can make the freshly nucleated sulfuric acid – water nanoparticles grow.[97,98] Unfortunately, the chemical identities of the gas phase species that can make the freshly nucleated nanoparticle grow are poorly known. It is one of the goals in the current project, besides nucleation experiment, to find out which chemical species contribute to the growth of freshly nucleated nanoparticle. The chemical mechanism for the growth also needs to be elucidated.

2. INTERACTION BETWEEN NUCLEATION PRECURSORS*

2.1 Introduction

Atmospheric aerosols impact the Earth-Atmosphere system in several aspects. They influence the Earth radiation budget, impact cloud formation, cause or enhance diseases on humans, and change photochemical chemistry and partitioning of trace species by providing surfaces for heterogeneous chemical reactions.[57-62] The effects of aerosols are recognized as one of the key issues in the climate system and the hydrological cycle. Atmospheric aerosols cool the atmosphere by directly scattering a fraction of the incoming solar radiation back to space, which is often referred to as the aerosol direct effect. While acting as cloud condensation nuclei (CCN) and ice nuclei (IN), aerosols play an important role in controlling cloud formation, development and precipitation on local, regional and global scales,[57,59] which is often referred to as the aerosol indirect effect. Presently, the aerosol direct and indirect effects represent the largest uncertainty in climate predictions.[57]

Aerosols can be directly emitted into the atmosphere from natural and anthropogenic sources or formed in the atmosphere through nucleation from gas-phase species. New particle formation produces a large fraction of atmospheric aerosols and has been frequently observed in various environments, including urban, forested, and remote continental areas. New particle formation occurs in two distinct stages,[81,82,97,99] i.e., nucleation to form the critical nucleus (with the maximum free energy) and subsequent growth of the critical nucleus to a detectable size (2-3

* Reprinted with permission from Xu, W., & Zhang, R. (2012). Theoretical Investigation of Interaction of Dicarboxylic Acids with Common Aerosol Nucleation Precursors. *The Journal of Physical Chemistry A, 116*(18), 4539-4550. Copyright (2012), American Chemical Society

nm) that competes with capture and removal of the critical cluster by coagulation with pre-existing aerosols. New particle formation is kinetically limited by the population of critical nucleuses; the rate at which nucleation occurs is related to the chemical makeup of the critical nucleus and the gaseous concentrations of the nucleating species and represents an important variable in simulations of aerosol formation in atmospheric models.[81] Currently, a large uncertainty exists in the chemical compositions of the critical nucleus and the identity of chemical species that participate in the nucleation and growth of nanoparticles in the atmosphere.

Several mechanisms have been proposed to explain nucleation events in the continental troposphere, including binary H_2SO_4/H_2O and ternary $H_2SO_4/H_2O/NH_3$ nucleation,[64,65] ion-mediated nucleation,[66,67] and nucleation enhanced by organic compounds.[45,46,68] Sulfuric acid has been widely identified as one of the major atmospheric nucleating species.[81,100] The importance of organic species in aerosol nucleation has been recently realized.[35,45-47,68] Organic compounds from anthropogenic and biogenic emissions react with atmospheric oxidants to form a number of products,[101-103] including organic carbonyls and acids, some of which may participate in nucleation and growth to form nanoparticles under various environments.[97,104,105] Organic aerosol nucleation was first suggested to occur through the formation of stable heterodimers of monocarboxylic acids.[106] However, theoretical calculations have indicated that those dimers have no vacant hydrogen acceptor/donor groups to promote subsequent cluster growth and are unlikely to contribute to new particle formation by themselves only.[46,47,81] On the other hand, the presence of organic acids considerably enhances new particle formation of the water-sulfuric acid system via formation of strongly hydrogen-bonded clusters containing one molecule of an organic acid and several molecules of sulfuric acid and water,[10,46,47,81] likely explaining field measurements of high aerosol concentrations observed in polluted and forested environments.

Numerous experimental and theoretical studies have been conducted to investigate the mechanisms of atmospheric aerosol nucleation. For example, previous theoretical studies using quantum chemical calculations have explored the interaction of sulfuric acid with ammonia,[29,107] amines,[32,34,40] and organic acids.[35,37,39,45-47,108,109] Strong hydrogen bonding between organic acids and atmospheric nucleation precursors has been demonstrated in the previous studies.[35,45,47] For example, Zhao *et al*. employed the quantum theory of atoms in molecules to elucidate the nature of hydrogen bonds formed in the organic acid clusters,[47] and the results indicated that the organic acids-sulfuric acid/ammonia clusters possess one strong-strength hydrogen bond and one medium-strength hydrogen bond, stabilizing the critical nucleus by lowering the free energy. In addition to monocarboxylic acids, theoretical studies on the interaction between dicarboxylic acids and common aerosol nucleation precursors have also been carried out for both neutral[37,39,108] and charged[37,39,109] clusters. Xu *et al.* showed that maleic acid stabilizes both neutral and ionic sulfuric acid/ammonia clusters[37], while oxalic acid stabilizes only ionic clusters.[39] Ehn *et al.* showed that oxalic, malonic, and succinic acids stabilize anionic clusters of bisulfate.[109] Another previous study revealed that dicarboxylic acids have lower saturation vapor pressures than those of monocarboxylic acids,[110] suggesting that dicarboxylic acids may play a more important role in partitioning into the particle-phase.

In the present study, the interaction of five dicarboxylic acids, including oxalic acid (OA, $C_2H_2O_4$), malonic acid (MOA, $C_3H_4O_4$), maleic acid (MEA, $C_4H_4O_4$), phthalic acid (PA, $C_8H_6O_4$), and succinic acid (SUA, $C_4H_6O_4$), with common atmospheric aerosol nucleation precursors (i.e., sulfuric acid and ammonia) is studied using the density functional theory (DFT), quantum theory of atoms in molecules (QTAIM), and natural bond orbital (NBO) analysis methods. The five dicarboxylic acids are chosen because they correspond to the most abundant dicarboxylic acids in the atmosphere.[111] The results of quantum chemical calculations using

several different levels of theory, including coupled-cluster theory with single and double excitations with perturbative corrections for the triple excitations (CCSD(T)) and two density functionals, B3LYP and PW91PW91, are compared and discussed. The implications of the present results for atmospheric aerosol nucleation are discussed.

2.2 Theoretical methods

All the calculations were performed on a 3 64-core Altix 450 machines with 128GB memory each using Gaussian 03 software package.[112] B3LYP functional with Pople's basis set 6-311++G (2d, 2p) was employed for geometry optimization. For each stationary point, frequency calculations were performed to ensure there were no imaginary frequencies. The optimized geometry was taken in single point energy calculations using CCSD(T)) and PW91PW91 with the 6-311++G (2d, 2p) and 6-311++G(3df,3pd) basis sets, respectively. Basis set superposition error (BSSE) at B3LYP level of theory for each stationary point, and at PW91PW91 and CCSD(T) for some of the stationary points were obtained using the counterpoise method implemented in Gaussian 03 package. The free energy of the cluster formation was calculated using the single point electronic energies from B3LYP, CCSD(T), and PW91PW91 and the thermal correction from B3LYP and BSSE corrections. The energetics of the sulfuric acid-water and oxalic acid-water clusters obtained at the B3LYP/6-311++G (2d, 2p)) level was compared with the results from CCSD(T) and PW91PW91/6-311++G(3df,3pd). Subsequently, the geometry and energetics at the B3LYP/6-311++G (2d, 2p) level was used to investigate the heterodimer and heterotrimer clusters of all dicarboxylic acids with sulfuric acid, ammonia, and water. In addition, single point calculations using PW91PW91/6-311++G(3df,3pd) were also made for comparison. To further evaluate the theoretical method**,** the results from B3LYP were compared with those reported previously using PW91PW91 for SA, OA, and MEA[31,32].

The topological analysis of OA, MOA, MEA, PA, SUA, and clusters of PA with sulfuric acid, ammonia, and water was carried out using QTAIM[113] with AIM2000 software[114-116] at the B3LYP/6-311++G(2d,2p) level. The topological properties (e.g., charge density and its Laplacian, energy densities) at the hydrogen bond critical points were used to evaluate the individual hydrogen bond strength in those molecules and molecular clusters. NBO analysis[117] calculations were also carried out using Gaussian 03 to investigate the individual hydrogen bond strength.

2.3 Results and discussion

2.3.1 Geometrical analysis

The geometries of H_2SO_4, H_2O, NH_3, and the five dicarboxylic acids are optimized at the B3LYP level with 6-311++G (2d, 2p) basis set using the Gaussian 03 package. The calculated geometries of H_2SO_4, H_2O and NH_3 are consistent with the available experimental values (Tables 2.1 and 2.2). Sulfuric acid possesses a C_2 symmetry, consistent with that described by Zhao et al.[47] There are several possible conformations of dicarboxylic acids and their molecular complexes, but only the conformations with the intramolecular O-H···O hydrogen bonds are presented. Figure 2.1 shows that, except for oxalic acid, the stable conformations of dicarboxylic acids have an intramolecular hydrogen bond and a free carboxylic group. An additional hydrogen bond is formed between the two adjacent carboxylic groups in oxalic acid. The strength of the intramolecular hydrogen bond is restrained by the molecular structure of the dicarboxylic acids. With a stronger hydrogen bond (i.e., a shorter O-H···O distance), lengthening of the O-H bond in the carboxylic group is larger. For example, the sequence of the intramolecular hydrogen bond distances of the five dicarboxylic acids in a decreasing order is OA (2.128 Å) > SUA (1.835 Å) > MOA (1.778 Å) > MEA (1.651 Å) > PA (1.598 Å), and the hydrogen bond strength increases correspondingly from OA to PA. In contrast, the sequence of

the O-H bond lengths in the carboxylic group in an increasing order is OA (0.974 Å) < SUA (0.976 Å) < MOA (0.980 Å) < MEA (0.986 Å) and PA (0.986 Å). The O-H bond length in the free carboxylic acid group ranges from 0.968 to 0.970 Å, which is shorter than the corresponding O-H bond length in the hydrogen bonded ones (0.974-0.986 Å).

Table 2.1.[a] Comparison of calculated geometries with experimentally determined geometries for sulfuric acid.

	This work	Zhao et al.[47]	Exp[118]
	B3LYP/6-311++G (2d, 2p)	B3LYP/6-31G (d, p)	
d(S=O)	1.429	1.447	1.422
d(S-O)	1.608	1.626	1.574
d(O-H)	0.968	0.973	0.970
α(O=S=O)	124.6	124.6	123.3
α(O-S-O)	101.8	101.6	101.3
α(S-O-H)	108.4	107.7	108.5

a. Length is in angstrom and angle is in degree.

Table 2.2.[a] Comparison of calculated geometries with experimentally determined geometries for ammonia and water.

		This work	Zhao et al[47]	Exp[119]
		B3LYP/6-311++G (2d,2p)	B3LYP/6-31G(d,p)	
H_2O	d(O-H)	0.961	0.965	0.957
(C_{2v})	α(H-O-H)	105.1	103.8	104.5
NH_3	d(N-H)	1.013	1.018	1.012
(C_{3v})	α(H-N-H)	107.2	105.8	106.7

a. Length is in angstrom and angle is in degree.

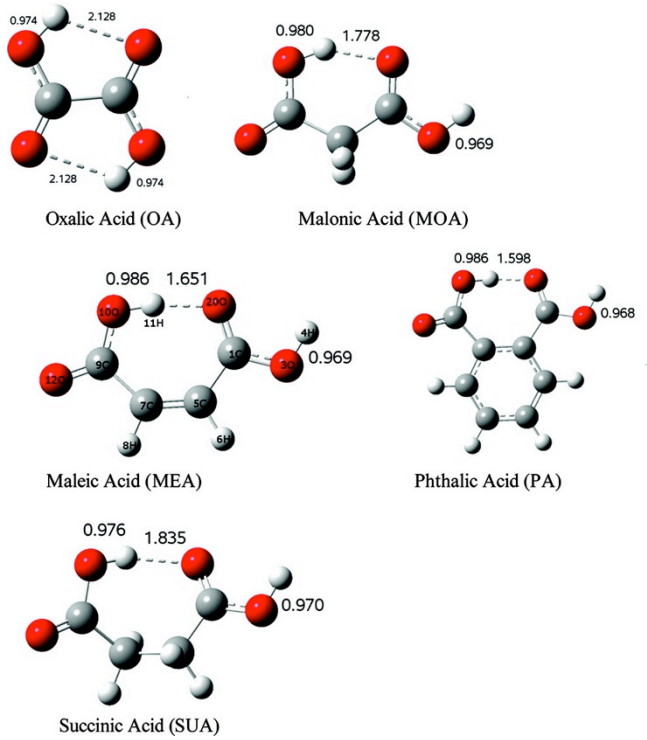

Figure 2.1. Optimized geometries of the five dicarboxylic acids at B3LYP/6-311++G(2d,2p) (red for oxygen, white for hydrogen, gray for carbon, yellow for sulfur, and blue for nitrogen).

The geometries obtained using B3LYP/6-311++G(2d,2p) for OA and MEA is summarized in Table 2.3, along with those previously reported using PW91PW91/6-311++G(3df,3pd) and the experimental values. Table 2.3 shows that both B3LYP and PW91PW91 geometries agree well with the experimental values. Table 2.4 compares the B3LYP and PW91PW91 vibrational frequencies of MEA with the experimental values. Similarly, both B3LYP and PW91PW91 yield the vibrational frequencies in agreement with the experimental values.

Table 2.3. Geometry parameters and O-H stretching frequency for OA and MEA calculated using B3LYP/6-311++G(2d,2p). Also included in the table for comparison are the experimental data[120] and results previously calculated using PW91PW91/6-311++G(3df,3pd)[37,39]. The bond lengths, angles, and frequencies are given in angstroms, degrees, and cm^{-1}, respectively.

OA				MEA			
parameter	B3LYP/6-311++G(2d,2p)	PW91PW91/6-311++G(3df,3pd)[39]	Exp[121]	parameter	B3LYP/6-311++G(2d,2p)	PW91PW91/6-311++G(3df,3pd)[37]	Exp[120]
B_{C-C}	1.544	1.544	1.548	C1-O2	1.22	1.23	1.20
$B_{C=O}$	1.202	1.211	1.208	C1-O3	1.34	1.35	1.27
B_{C-O}	1.325	1.330	1.339	C1-C5	1.47	1.47	1.44
B_{O-H}	0.974	0.986	1.056	C5-C7	1.34	1.35	1.43
$A_{C-C=O}$	121.35	121.51	123.1	C7-C9	1.51	1.51	1.46
$A_{O=C-O}$	125.21	125.51	125.0	C9-C12	1.21	1.22	1.21
A_{C-O-H}	107.50	105.83	104.4	C9-C10	1.33	1.33	1.27
ν_{O-H}	3661	3487	3475	O2-O10	2.63	2.61	2.46
				∠O2-C1-O3	121.4	121.3	125.5
				∠O3-C1-C5	111.2	111.3	114.8
				∠O2-C1-O5	127.3	127.4	118.4
				∠C1-C5-C7	128.2	127.9	126.7
				∠C5-C7-C9	133.7	133.6	124.7
				∠C5-C7-C10	120.4	120.1	124.1
				∠O10-C9-O12	121.9	122.1	119.2
				∠C7-C9-O12	117.7	117.8	111.3

Table 2.4. Comparison of vibrational frequencies of MEA (in cm^{-1}) between calculated using B3LYP/6-311++G(2d,2p), previously calculated using PW91PW91/6-311++G(3df,3pd)[37,39] and the experimental values[122].

Freq	B3LYP/6-311++G(2d,2p)	PW91PW91/6-311++G(3df,3pd)[37]	Exp[122]
1	3756	3637	
2	3344	3132	
3	3199	3116	
4	3183	3091	
5	1785	1729	1705
6	1736	1678	1635
7	1676	1626	1587
8	-	-	1565
9	1461	-	1459
10	1449	1424	1432
11	1230	1297	1261
12	1178	1188	1218

A previous study showed that succinic acid has two stable conformations, with and without intramolecular hydrogen bond.[123] The two conformations have a small energy difference of about 2.5 kcal mol^{-1}, and convert readily to each other if the thermal kinetic energy is sufficient to facilitate crossing of this isomerization barrier. To obtain the potential energy surface (PES) along the reaction coordinate corresponding to breaking of the intramolecular hydrogen bond, a relaxed PES profile is obtained. The relative energies of the two conformations are plotted as a function of the intramolecular hydrogen bond length in Figure 2.2. The barrier height for isomerization between the two conformations is about 3 kcal mol^{-1} from configuration I to II. At room temperature (298.15 K), the translational energy is 1.5 kT, which equals to 3.7 kcal mol^{-1}. As a result, thermal collision with buffer gas molecules at room temperature is sufficient to break the intramolecular hydrogen bond in succinic acid and conversion between the conformations occurs readily in the atmosphere.

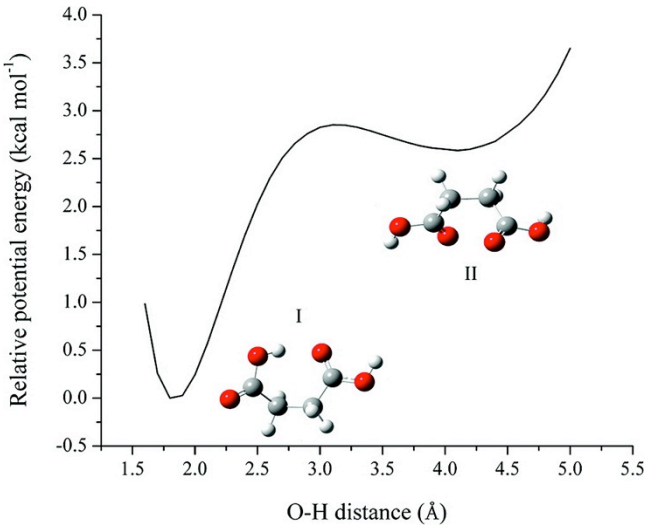

Figure 2.2. Potential energy surface along the intramolecular hydrogen bond obtained by the relaxed potential energy surface scan at B3LYP/6-311++G(2d,2p).

On the basis of the monomers with one intramolecular hydrogen bond, the heterodimer molecular complexes of the dicarboxylic acids are constructed and optimized. Figure 2.3 illustrates the structures of the heterodimer complexes of PA with sulfuric acid/ammonia/water. There exists a pair of inter-molecular hydrogen bonds between one of the carboxylic groups and sulfuric acid/ammonia/water and an intra-molecular hydrogen bond for the additional carboxylic group. The PA molecule acts as both a hydrogen bond donor and acceptor in the inter-molecular pair, with a stronger and a weaker hydrogen bond. Since the stronger hydrogen bond for the PA-ammonia (AM) complex involves the interaction of an nitrogen and hydrogen atom, the strength of this hydrogen bond cannot be directly compared to that of the PA-sulfuric acid (SA) complex using the bond lengths (i.e., 1.687 and 1.656 Å̊, respectively). Instead, the strength of the inter-molecular hydrogen bond can be inferred from the lengthening of the adjacent O-H bond. The strength of the stronger inter-molecular hydrogen bond decreases in the order from PA-AM (1.016 Å̊), PA-SA (1.000 Å̊), to PA-water (W) (0.991 Å̊). Therefore, without considering the

contribution from the weak hydrogen bond, the interaction between dicarboxylic acids and sulfuric acid/ammonia/water decreases from PA-AM, PA-SA, to PA-W. However, for the weaker hydrogen bond, the strength of the PA-SA complex is the strongest (1.715 Å), and the strength of the PA-AM complex is the weakest (2.688 Å). The strength of the weaker hydrogen bond decreases, from 1.715 Å for PA-SA to 2.169 Å for PW-W, consistent with lengthening of the adjacent O-H bond (i.e., from 0.989 Å to 0.968 Å, respectively). As to be discussed in the NBO and thermochemical analysis section, the overall interaction energy can be computed from the combined strengths of the inter-molecular hydrogen bond pair.

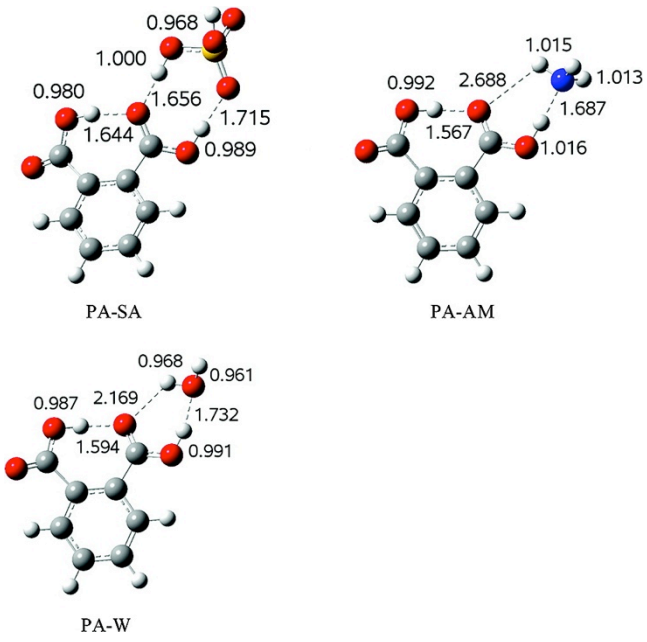

Figure 2.3. Optimized geometries of selected heterodimer complexes of phthalic acid with sulfuric acid, ammonia, and water at B3LYP/6-311++G(2d,2p).

It is also interesting to compare the changes in the intramolecular hydrogen H···O bond, when a molecule of sulfuric acid/ammonia/water is added to the dicarboxylic acids. The strength of intramolecular hydrogen bond in PA-SA is weaker than that in PA. The adjacent O-H distance in PA-SA (0.980 Å) is shorter than that in PA (0.986 Å), while the intramolecular hydrogen bond distance in PA-SA (1.644 Å) is larger than that in PA (1.598 Å), both indicating a stronger bond for PA. This behavior is explained by the strong hydrogen donor characteristic of sulfuric acid. Because the oxygen atom (O=C in the carboxylic group) forms two hydrogen bonds, the stronger inter-molecular hydrogen bond between PA and SA weakens the intra-molecular hydrogen bond. In contrast, the intra-molecular hydrogen bond in PA-AM is stronger than that in PA. The adjacent O-H distance in PA-AM (0.992 Å) is longer than that in PA (0.986 Å), while intra-molecular hydrogen bond length in PA-AM (1.567 Å) is shorter than that in PA (1.598 Å). This is probably attributable to a weaker inter-molecular hydrogen bond between PA and AM on the oxygen atom (O=C), leading to strengthening of the corresponding intramolecular hydrogen bond. The intramolecular hydrogen bond in PA-W is largely unaffected compared to that in PA, and the distances of the adjacent O-H and H···O intramolecular bonds are comparable between PA-W and PA. The geometrical features of the other heterodimer complexes of dicarboxylic acids with sulfuric acid/ammonia/water are similar and are comparable with those for monocarboxylic acids previously described by Zhao et al.[47]

In addition to the heterodimer molecular complexes, heterotrimer complexes of dicarboxylic acids with sulfuric acid/ammonia/water molecules are also investigated. Figure 2.4 depicts the optimized geometries of heterotrimer molecular complexes for selected dicarboxylic acids (SUA, OA, and PA). Those conformations are local minima on the multidimensional PES of the corresponding molecular clusters. More stable conformations may exist and be obtained by configurational sampling methods, which are out of the scope of this study. The heterotrimer

complexes have two major configurations, one with dicarboxylic acids at the ends and another with dicarboxylic acids in the middle. For each configuration, the dicarboxylic acid has two major conformations. For example, in the SA-SUA-SA complex SUA has two conformations (I and II in Figure 2.4), with or without the intramolecular hydrogen bond. Both conformations I and II exhibit four hydrogen bonds. Conformation II is more stable than conformation I, since the weaker intramolecular hydrogen bond is replaced by a stronger SUA-SA intermolecular hydrogen bond. This finding is also corroborated by thermochemical analysis to be discussed in the next section.

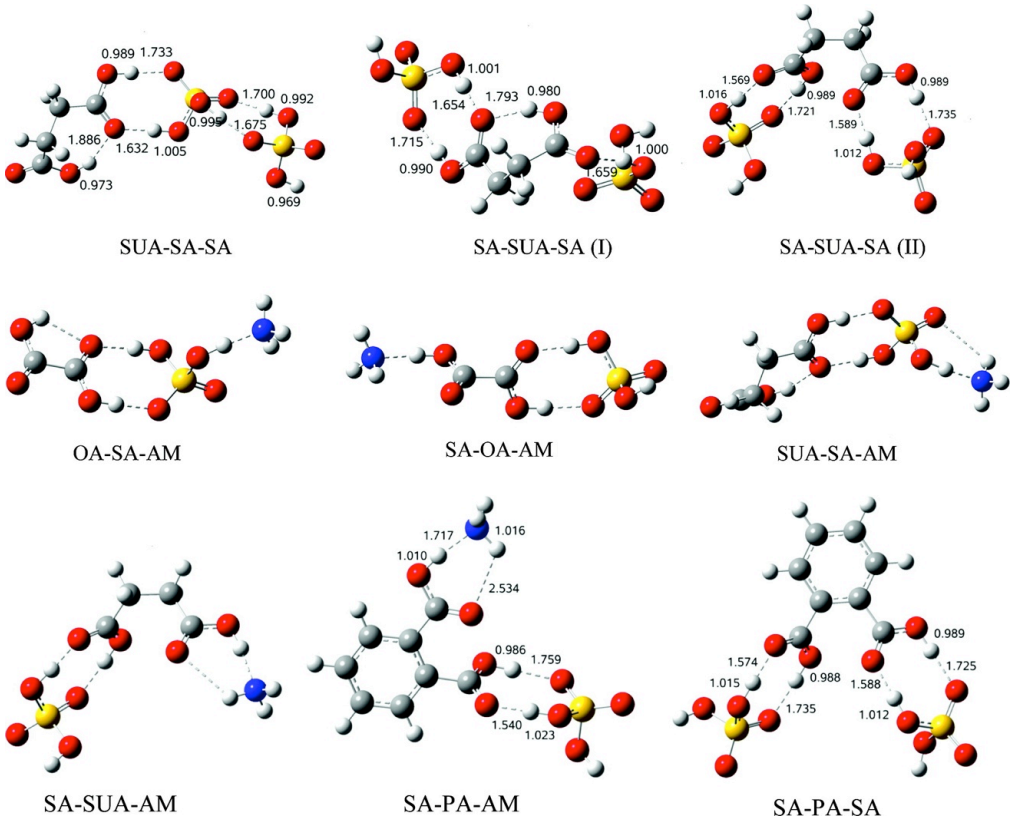

Figure 2.4. Optimized geometries of selected heterotrimer molecular complexes of dicarboxylic acids (i.e., phthalic, oxalic, and succinic acids) with sulfuric acid, ammonia, and water at B3LYP/6-311++G(2d,2p).

The geometries of two heterotrimer complexes, SA-PA-SA and SA-PA-AM, can be compared with their corresponding heterodimer complexes. The four hydrogen bond lengths in SA-PA-SA complex are close to their counterparts in the SA-PA complex, except for the length of SO-H···O hydrogen bond. The lengths of two SO-H···O hydrogen bonds in SA-PA-SA are 1.574 and 1.588 Å, which are smaller than the length of SO-H···O hydrogen bond (1.656 Å) in the SA-PA complex. Hence, the SO-H···O hydrogen bonds in SA-PA-SA are slightly stronger than the corresponding SO-H···O hydrogen bond in PA-SA. This is explainable because of weakening of the SO-H···O hydrogen bond by the adjacent intramolecular hydrogen bond in the PA-SA complex. The CO-H···O hydrogen bond lengths in SA-PA-SA are 1.735 and 1.725 Å, which are close to the length of CO-H···O hydrogen bond (1.715 Å) in PA-SA. This indicates the CO-H···O hydrogen bond strength is not affected by the intramolecular hydrogen bond in PA-SA. The strengths of the SO-H···O and CO-H···O hydrogen bonds on each side of SA-PA-SA are comparable, i.e., with the similar values of the hydrogen bond lengths on each side. For complex SA-PA-AM, the length of CO-H···N (1.717 Å) in SA-PA-AM is close to that of CO-H···N (1.687 Å) in PA-AM, while the length of NH···O (2.534 Å) in SA-PA-AM is smaller than that of NH···O (2.688 Å) in PA-AM. This suggests a small change of the NH···O hydrogen bond strength in PA-AM after addition of sulfuric acid on the other side, but the strength of CO-H···N does not change noticeably after the sulfuric acid addition. The different characteristics in the CO-H···N and NH···O hydrogen bonds within the heterotrimer complex SA-PA-AM are attributable to the presence of the intramolecular hydrogen bond within the heterodimer complex PA-AM, similarly to those in the complex SA-PA-SA.

Formation of molecular complexes of dicarboxylic acids also results in changes of the vibrational frequencies of the functional groups. The values of the frequency shifts for the phthalic acid complexes are summarized in Table 2.5. Red shifts in stretching frequencies are

evident for all the bonds that participate in the hydrogen bond formation. The amount of the red shift also reflects the strength of the hydrogen bonding. The SO-H···O=C (68.94 cm^{-1}) hydrogen bond is much stronger than the NH···O=C (29.78 cm^{-1}) and OH···O=C (26.38 cm^{-1}) hydrogen bonds, because the frequency shift of C=O stretching for the former hydrogen bond is much larger than that for the latters. Similarly, the COH···N (931.50 cm^{-1}) hydrogen bond is much stronger than the COH···O=S (414.18 cm^{-1}) and COH···O (451.89 cm^{-1}) hydrogen bonds. The interaction strength of phthalic acid with sulfuric acid/ammonia/water is determined by the combination of the two aforementioned hydrogen-bonding strengths. Red shifts in the stretching frequencies for O=C, O=S, CO-H, and SO-H functional groups also exist in the heterotrimer complexes. The values of the red shifts for the SA-PA-SA and SA-PA-AM heterotrimer complexes are also presented in Table 2.5. The frequency shifts of the two C=O functional groups in SA-PA-SA are 78.57 and 84.46 cm^{-1}, similar to the corresponding frequency shift (68.94 cm^{-1}) in SA-PA. The frequency shifts of the two C=O functional groups in SA-PA-AM are 83.05 and 42.05 cm^{-1}, corresponding to those of 68.94 and 29.78 cm^{-1} in PA-SA and PA-AM, respectively. On the basis of the values of red shifts, it can be concluded that the interaction strength of dicarboxylic acids with sulfuric acid or ammonia in the heterotrimer complexes are comparable to that in the heterodimer complexes.

Table 2.5. Frequency[a] (cm^{-1}) shifts of the functional groups for heterodimer and heterotrimer complexes of phthalic acid with sulfuric acid, ammonia, and water.

Complexes	S=O	SO-H	C=O	CO-H
PA-SA	-101.13	-651.15	-68.94	-414.18
PA-AM			-29.78	-931.50
PA-W			-26.38	-451.89
SA-PA-SA	-87.91	-847.39	-78.57	-386.24
	-92.19	-908.53	-84.46	-409.77
SA-PA-AM			-83.05	-353.93
	-84.61	-1036.66	-42.05	-819.32

[a] All frequencies are obtained from B3LYP/6-311++G (2d, 2p) and are un-scaled.

2.3.2 Topological and NBO analysis

In addition to the geometrical analysis, topological analysis using QTAIM provides an alternative way to evaluate the hydrogen bond strength. According to Bader's theory, the nuclei are (3,-3) the critical points where the charge density is maximum in all directions. The bond critical points (BCP) (3,-1) correspond to the charge density Hessian matrix that has one positive and two negative eigenvalues. The bond critical points and the nuclei are connected by the maximum charge density paths. Two adjacent paths form a bond path by connecting the adjacent nuclei. The ring critical points (RCP) (3,+1) occur where the charge density Hessian has one negative and two positive eigenvalues. Nuclei, BCP, RCP and bond paths constitute the molecular graphs, as presented in Figure 2.5. The ring structure of the inter and intra molecular

hydrogen bonds are similar to that described by Zhao *et al.*[47] The topological parameters, such as charge density (ρ) and its Laplacian ($\nabla^2\rho$), gradient kinetic energy density (G), potential energy density (V), and electronic energy density (K), are summarized in Table 2.6. The values of ρ, $\nabla^2\rho$, G, V, and K are comparable to those reported by Zhao *et al.*[47] A positive value of ρ indicates a closed-shell interaction between two hydrogen bonded atoms, according to Koch and Popelier.[124] The strength of the hydrogen bond is related to the magnitude of K at BCP of the corresponding hydrogen bond. The hydrogen bond strength increases with decreasing K. As a result, the intra-molecular hydrogen bond strength increases from OA, SUA (-0.02 au.), MOA (-0.19 au.), MEA (-0.59 au.), to PA (-0.88 au.). Addition of sulfuric acid to PA (-0.57 au.) decreases the intramolecular hydrogen bond strength, but addition of ammonia to PA (-1.17 au.) increases the strength. However, addition of water to PA (-0.92 au.) does not alter the strength appreciably. The strength of the stronger hydrogen bond in the complexes of PA with sulfuric acid, ammonia, and water decreases from PA-AM (-1.26 au.), PA-SA (-0.50 au.) to PA-W (-0.28 au.), while the strength of the weaker hydrogen bond in those clusters decreases from PA-SA (-0.21 au.), PA-W (0.17 au.), to PA-AM. Those results are consistent with geometrical bond length analysis.

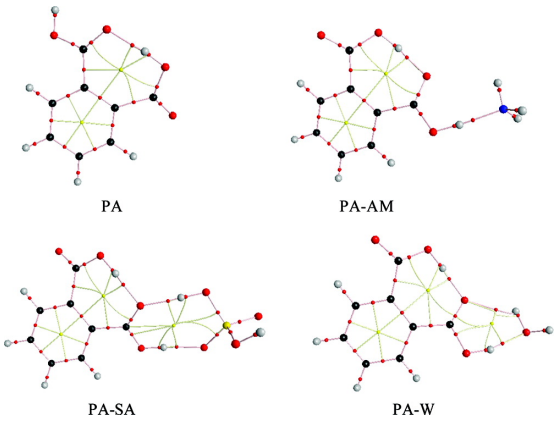

Figure 2.5. Molecular graphs of PA, PA-AM, PA-SA, and PA-W complexes showing the BCPs, ring critical points, bond path, and ring path.

Table 2.6. Topological parameters (Charge Densities, Laplacian, Gradient Kinetic Energy Densities, Potential Energy Densities, and Electronic Energy Densities) at BCPs of the hydrogen bonds of the complexes (in au.)[a]

	$\rho(10^{-2})$	∇^2 (10^{-2})	G(r) (10^{-2})	V(r) (10^{-2})	K(r) (10^{-2})	$\rho(10^{-2})$	$\nabla^2(10^{-2})$	G(r) (10^{-2})	V(r) (10^{-2})	K(r) (10^{-2})
			Inter HB							
MOA	3.99	12.20	3.24	-3.43	-0.19					
MEA	5.06	13.61	4.00	-4.59	-0.59					
PA	5.76	15.03	4.64	-5.53	-0.88					
SUA	3.26	10.27	2.59	-2.61	-0.02					
PA-SA	5.13	14.47	4.19	-4.77	-0.57					
PA-AM	6.28	15.27	4.98	-6.15	-1.17					
PA-W	5.84	15.06	4.69	-5.61	-0.92					
			Stronger HB					Weaker HB		
PA-SA	4.77	12.47	3.62	-4.12	-0.50	3.95	11.60	3.11	-3.33	-0.21
PA-AM	5.58	8.23	3.32	-4.58	-1.26					
PA-W	4.11	11.48	3.15	-3.44	-0.28	1.70	6.15	1.37	-1.20	0.17

[a] Geometries of all complexes are optimized at B3LYP/6-311++G(2d,2p) level. The bond paths for the two intramolecular hydrogen bonds in OA and the weaker intermolecular hydrogen bond in PA-AM are not observed.

In the NBO analysis, the hydrogen bond strength is related to the interaction energy between nonbonded natural orbital of the hydrogen acceptor and the unoccupied antibonding orbital of the hydrogen donor DH bond (σ^*_{DH}).[125] The interaction energies for those hydrogen bonds are summarized in Table 2.7. The intramolecular hydrogen bond strength increases from OA (2.42 kcal mol^{-1}), SUA (11.79 kcal mol^{-1}), MOA (16.05 kcal mol^{-1}), PA-SA (22.63 kcal mol^{-1}), MEA (27.03 kcal mol^{-1}), PA (31.31 kcal mol^{-1}), PA-W (31.43 kcal mol^{-1}), to PA-AM (36.15 kcal mol^{-1}). On one hand, the strength of the stronger intermolecular hydrogen bond in the complexes of PA with sulfuric acid, ammonia, and water decreases from PA-AM (38.06 kcal mol^{-1}), PA-SA (26.84 kcal mol^{-1}), to PA-W (21.18 kcal mol^{-1}). On the other hand, the strength of the weaker intermolecular hydrogen bond decreases from PA-SA (22.50 kcal mol^{-1}), PA-W (2.05 kcal mol^{-1}), to PA-AM (0.10 kcal mol^{-1}). The combination of the two intermolecular hydrogen bonds strength shows that the interaction decreases from PA-SA (49.34 kcal mol^{-1}), PA-AM (38.16 kcal mol^{-1}), to PA-W (23.23 kcal mol^{-1}). This result further corroborates the findings in geometrical analysis and is consistent with the thermochemical analysis results, to be discussed in the next section.

Table 2.7. NBO interaction energies[a] for the hydrogen bond of different complexes (in kcal mol^{-1})

	Inter HB	Stronger HB	Weaker HB
OA	2.42		
MOA	16.05		
MEA	27.03		
PA	31.31		
SUA	11.79		
PA-SA	22.63	26.84	22.25
PA-AM	36.15	38.06	0.10
PA-W	31.43	21.18	2.05

[a] All calculations are carried out at B3LYP/6-311++G(2d,2p) level.

2.3.3 Thermochemical analysis

Table 2.8 summarizes the Gibbs free energy changes associated with hydration of sulfuric acid and oxalic acid and the complex formation involving sulfuric acid, ammonia, oxalic acid, and maleic acid. The B3LYP/6-311++G(2d,2p) results are also compared with those predicted by CCSD(T)/6-311++G(2d,2p) and previously reported using PW91PW91/6-311++G(3df,3pd).[37,39] The experimental value of the Gibbs free energy change of hydration of sulfuric acid is also included in Table 2.8 for comparison. For hydration of sulfuric acid, the B3LYP value (-1.00 kcal mol^{-1}) is about 1 kcal mol^{-1} higher than those of PW91PW91 (-2.28 kcal mol^{-1}) and CCSD(T) (-2.23 kcal mol^{-1}). After the BSSE correction, the B3LYP and CCSD(T) values are similar, but smaller than that of PW91PW91. Note for sulfuric acid hydration, the BSSE method yields a more positive value, which differs further from the experimental value (-3.60 kcal mol^{-1}).[126] It has been previously suggested that the BSSE correction may not necessarily improve the accuracy in energetic predictions for molecular complexes, as previously explained by Kurten *et al*.[34] For hydration of oxalic acid, the B3LYP value (0.77 kcal mol^{-1}) is higher than those predicted by CCSD(T) (0.23 kcal mol^{-1}) and PW91PW91 (-1.17 kcal mol^{-1}). After the BSSE correction, the B3LYP (1.42 kcal mol^{-1}) and CCSD(T) (2.42 kcal mol^{-1}) values are higher than that of PW91PW91. Currently, there exists no experimental value of Gibbs free energy changes associated with hydration for dicarboxylic acids in the literature. Herb *et al.*[41] indicated that a comparison of the DFT methods against a high level of ab initio method may not be useful, since few ab inito predictions of stepwise Gibbs free energy changes have been studied systematically and validated against experimental values. Also, the determination of experimental enthalpies typically employs the linearized van't Hoff equation, which may introduce additional errors.[41]

Table 2.8. Changes of Gibbs free energy (Kcal mol^{-1}) for complex formation by sulfuric acid, organic acids, ammonia, and water with and without (in parenthesis) BSSE calculated using B3LYP, PW91PW91, and CCSD(T) with two basis sets, i.e., 6-311++G(2d,2p) and 6-311++G(3df,3pd). Also included in the table for comparison are the experimental data[126] of hydration of sulfuric acid and results previously calculated using PW91PW91/6-311++G(3df,3pd)[37,39].

	B3LYP/6-311++G(2d,2p)	PW91PW91/6-311++G(3df,3pd)//B3LYP/6-311++G(2d,2p)	CCSD(T)/6-311++G(3df,3pd)//B3LYP/6-311++G(2d,2p)	PW91PW91/6-311++(3df,3pd)[37,39]	Exp
SA+W⇔SA-W	-1.00 (-0.300)	-2.72 (-1.97)	-2.23 (-0.13)	-2.28	-3.6±1.0
SA+AM⇔SA-AM	-5.56 (-4.99)	-7.90		-7.77	
SA+SA⇔SA-SA	-3.35 (-2.23)	-5.65		-5.59	
OA+W⇔OA-W	0.77 (1.42)	-1.17 (-0.47)	0.23 (2.42)	-0.96	
OA+AM⇔OA-AM	-2.23 (-1.74)	-4.55		-4.42	
OA+SA⇔OA-SA	-0.71 (0.19)	-2.74		-3.24	
MEA+AM⇔MEA-AM	-3.14 (-3.04)	-5.01		-5.34	
MEA+SA⇔MEA-SA	-2.12 (-1.45)	-4.58		-4.89	

All thermal properties are calculated at the B3LYP level with a 6-311++G (2d, 2p) basis set at 1 atm and 298.15 K. The changes in the electronic energy (with the zero point energy, ZPE, correction), enthalpy, free energy, BSSE, and PW91PW91 corrected free energy of the reaction for the heterodimer complexes are summarized in Table 2.9. The PW91PW91 method consistently predict the energy of about 2.00 kcal mol^{-1} lower than that by B3LYP without BSSE correction. From the electronic energy (with ZPE) changes, the interaction strength of the dicarboxylic acid with sulfuric acid/ammonia/water at 0 K is determined. For the phthalic acid complexes, the interaction of PA with sulfuric acid (-12.69 kcal mol^{-1}) is much stronger than those with ammonia (-10.87 kcal mol^{-1}) and water (-7.91 kcal mol^{-1}), consistent with the previous results of Zhao et al.[47] The geometrical, topological, and NBO analysis shows that PA-SA has one strong hydrogen bond and one medium strength hydrogen bond. In contrast, PA-AM

and PA-W have one strong hydrogen bond and one weak hydrogen bond, and the strong hydrogen bond in PA-AM is stronger than that in PA-W.

Table 2.9. Electronic energy of reaction (ΔE) (with ZPE), enthalpy of reaction (ΔH), free energy of reaction (ΔG) for heterodimer complexes, and BSSE corrected free energy of reactions[a].

Reaction/Energy	ΔE (ZPE)	ΔH	ΔG	ΔS[b]	ΔG(BSSE)	ΔG(PW91PW91/6-311++G(3df,3pd)//B3LYP/6-311++G(2d,2p))
SA+AM⇔SA-AM	-13.27	-13.74	-5.56	-27.43	-4.99	-7.90
OA+AM⇔OA-AM	-9.01	-9.23	-2.23	-25.71	-1.14	-4.55
MOA+AM⇔MOA-AM	-10.98	-11.29	-2.86	-28.28	-2.43	-4.93
MEA+AM⇔MEA-AM	-11.24	-11.54	-3.14	-28.19	-3.04	-5.01
PA+AM⇔PA-AM	-10.87	-11.13	-2.65	-28.44	-2.25	-4.78
SUA+AM⇔SUA-AM	-10.52	-10.83	-2.33	-28.51	-1.93	-4.51
SA+SA⇔SA-SA	-13.14	-13.14	-3.35	-32.84	-2.23	-5.65
OA+SA⇔OA-SA	-10.29	-10.14	-0.71	-32.90	0.59	-2.74
MOA+SA⇔MOA-SA	-12.73	-12.67	-1.86	-36.23	-0.93	-4.23
MEA+SA⇔MEA-SA	-12.58	-12.45	-2.12	-34.63	-1.45	-4.58
PA+SA⇔PA-SA	-12.69	-12.51	-2.11	-34.87	-1.02	-4.37
SUA+SA⇔SUA-SA	-12.82	-12.68	-2.43	-34.39	-1.47	-4.93
SA+W⇔SA-W	-9.06	-9.71	-1.00	-29.19	-0.30	-2.72
OA+W⇔OA-W	-5.51	-5.95	0.77	-27.94	2.95	-1.17
MOA+W⇔MOA-W	-7.81	-8.36	1.00	-31.40	1.56	-0.58
MEA+W⇔MEA-W	-7.98	-8.48	0.53	-30.24	0.81	-1.07
PA+W⇔PA-W	-7.91	-8.40	0.74	-30.63	1.31	-1.06
SUA+W⇔SUA-W	-7.60	-8.12	0.92	-30.31	1.48	-0.70

a. Energy in kcal mol^{-1} at B3LYP/6-311++G(2d,2p) level.
b. Entropy in cal mol^{-1} K^{-1} at B3LYP/6-311++G(2d,2p) level.

To obtain the thermochemical properties of the molecular complexes under atmospheric conditions, the temperature effect needs to be taken into account. At 298.15 K, the interaction of dicarboxylic acids with sulfuric acid/ammonia/water includes the contributions from the translational, rotational and vibrational energies, and the thermochemical properties of the molecular complexes are related to enthalpy and entropy. If only enthalpy is considered, the interaction of PA with sulfuric acid is the strongest, followed by those with ammonia and water, since the enthalpy changes of reaction are -12.51, -11.13, and -8.40 kcal mol^{-1} for PA-SA, PA-AM, and PA-W, respectively. However, when incorporating the entropy changes, the interaction of PA with ammonia (-2.25 kcal mol^{-1}) becomes the strongest, followed by those with sulfuric acid (-1.02 kcal mol^{-1}) and water (1.31 kcal mol^{-1}). The entropy changes also consist of the translational, rotational and vibrational entropy components, and the values of the translational, rotational and vibrational entropies for the complexes between PA with sulfuric acid, ammonia, and water are listed in Table 2.10. The translational entropy changes represent the most important term in the total entropy changes; this arises since the number of molecules decreases from two for the heterodimer complex to one for the PA monomer in the association reaction. The changes in the rotational and vibrational entropy nearly cancel out each other. Since the translational entropy depends not only on the temperature but also on the number concentration of the molecules, the relative stability of the PA-SA, PA-AM and PA-W complexes varies with the concentrations of those species in the atmosphere. At the concentrations corresponding to 1 atm and 298.15 K, the total entropy changes are practically independent of the structures of the molecules and only vary with the type of interaction, i.e., about -34 cal mol^{-1} K^{-1} for SA with dicarboxylic acids, about -28 cal mol^{-1} K^{-1} for ammonia with dicarboxylic acids and -30 cal mol^{-1} K^{-1} for water with dicarboxylic acids. The entropy changes for the heterotrimer complexes, SA-PA-SA and SA-PA-AM, are also presented in Table 2.11. The total entropy changes of reaction

for the SA-PA-SA (-33.90 cal $mol^{-1} K^{-1}$) and SA-PA-AM (-26.71 cal $mol^{-1} K^{-1}$) complexes are close to those for PA-SA (-34.87 cal $mol^{-1} K^{-1}$) and PA-AM (-28.45 cal $mol^{-1} K^{-1}$), indicating that the interaction of PA with SA and AM in heterotrimer complexes is similar to that in the corresponding heterodimer complexes.

The thermochemical properties of the heterotrimer complexes are presented in Table 2.11. The complexes of SUA with two sulfuric acid molecules are discussed to illustrate the heterotrimer interaction. There are two possible interactions in the heterotrimer complexes, i.e., SA-SUA-SA and SUA-SA-SA. For SA-SUA-SA, two conformations are obtained from the geometry optimization. The free energy for conformation II is lower than that for conformation I. There exists no intramolecular hydrogen bond within the succinic acid molecule for conformation II, but in conformation I succinic acid retains its intramolecular hydrogen bond, consistent with that discussed in the geometrical analysis section. The enthalpies of reaction for heterotrimer complexes are similar to those for heterodimer complexes. For example, the enthalpy of reaction for PA-AM (-11.13 kcal mol^{-1}) is close to that for SA-PA-AM (-12.56 kcal mol^{-1}) from the association reaction of SA-PA and AM. This implies that the formation of heterotrimer complexes from heterodimer complexes is as favorable as that of heterodimer complexes.

Table 2.10. Translational (ΔS_{tr}), rotational (ΔS_{rot}), vibrational (ΔS_{vib}), and total (ΔS_{total}) entropy changes of reaction (in cal mol^{-1} K^{-1}) for heterodimer and heterotrimer complexes of phthalic acid with sulfuric acid, ammonia, and water at B3LYP/6-311++G(2d,2p) level.

Complex	ΔS_{tr}	ΔS_{rot}	ΔS_{vib}	ΔS_{total}
PA-AM	-34.15	-10.42	16.12	-28.45
PA-SA	-38.27	-20.92	24.32	-34.87
PA-W	-34.30	-9.48	13.15	-30.63
SA-PA-SA[a]	-38.72	-21.86	26.68	-33.90
SA-PA-AM[b]	-34.26	-10.81	18.35	-26.71

a. SA-PA-SA is formed through the association reaction of SA-PA with SA
b. SA-PA-AM is formed through the association reaction of SA-PA with AM

Table 2.11. Electronic energy (ΔE), enthalpy (ΔH), free energy (ΔG) and entropy changes of reaction (ΔS) for heterotrimer molecular complexes [a].

Reaction	ΔE(ZPE)	ΔH	ΔG(B3LYP)	ΔS	ΔG(PW91PW91/6-311++G(3df,3pd)// B3LYP/6-311++G(2d,2p))
SA+OA-SA⇔SA-OA-SA	-10.40	-9.94	-0.11	-31.72	-1.85
SA+OA-SA⇔OA-SA-SA	-13.27	-13.12	-3.14	-32.23	-5.68
SA+SUA-SA⇔SA-SUA-SA(I)	-11.73	-11.43	-1.72	-32.57	-2.94
SA+SUA-SA⇔SA-SUA-SA(II)	-18.64	-18.49	-8.44	-33.69	-9.71
SA+SUA-SA⇔SUA-SA-SA	-13.26	-13.24	-2.93	-34.55	-5.27
W+OA-SA⇔OA-SA-W	-9.32	-9.84	-0.90	-28.69	-2.64
W+OA-SA⇔W-OA-SA	-7.50	-7.87	1.01	-28.53	-0.42
W+SUA-SA⇔W-SUA-SA(I)	-3.40	-3.39	3.04	-21.56	2.18
W+SUA-SA⇔W-SUA-SA(II)	-11.19	-11.71	-3.06	-29.00	-4.31
W+SUA-SA⇔SUA-SA-W	-9.35	-9.97	-0.97	-30.22	-2.79
OA-SA+AM⇔OA-SA-AM	-14.49	-15.00	-6.05	-28.76	-8.81
OA-SA+AM⇔SA-OA-AM	-11.08	-11.16	-3.83	-23.34	-5.83
SUA-SA+AM⇔SUA-SA-AM	-14.16	-14.70	-5.90	-29.50	-8.58

Table 2.11. Continued

Reaction	Δ*E*(ZPE)	Δ*H*	Δ*G*(B3LYP)	Δ*S*	Δ*G*(PW91PW91/6-311++G(3df,3pd)//B3LYP/6-311++G(2d,2p))
SUA-SA+AM⇔SA-SUA-AM	-13.43	-13.62	-5.62	-26.86	-7.22
PA-SA+AM⇔SA-PA-AM	-12.47	-12.56	-4.59	-26.71	-6.01
PA-SA+SA⇔SA-PA-SA	-17.70	-17.41	-7.31	-33.90	-9.33
PA-AM+SA⇔SA-PA-AM	-14.30	-13.93	-4.05	-33.14	-5.61

a. The thermal data are from B3LYP/6-311++G(2d,2p) calculation. Energy in kcal mol^{-1}. Entropy in cal mol^{-1} K^{-1}

The thermochemical analysis may be subject to a possible error caused by the approximation of the internal rotor using harmonic oscillator. To quantify this effect, hindered internal rotor analysis is carried out for PA using Gaussian 03 package.[112] The McClurg's[127,128] free energy correction of 0.02 kcal mol^{-1} is one order of magnitude smaller than that reported by Ehn *et al.* (0.5 kcal mol^{-1}).[109] Hence, the harmonic approximation of internal rotor does not introduce a significant error in our study. Another possible source of errors includes neglecting of the gas-phase hydration effect[38], which may be important for complex formation in the atmosphere and will be assessed in future studies. It should also be pointed out that the concentrations of the aerosol precursors (excluding water vapor) in the atmosphere are relatively small and the equilibrium for the formation of the pre-nucleation molecular complexes is rarely established. Hence, cautions need to be exercised to predict the equilibrium distributions of those pre-nucleation molecular complexes using the theoretically predicted free energies and the gaseous concentrations of sulfuric acid, ammonia, and organic acids. Furthermore, the free energies predicted in Tables 2.9 and 2.11 do not account for the liquid-like properties for the pre-nucleation molecular complexes. There typically exists a nucleation barrier, as demonstrated in

supersaturation phenomenon, to overcome the entropy restriction during the initial stage of a phase transformation.[99] The quantum chemical calculations likely overestimate the translational entropy by treating the pre-nucleation molecular clusters as ideal gases. Indeed, the free energies predicted by quantum chemical calculations fail to exhibit an activation barrier, in contrast to that predicted by the classical nucleation theory, as discussed analogously by Reiss et al. on the translational-rotational paradox.[129].

2.4 Summary and conclusion

DFT, QTAIM, and NBO methods have been applied to investigate the interaction of selected dicarboxylic acids (i.e., oxalic acid, malonic acid, maleic acid, phthalic acid, and succinic acid) with common atmospheric aerosol nucleation precursors (i.e., sulfuric acid, ammonia, and water). B3LYP density functional with 6-311++G(2d,2p) basis set is applied to obtain the energetics of the molecular cluster formation**.** Comparisons are made between the predictions using several different theoretical methods and with the experimental results. The geometrical, topological, and NBO analysis shows that the dicarboxylic-sulfuric acid complex has one strong hydrogen bond and one medium strength hydrogen bond, similar to those mono carboxylic acids previously reported.[47] The heterodimer interaction shows that at 0 K dicarboxylic acids have the strongest interactions with sulfuric acid, followed by those with ammonia and water. At room temperature, due to the contribution from entropy changes of reaction, dicarboxylic acids have the strongest interaction with ammonia, followed by those with sulfuric acid and water. The heterotrimer interaction shows that dicarboxylic acids bind with two sulfuric acid molecules, and the resulting complex is hydrophilic in both ends. The geometrical analysis of the heterotrimer dicarboxylic acid-sulfuric acid complexes exhibit similar characteristic as those of the heterodimer dicarboxylic acid complexes, i.e., with one strong hydrogen bond and one medium strength hydrogen bond on each side of the carboxylic

functional group. The enthalpies of reaction for heterotrimer complexes are similar to those for heterodimer complexes, indicating that the formation of heterotrimer complexes from heterodimer complexes is as favorable as that of heterodimer complexes.

Sulfuric acid has been commonly considered as a key species in atmospheric new particle formation.[81] However, it well recognized that the atmospheric concentration of gas-phase sulfuric acid is typically too low to explain nucleation and growth of atmospheric nanoparticles.[81,130] Binary nucleation of the sulfuric acid/water system alone is insufficient to explain nucleation rates observed in field measurements of diverse environmental conditions, i.e., urban, rural, remote continental, free troposphere, and coastal areas. Mono carboxylic acids, formed from photochemical oxidation of anthropogenic and biogenic hydrocarbons have been identified as an important element in the aerosol nucleation process.[45,46] Oxalic acid, malonic acid, maleic acid, phthalic acid, and succinic acid investigated in this study are the most abundant forms of dicarboxylic acids in the atmosphere. The free energies of formation of the heterodimer and heterotrimer clusters suggest that dicarboxylic acids can contribute to the aerosol nucleation process by binding to sulfuric acid and ammonia. In particular, the formation energies and structures of the heterotrimer clusters show that dicarboxylic acids enhance nucleation in two directions, in contrast to monocarboxylic acids. As a result, the heterodimer and heterotrimer complexes of dicarboxylic acids likely act as the linking elements in sulfuric acid/ammonia/water nucleation. Future experimental studies are required to investigate the contribution of dicarboxylic acids to aerosol nucleation under atmospheric conditions.

3. THE CRITIAL ROLE OF HYDRATION IN NUCLEATION PRECURSOR INTERACTION*

3.1 Introduction

The formation and growth mechanisms of aerosols represent one of the key research areas in atmospheric chemistry, because of the importance of aerosols in affecting the Earth climate and human health.[57-59] Aerosols exert strong radiative forcing on climate by scattering and absorbing a fraction of the incoming sunlight,[131] which is commonly referred to as the direct effect. Also, aerosols act as cloud condensation nuclei (CCN) or ice nuclei (IN) and subsequently impact the development, lifetime, and albedo of clouds,[132,133] indirectly affecting the Earth radiation budget.[59] The aerosol direct and indirect forcings represent the most uncertain components in projections of the future climate.[57] In addition, multi-phase reactions occurring on aerosol surfaces can play a key role in affecting atmospheric trace constitutes.[60,104,105,134,135]

Atmospheric aerosols are typically divided into two categories, i.e., primary and secondary, on the basis of their formation in the atmosphere. Primary aerosols are emitted directly into the atmosphere from natural or anthropogenic sources, while secondary aerosols are formed via gas to particle conversion. Although a large portion of atmospheric aerosols is secondary and formed through nucleation and growth of nanoparticles, the mechanism of secondary aerosol formation remains highly uncertain, preventing the development of physically-based representation of those processes in atmospheric models.[63] New particle formation occurs in two distinct stages, i.e., nucleation to form critical nuclei and subsequent

* Reprinted with permission from Xu, W., & Zhang, R. (2013). A theoretical study of hydrated molecular clusters of amines and dicarboxylic acids. *The Journal of Chemical Physics, 139*(6), 064312, Copyright (2013), American Institute of Physics.

growth of freshly nucleated particles to larger sizes.[51] Formation of the critical nucleus is restricted by entropy and a Gibbs free energy barrier exists prior to spontaneous transformation into the new phase. Also, there exists a large Kelvin effect for the growth of nanoparticles, because of elevated equilibrium vapor pressures above curved surfaces, which acts as another major limitation in the new particle formation process.

Sulfuric acid has been identified as an important precursor in atmospheric aerosol formation.[51,136] To explain the nucleation of sulfuric acid and water from a molecular point of view, experimental and computational studies of gaseous complexes of sulfuric acid and water have been carried out.[137-140] A previous matrix isolation infrared spectroscopy study showed that the most stable isomer of (SA)(W) complex corresponded to the one with water acting as proton acceptor, although no spectra evidence for proton transfer was found in that study.[137] Another density functional study revealed the coexistence of neutral and ion-pair clusters of hydrated sulfuric acid $(SA)(W)_n$ (n=1-5),[138] showing that the proton transferred form of $(SA)(W)_5$ is 2 kcal mol^{-1} more stable than the hydrogen bonded neutral form.[138] Recently, Sugawara *et al.* employed the semiempirical path-integral molecular dynamics simulation to investigate the proton transfer process in hydrated sulfuric acid clusters and found that the distance between O in sulfuric acid and O in the proton-accepting water and the water coordination number of the proton-accepting water played an important role in the proton transfer process.[139]

However, the binary nucleation involving sulfuric acid and water has been commonly recognized to be insufficient to explain field measured nucleation events and its dependence on the sulfuric acid concentration, since the gaseous concentration of sulfuric acid is very low, typically on the sub parts per trillion (ppt) level.[82] Several other mechanisms, such as ternary nucleation by sulfuric acid/water/ammonia/amines,[31,32,40,141] ion induced nucleation,[66,142,143] and

organic acid assisted nucleation,[45,46,68,106] have been suggested to account for new particle formation under different ambient conditions.

Numerous experimental and theoretical studies have shown that amines and organic acids enhance nucleation rate in multi-compound systems consisting of sulfuric acid and water.[51] For example, theoretical studies on the interaction of amines and carboxylic acids with sulfuric acid show that both amines and carboxylic acids bind strongly to sulfuric acid via hydrogen bonding.[31,32,34,37,39,40,43,47] Zhao *et al.* showed that monocarboxylic acids form one strong and one medium strength hydrogen bond with sulfuric acid using density functional theory (DFT) and atom in molecules (AIM) analysis.[47] The strength of hydrogen bonding is classified using the O-H bond length, second order NBO interaction energy, or the charge density in AIM analysis. The strong hydrogen bond has an O-H length of 1.000-1.016 Å, a second order Natural bond orbital (NBO) interaction energy of 26.84-38.06 kcal mol^{-1}, and a charge density of 4.77-5.58 (10^{-2} a.u.), while the weak hydrogen bond has an O-H length of about 0.968 Å, a second order NBO interaction energy of 0.10-2.05 kcal mol^{-1}, and a charge density of about 1.70 (10^{-2} a.u.).[43,47] Theoretical studies have revealed a barrierless hydrolysis of sulfur trioxides catalyzed by organic acid in the gas phase.[47] The importance of the reactions of organic acids with protonated water clusters in the formation of pre-nucleation embryos have been demonstrated experimentally.[144,145] In addition, the interaction of dicarboxylic acids with sulfuric acids has been investigated in theoretical studies. For example, maleic acid has been suggested to form stable clusters with both neutral and ionic sulfuric acid clusters, while oxalic acid only forms stable ionic clusters with sulfuric acid.[37,39] Anionic clusters of bisulfate have been shown to be stabilized by oxalic, malonic, and succinic acids, on the basis of the theoretical work by Ehn *et al.*[109] NBO and AIM analyses have also shown that dicarboxylic acids form one strong and one medium strength hydrogen bond in both ends,[43] indicating that dicarboxylic acids can serve as an

important element in nucleation involving sulfuric acid water. Furthermore, theoretical work has been performed on the interaction of amines with sulfuric acid. Kurten *et al.* suggested that amines enhance the neutral and ion induced sulfuric acid-water nucleation more effective than ammonia.[31] In contrast, Nadykto *et al.* showed that although amines form strong hydrogen bond clusters with sulfuric acid, the enhancement effect of amines may not be comparable with that by ammonia, because of a much higher atmospheric concentration of ammonia than amines.[40] Since the free energy changes of cluster formation are highly sensitive to both calculation levels of theory and conformation sampling methods, the relative effect between amines with ammonia on aerosol nucleation is still controversial and requires further investigation.[34] Experimental and theoretical studies have also been performed to investigate the interaction between amines and charged clusters consisting of sulfuric acid and ammonia sulfate.[146-149]

Recent experimental studies have shown that a trace amount of amines considerably enhances nucleation of sulfuric acid-water system.[83,150,151] However, the available experimental studies do not differentiate the role of amines in the two distinct stages of new particle formation, i.e., whether amines enhance new particle formation by overcoming the free energy nucleation barrier through forming stable molecular complexes with sulfuric acid or by overcoming the Kelvin barrier through stabilizing freshly nucleated acidic particles. Furthermore, the gaseous concentration of amines in the atmosphere is typically several orders of magnitude lower than those of organic acids. It has been suggested that the molecular complexes containing organic acids may represent an important form in aerosol nucleation under atmospheric conditions.[43,47] On the other hand, it has been shown that organic acids contribute negligibly to the growth of nanoparticle, because of their hydrophobicity.[46]

Although the effect of carboxylic acids and amines on sulfuric acid-water nucleation has been focused in numerous previous theoretical calculations, the interaction between dicarboxylic

acids and amines in the presence of hydration effect has yet to be investigated. In the present study, theoretical calculations of hydrated molecular clusters consisting of succinic acid (SUA) and dimethylamine (DMA) are carried out to illustrate the interaction between dicarboxylic acids and amines. Succinic acid is chosen, since it represents one of the common dicarboxylic acids frequently observed in ambient aerosols.[152] The free energy changes of the interactions of succinic and sulfuric acids with dimethylamine in the presence of water (W) are calculated through a two consecutive step process, i.e., the Basin Paving Monte Carlo (BPMC) conformational sampling and subsequent geometry optimization and frequency calculations using density functional theory (DFT). The atmospheric implications of the present results on nucleation of atmospheric nanoparticles are discussed.

3.2 Theoretical methods

In each Monte Carlo (MC) trial, the atom and its Cartesian coordinate are randomly selected. The step of the atomic movement is also a random number with the largest magnitude of 0.5 Å. The local energy minimizations in BPMC are carried out employing Amber11 software package[153] through an interface FORTRAN code. The BPMC is based on the Basin Hopping Monte Carlo (BHMC) approach, which increases the Monte Carlo transition probability by transforming the original energy landscape into a stepwise energy landscape.[154] Another term for the BPMC, which is proportional to the energy histogram, is introduced in the simulation to the transformed energy landscape.[155] This modification further helps the molecular system to escape from the local energy minimum trap. A detailed description of the basin hopping and basin paving algorithms has been previously discussed.[154,155] Recently, another algorithm based on BPMC by varying temperature in the simulation has been developed.[156] In our BPMC simulation, the Generalized Amber Force Field (GAFF) implemented in antechamber tools is used to describe dimethylamine and succinic acid.[157,158] The force field parameters of sulfuric acid and

bisulfate ion are taken from the study by Loukonen *et al.*[32] TIP3P model is employed for water molecules.[159] Since proton transfer can occur for sulfuric acid-dimethylamine clusters, bisulfate anion and dimethylamminium cation are used in the BPMC simulation, instead of sulfuric acid and dimethylamine. For $(SA)(W)_n$ cluster with *n* greater than 2, bisulfate and hydronium ions are employed in the BPMC simulation.

On the basis of the conformations obtained by BPMC, the geometries are taken in further optimization and frequency calculations at PW91PW91 level of theory with the basis set 6-311++G(2d,2p). The PW91PW91 density functional has been widely employed and shown to reproduce accurately the experimental value of the free energy change of first hydration of sulfuric acid.[35] In addition, the first hydration of sulfuric acid is also studied at MP2 and CCSD(T) levels of theory. It is found that the PW91PW91 method well reproduces the MP2 and CCSD(T) results. The values of first hydration free energy of sulfuric acid at the three levels of theory and the experimental value are listed in Table 3.1.[160] All the density functional geometry optimization and frequencies calculations are carried out using Gaussian 09 software package.[161] Thermodynamic properties, such as enthalpy, entropy, and Gibbs free energies, are calculated using unscaled density functional frequencies at standard temperature and pressure conditions (STP). The formulas and theory used in calculating the thermodynamic properties have been described previously by the Gaussian, Inc.[162] Both molecular dynamics and Monte Carlo simulation have been previously employed to obtain the distribution of conformers.[163] On the basis of the structures of the conformers, reliable Gibbs free energies for clusters have been obtained through Boltzmann averaging of the Gibbs free energy of each conformer, which can be calculated using the scaled or unscaled harmonic vibrational frequencies.[163]

Table 3.1. Theoretical and experimental values of the first hydration free energy of sulfuric acid in kcal mol^{-1}.

	PW91PW91/6-311++G(2d,2p)	MP2/6-311++G(2d,2p)	CCSD(T)/6-311++G(2d,2p)//MP2/6-311++G(2d,2p)	Experiment[160]
SA+W⇔SA-W	-2.08	-1.78	-3.48	-3.6±1.0

Molecular graphics are generated using MOLDEN software package.[164] The display option for hydrogen bonding is chosen so that the minimum and maximum distances (angles) for hydrogen bonding are 1.5 (145) and 3.15 (215) Å (degrees), respectively. Basis set superposition errors (BSSE) are not included in the present calculation, since there are significant controversies concerning the applicability of BSSE to molecular complexes, such as strong acid and base complex, in which the original acid and base monomeric unit does not exist as a result of proton transfer.[34]

3.3 Results and discussion

3.3.1 Conformational analysis of $(SA)(W)_2$ and $(SA)(W)_5$ cluster

In the present work, the BPMC sampling results of $(SA)(W)_2$ and $(SA)(W)_5$ are used to illustrate the validity of our method. Since the relative position and orientation as well as the conformation of monomers vary in molecular clusters, it is important to note that the monomer in molecular clusters cannot be treated as a rigid body. At each time when a new energy conformation is identified, the energy and the corresponding geometry are recorded. The criterion in selecting a new conformation relies on the consideration that the three principal moments of the inertia and energy of a conformation are different from those of previously recorded conformations. Figure 3.1 indicates that with BPMC the MC trial readily avoids the

local energy minimum trap. Figure 3.2 shows the potential energy histogram of $(SA)(W)_2$ cluster obtained from the BPMC simulation. Because the energy order may change from MM to DFT level, it is important to estimate the error caused by using the MM global minimum as the DFT calculation starting point to obtain the cluster Gibbs free energy.

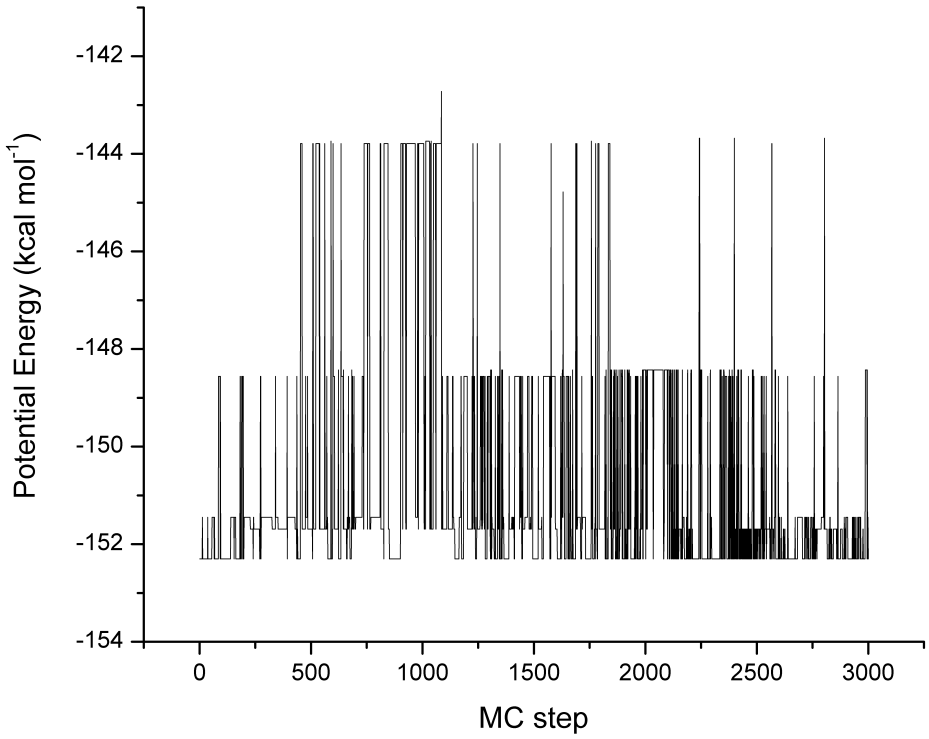

Figure 3.1. Plot of potential energy of $(SA)(W)_2$ cluster versus the MC step number.

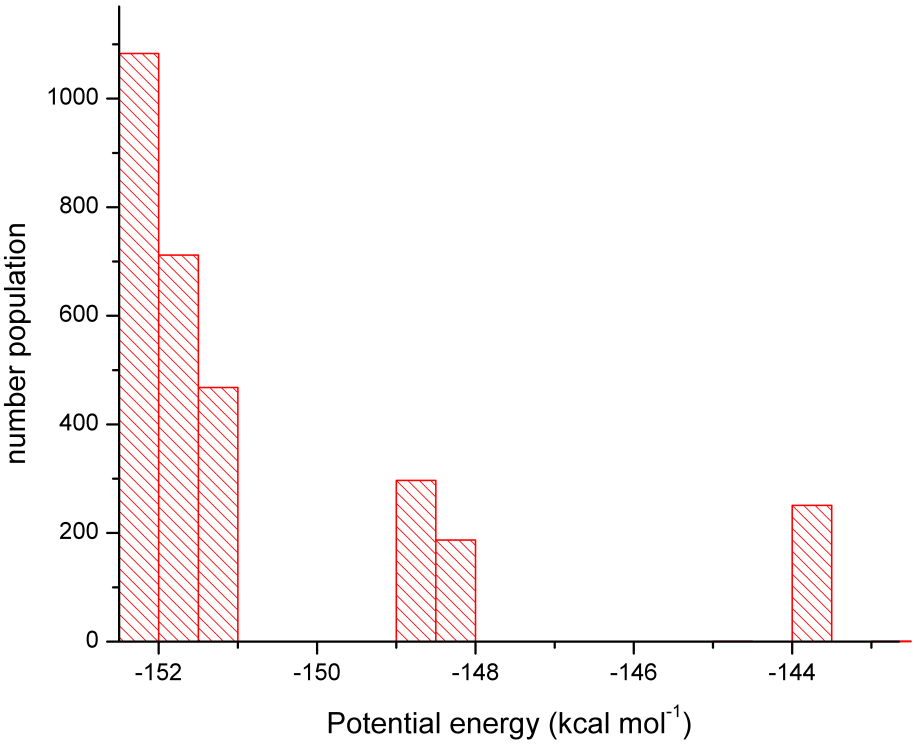

Figure 3.2. Histogram of potential energy distribution of $(SA)(W)_2$ conformers.

Ten conformers of $(SA)(W)_2$ cluster are obtained using BPMC at MM level (Figure 3.3). The conformers are subsequently optimized at DFT level and the equilibrium structures are shown in Figure 3.4. The relative potential energies to the first conformer at MM and DFT levels are summarized in Table 3.2. The results show that the global minimum of $(SA)(W)_2$ cluster corresponds to the first conformer with two water molecules on the same side forming a cyclic structure, consistent with results by Re *et al.* and Sugawara *et al.*[138,139] The second lowest energy conformer at both MM and DFT level corresponds to conformer IV, with two water molecules on opposite sides of sulfuric acid forming two cyclic structures. Conformer IV exhibits an

energy difference of 0.61 and 0.11 kcal mol^{-1} from conformer I at MM and DFT level, respectively, compared with 0.7 kcal mol^{-1} by Re *et al.* at B3LYP/D95++(d,p) level and 0.43 kcal mol^{-1} by Sugawara *et al.* at PM6/SRP2 level.[138,139] The two O=S-O-H dihedrals of sulfuric acid are 38.85 and 34.21 degrees in conformer I, and are 29.1 and 61.58 degrees in conformer V. The energy of conformer V at DFT level is 0.46 kcal mol^{-1}, which is slightly higher than that of conformers I and IV (0.11 kcal mol^{-1}). Conformers II and IX are different from those previously reported by Re *et al.* and Sugawara *et al.*[138,139] Conformers VII and X have been previously identified by Re *et al.*, with the relative energies of 4.2 and 2.2 kcal mol^{-1} at B3LYP/D95(d,p) level of theory, respectively, compared with 3.94 and 1.40 kcal mol^{-1} in the present study at PW91PW91/6-311++G(2d,2p) level of theory. Boltzmann averaging of the available conformers at room temperature (298.15 K) shows that the correction to Gibbs free energy of cluster is only 0.27 (0.23 for DFT level) kcal mol^{-1}, when global minimum is used to approximate the cluster Gibbs free energy.

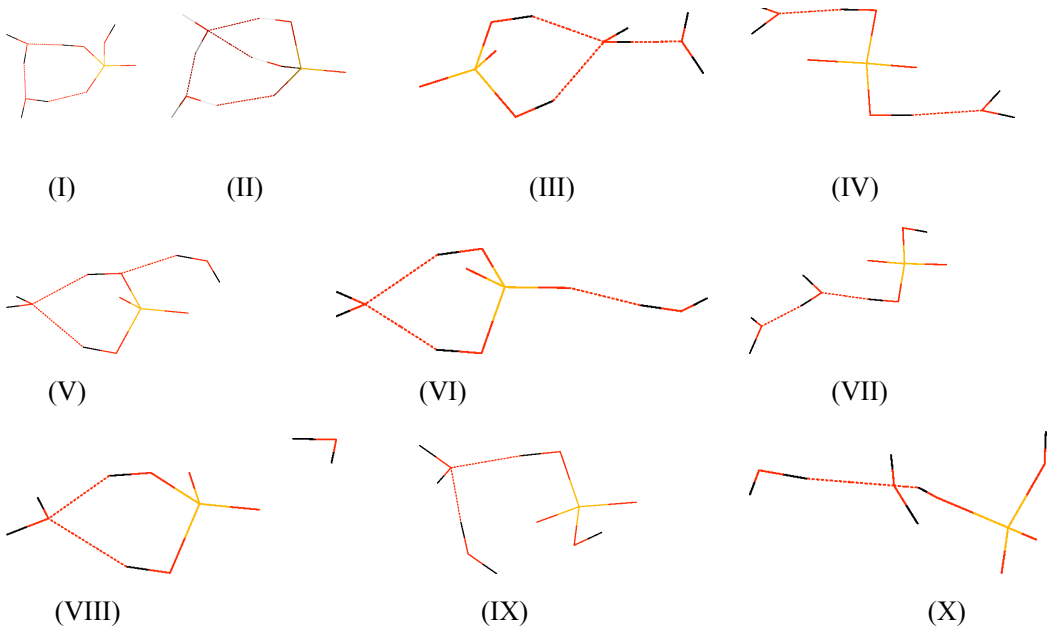

Figure 3.3. List of possible conformations of $(SA)(W)_2$ found by BPMC method at molecular mechanics (MM) level.

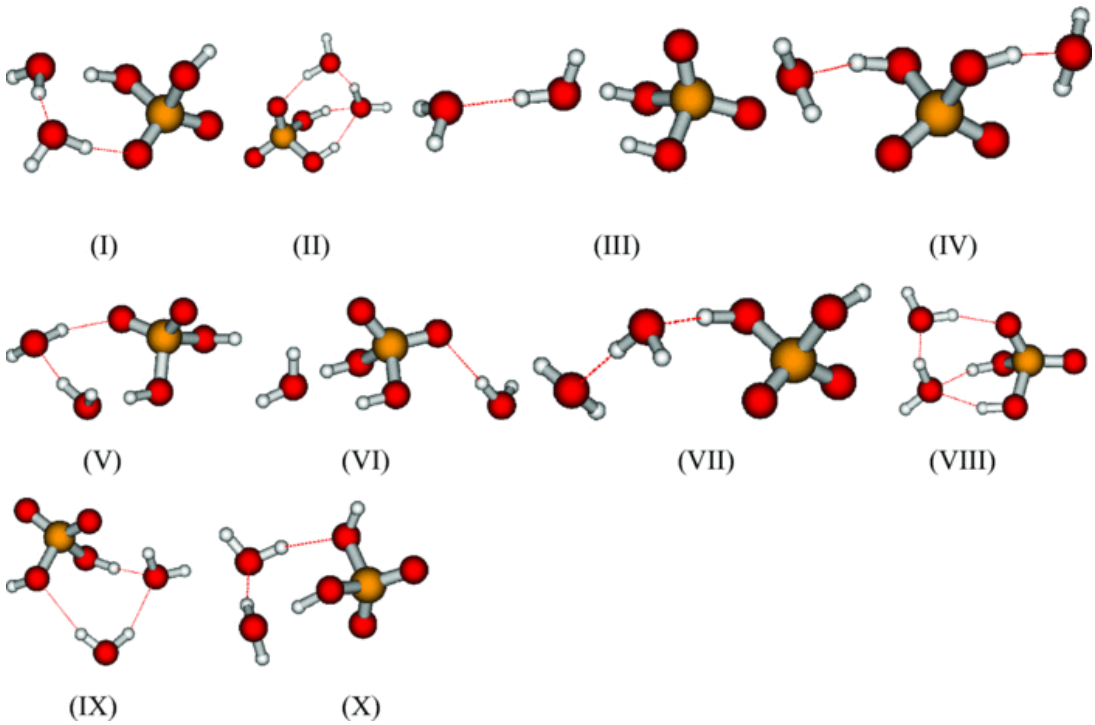

Figure 3.4. Conformations of $(SA)(W)_2$ optimized at PW91PW91/6-311++G(2d,2p) level.

Table 3.2. Conformations of $(SA)(W)_2$ identified by BPMC method at molecular mechanics (MM) level and their corresponding electronic energies (relative to the first conformation) at both MM and DFT levels.

Conformation #	MM (kcal mol^{-1})	PW91PW91/6-311++G(2d,2p) (kcal mol^{-1})	B3LYP/D95(d,p) (kcal mol^{-1})[b]	PM6/SRP2 (kcal mol^{-1})[c]
I	0.00	0.00	0.00	0.00
II	0.85	1.45[a]		
III	3.74	6.28		
IV	0.61	0.11	0.30 (0.70[d])	0.43
V	8.51	0.46		
VI	8.56	11.64		
VII	3.87	3.94	4.20	
VIII	9.58	1.45[a]		
IX	7.52	8.80		
X	8.62	1.40	2.20	
Boltzmann average at RT	0.27	0.23		

[a] II and VIII conformation at DFT level is the same.
[b] Reference 138; [c] Reference 139; [d] At B3LYP/D95++(d,p) level of theory.

For $(SA)(W)_5$ cluster, since proton transfer exists in the cluster, bisulfate and hydronium ions are used for the simulation. Among various conformers obtained, only the lowest four structures are further optimized at DFT level. The relative electronic energies of the four conformers at MM and DFT levels are presented in Table 3.3, and their corresponding structures are shown in Figure 3.5. Conformer IV obtained in the current study is similar to those of the global minimum obtained by Re *et al.* and Loukonen *et al.*[32,138]

Table 3.3. Conformations of $(SA)(W)_5$ identified by BPMC method at molecular mechanics (MM) level and their corresponding electronic energies (relative to the fourth conformation) at both MM and DFT levels

Conformation #	MM (kcal mol^{-1})	PW91PW91/6-311++G(2d,2p) (kcal mol^{-1})
I	3.11	2.07
II	2.19	1.56
III	3.36	3.96
IV	0.00	0.00

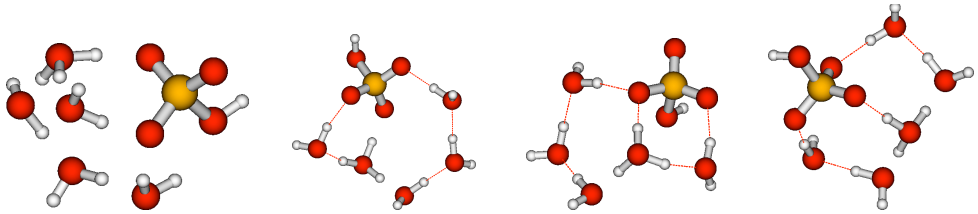

(I) (II) (III) (IV)

Figure 3.5. List of four possible conformers of $(SA)(W)_5$.

3.3.2 Conformational analysis of SUA-DMA-nW molecular clusters

In Figure 3.6, the structures of sulfuric and succinic acids and dimethylamine clusters with 0-6 molecules of water are presented. Only the conformers with the lowest potential energy at MM level are subsequently optimized at PW91PW91/6-311++G(2d,2p) level of theory. The structures of the sulfuric acid-water clusters are compared with those obtained by Temelso *et al.*[163] The two hydrogen bond lengths of 2.08 and 1.62 Å for the (SA)(W) cluster in the present study compare favorably with those of 2.16 and 1.68 Å by Temelso *et al.*[163] For the $(SA)(W)_2$ cluster, only the structures corresponding to A1 (IV) and C1 (I) in the work by Temelso *et al.*[163] are identified in the present work. A possible explanation is that the force field applied to

sulfuric acid in our study is different from the GAFF force field applied by Temelso *et al.*[163] In addition, the energy order between A1 (IV) and C1 (I) in the present study is reversed, compared with that by Temelso *et al.*, which likely is caused by different levels of theories employed in the two studies.[163] The three hydrogen bond lengths of 1.83, 1.67, and 1.49 Å for the C1(I) conformer of $(SA)(W)_2$ cluster in the present study are also similar to those of 1.91, 1.76, and 1.58 Å by Temelso *et al.*[163] As the number of water molecules increase, the number of possible conformers increases significantly. For the $(SA)(W)_3$ cluster, the most stable conformer corresponds to the ionized state according to Re *et al.* and Loukonen *et al.*[32,138] However, according to Temelso *et al.*, the neutral form is the global minimum.[163] In the present study, the ionized state is 1.59 kcal mol^{-1} more stable than the lowest energy neutral form. For clusters $(SA)(W)_n$ ($n \geq 4$), the most stable conformer corresponds to the ionized state.

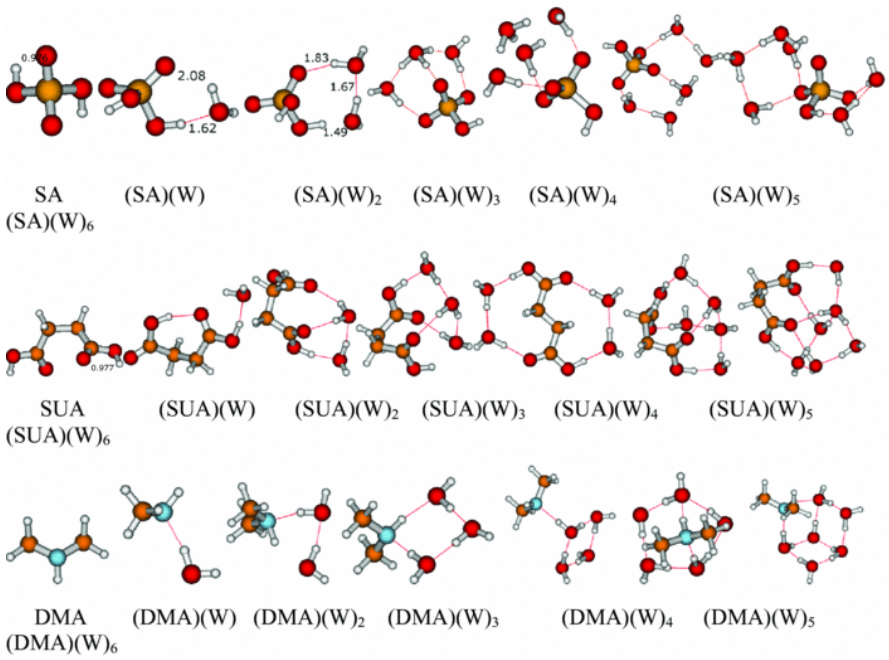

Figure 3.6. Optimized geometries of sulfuric/succinic acids and dimethylamine hydrated cluster with number of water molecules ranges from 0 to 6.

The stable conformers of succinic acid and dimethylamine with water clusters are also shown in Figure 3.6. The succinic acid - water cluster conformations are rather complicated, since succinic acid exists in several different conformations. In contrast, the cluster conformations containing dimethylamine - water are relatively simple. For example the $(DMA)(W)_2$ and $(DMA)(W)_3$ clusters exhibit similar structures to those of W_3 and W_4 clusters, respectively. $(DMA)(W)_4$ and $(DMA)(W)_5$ contain a cyclic water tetramer and pentamer, respectively. Both tetrameric and pentameric rings are essential in building the structures for water clusters.[165] $(DMA)(W)_6$ shows a similar structure to that of W_8 containing a cubic cage,[165] but one corner of the cubic cage is absent in the structure of the former.

The structures of succinic and sulfuric acids with dimethylamine hydrated clusters are presented in Figure 3.7. All of the clusters containing sulfuric acid exhibit proton transfer from sulfuric acid to dimethylamine. The OH bond length in a free sulfuric acid monomer is 0.976 Å, while after bonding with dimethylamine the OH bond is elongated to 1.686 Å, indicative of the transfer of proton from oxygen (sulfuric acid) to nitrogen (dimethylamine). In contrast, proton transfer does not occur in clusters of succinic acid with dimethylamine with 0-3 molecules of water. The OH bond length in free succinic acid monomer is 0.977 Å, while after bonding with dimethylamine the OH bond length is 1.085 Å, which does not vary appreciably from the value of a free monomer. When the degree of hydration of the cluster is smaller than 3, the OH bond length in succinic acid varies in a small range, from 1.068 to 1.121 Å. Further increasing number of water molecules (greater than 3) tends to promote proton transfer from succinic acid to dimethylamine and facilitates the formation of contact ion pairs. The OH bond length of succinic acid in $(SUA)(DMA)(W)_4$ is 1.478 Å, which is significantly larger than the value 1.068 Å prior to proton transfer. The resulting aminium and dicarboxylate ion pair is stabilized by water molecules through hydrogen bonding interaction. Compared with the interaction of sulfuric acid

with dimethylamine, the interaction of succinic acid with dimethylamine has a weaker strength, according to the change of O-H bond length.[43] This conclusion is also corroborated in the thermochemical analysis to be discussed below. The (SA)(DMA), (SA)(DMA)(W), and $(SA)(DMA)(W)_2$ structures have been reported previously by Nadykto *et al.*,[40] while Kurten *et al.* has reported the structure of (SA)(DMA).[31] A more comprehensive study on the structure and energetics of sulfuric acid and dimethylamine hydrated clusters has been reported by Loukonen *et al.*[32] The structures of (SA)(DMA) and (SA)(DMA)(W) clusters in the present study are consistent with those by Loukonen *et al.*[32,40] and Nadykto *et al.*[40] The structures of $(SA)(DMA)(W)_n$ ($n \geq 2$) in the present work are different from those reported by Loukonen *et al.*, which is probably caused by the different level of theory employed.

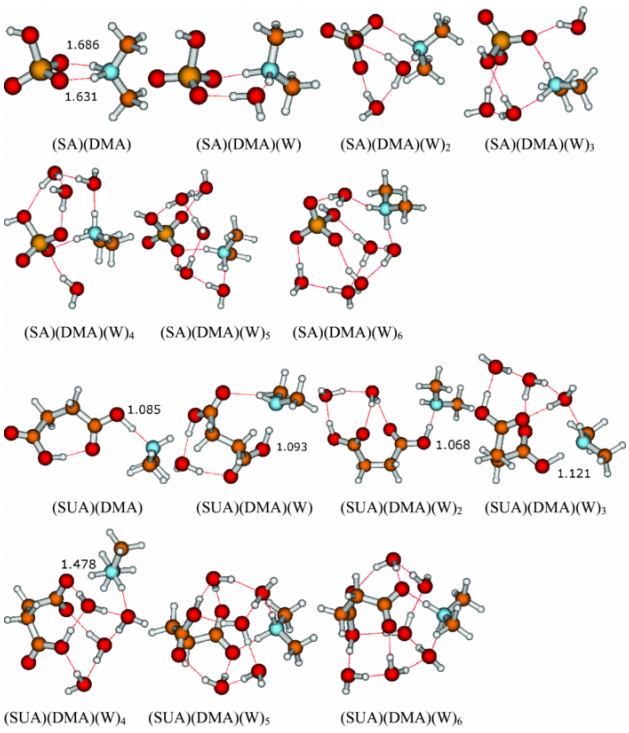

Figure 3.7. Optimized geometries of sulfuric/succinic acids and dimethylamine clusters in hydrate and anhydrate forms.

Four conformers of (SUA)(DMA)$(W)_5$ are depicted in Figure 3.8. The relative electronic energies relative to conformer IV are 6.24, 4.42, and 2.80 kcal mol^{-1} for conformers I, II, and III, respectively. To account for the contribution of Boltzmann averaging to the final Gibbs free energy, all the conformers of (SUA)(DMA)$(W)_5$ obtained at MM level are used in the averaging. The energies of (SUA)(DMA)$(W)_5$ conformers are listed in Table 3.4. At room temperature, the Boltzmann averaging contribution is calculated to be 0.79 kcal mol^{-1}. As a result, using the global minimum without Boltzmann averaging does not introduce a significant error in the final values of the free energy changes of reactions.

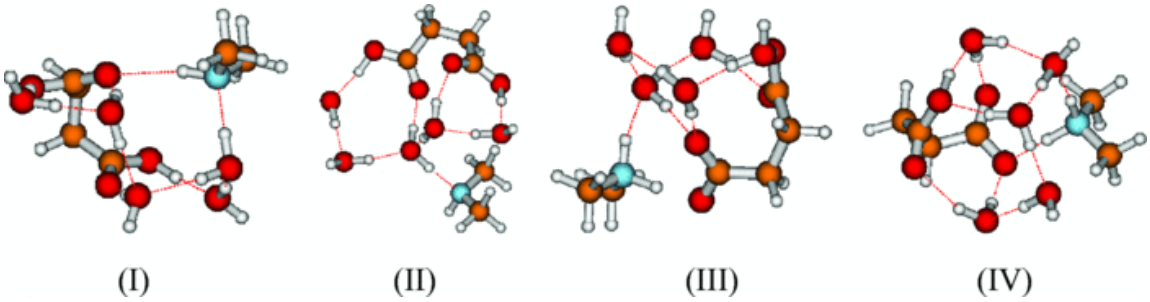

Figure 3.8. Optimized geometries of four conformers of (SUA)(DMA)$(W)_5$.

Table 3.4. Energies for (SUA)(DMA)$(W)_5$ conformers at MM level. The conformer 54 corresponds to the global minimum at MM level.

# conformer	MM (kcal mol^{-1})	# conformer	MM (kcal mol^{-1})	# conformer	MM (kcal mol^{-1})	# conformer	MM (kcal mol^{-1})
1	-129.20	21	-133.93	41	-137.54	61	-136.48
2	-129.21	22	-135.33	42	-134.45	62	-135.99
3	-130.29	23	-136.10	43	-135.54	63	-133.72
4	-134.32	24	-134.52	44	-134.78	64	-134.28
5	-135.87	25	-136.96	45	-136.25	65	-137.11
6	-135.78	26	-136.56	46	-137.49	66	-137.96
7	-136.34	27	-135.94	47	-137.35	67	-132.88
8	-136.54	28	-135.15	48	-137.38	68	-136.12
9	-136.35	29	-135.43	49	-137.65	69	-135.64
10	-134.86	30	-135.31	50	-137.17	70	-136.86
11	-134.98	31	-137.03	51	-137.62	71	-135.81
12	-135.58	32	-137.27	52	-137.52	72	-133.03
13	-136.49	33	-135.37	53	-133.98	73	-134.13
14	-135.95	34	-135.46	54	-138.58	74	-134.96

Table 3.4. Continued

# conformer	MM (kcal mol^{-1})	# conformer	MM (kcal mol^{-1})	# conformer	MM (kcal mol^{-1})	# conformer	MM (kcal mol^{-1})
15	-137.23	35	-133.66	55	-129.26	75	-133.34
16	-137.05	36	-136.13	56	-130.85	76	-134.24
17	-138.41	37	-135.01	57	-131.91	77	-135.28
18	-138.36	38	-136.41	58	-133.29	78	-136.66
19	-135.98	39	-136.97	59	-133.86	79	-136.72
20	-136.21	40	-134.51	60	-134.88		
Boltzmann Averaging (RT)				-137.793(-138.58)			

3.3.3 Thermochemical analysis

All thermal properties are calculated at the PW91PW91 level with a 6-311++G (2d, 2p) basis set at 1 atm and 298.15 K. The changes in Gibbs free energy of reaction of sulfuric acid with water and dimethylamine are summarized in Table 3.5. The results are also compared with those obtained previously.[31,32,40,163] The Gibbs free energy changes of sulfuric acid hydration in the present work are consistent with the previous reported results within 1-2 kcal mol^{-1}. The values of Gibbs free energy changes of sulfuric acid hydration by Loukonen *et al.*[32] and Kurten *et al.*[34] are more negative (1-2 kcal mol^{-1} smaller), when compared with that in our study and the study by Nadykto *et al.*[34] The values of Gibbs free energy changes by Temelso *et al.*[163] are generally higher (about 2 kcal mol^{-1}) than that reported in the present work and by Loukonen *et al.*[32] when the cluster size is large (the number of water is greater than 5). This can be explained since in the study by Temelso *et al.*[163] almost all the low-lying conformations of the sulfuric acid-water clusters were taken into consideration, when the Gibbs free energy of clusters were calculated through Boltzmann averaging. In contrast, the results reported in the present work and by Loukonen *et al.*[32] are obtained without Boltzmann averaging and only the cluster conformation with the lowest Gibbs free energy is included. The values of Gibbs free energy changes of complexation by sulfuric acid, dimethylamine, and water are also presented in Table

3.5. There is a large difference (5-10 kcal mol^{-1}) between the present work and Loukonen *et al.*,[32] but our present results agree well with those reported by Nadykto *et al.*[40] The disagreement between the results obtained with PW91PW91 level and RI-MP2 level has been previously noticed by Nadykto *et al.*[40] Since there exist still disagreements between the PW91PW91 and RI-MP2 results after the basis set extrapolation correction, the basis set superposition error cannot explain the difference, as discussed by Kurten *et al.*[34] Therefore, it remains unclear on the large difference between our present results and those by Loukonen *et al.*[32] The BSSE corrections of our current study are included in the Table 3.5. As shown in the table, BSSE correction almost scales linearly with the number of interacting entities. However, the applicability of BSSE in calculating total interaction energies may be questionable according to Kurten *et al.*[34]

Table 3.5. Comparison of the reaction free energy changes (kcal mol^{-1}) of sulfuric acid hydration and sulfuric acid-dimethylamine cluster hydration between the present results and those reported previously. The data in the parenthesis represent the calculated Basis Set Superposition Error (BSSE) in the same level.

Reactions	PW91PW91/6-311++G(2d,2p)	RI-MP2/aug-cc-pV(T+d)Z//BLYP/DZP[a]	Literature values
SA+W⇔(SA)(W)	-2.08 (0.89)	−2.93	–2.72[b], -2.28[c]
SA+2W⇔(SA)$(W)_2$	-4.04 (1.83)	−6.26	–3.91[b], -5.28[c]
SA+3W⇔(SA)$(W)_3$	-5.68 (3.42)	−7.11	–6.61[b]
SA+4W⇔(SA)$(W)_4$	-8.97 (4.73)	−8.11	–7.42[b]
SA+5W⇔(SA)$(W)_5$	-10.69 (5.22)	−10.01	–6.94[b]
SA+6W⇔(SA)$(W)_6$	-10.55 (6.33)		–6.17[b]
SA+DMA⇔(SA)(DMA)	-11.13 (1.14)	−15.57	-11.38[c],-13.66[d]
SA+DMA+W⇔(SA)(DMA)(W)	-14.03 (2.03)	−23.09	-15.05[c]
SA+DMA+2W⇔(SA)(DMA)$(W)_2$	-13.05 (3.14)	−23.05	-16.94[c]
SA+DMA+3W⇔(SA)(DMA)$(W)_3$	-14.57 (4.21)	−23.28	
SA+DMA+4W⇔(SA)(DMA)$(W)_4$	-13.50 (5.08)	−23.59	
SA+DMA+5W⇔(SA)(DMA)$(W)_5$	-15.94 (5.90)	−22.55	
SA+DMA+6W⇔(SA)(DMA)$(W)_6$	-17.09 (6.86)		

[a] Reference 32; [b] Reference 163; [c] Reference 40; [d] Reference 31.

The Gibbs free energy changes of formation of sulfuric and succinic acids hydrates with dimethylamine hydrates are summarized in Tables 3.6 and 3.7, respectively. Since both reactions in the tables have the form of two-molecular cluster interaction, the BSSE correction is similar to that (0.89 kcal mol^{-1}) of two interacting supermolecules. The present results are also compared with the available data reported by Nadykto *et al.*[40] For sulfuric acid with up to 2 molecules of water hydration, the largest difference between our results and those by Nadykto *et al.* is about 4 kcal mol^{-1}, i.e., for the $(SA)(DMA)(W)_2$ cluster the values are -14.85 kcal mol^{-1} in the present work and -19.02 kcal mol^{-1} by Nadykto *et al.*[40] For (SA)(DMA)(W) and (SA)(DMA)(W) clusters, the results from both studies are in good agreement (within 1 kcal mol^{-1}). The values of the free energy changes are plotted against the degree of hydration of acids and dimethylamine in two 3D contour plots (Figure 3.9). Figure 3.9 shows that the interaction between sulfuric and succinic acids with dimethylamine is strongly dependent on the degree of hydration of acids and dimethylamine. The Gibbs free energy of interaction of sulfuric acid with dimethylamine without water is -11.13 kcal mol^{-1}, while the Gibbs free energy of interaction of sulfuric acid with six-water hydrated dimethylamine is -18.59 kcal mol^{-1}, 7.46 kcal mol^{-1} larger than the anhydrated interaction. In contrast, the free energy of interaction of six-water hydrated sulfuric acid with dimethylamine is -8.89 kcal mol^{-1}, indicating that the hydration of sulfuric acid decreases its reactivity with dimethylamine, while the hydration of dimethylamine increases its reactivity with sulfuric acid. The maximum free energy of interaction for sulfuric acid and dimethylamine is reached, when sulfuric acid and dimethylamine are in anhydrated and hydrated forms, respectively. This conclusion, however, does not apply for the interaction of succinic acid with dimethylamine. For succinic acid with dimethylamine, the maximum Gibbs energy of interaction is achieved when both succinic acid and dimethylamine are hydrated. For instance, the Gibbs free energy of interaction of $(SUA)(W)_3$ with $(DMA)(W)_3$ is -7.41 kcal mol^{-1}, which is

more negative than that of SUA with $(DMA)(W)_6$ (-5.60 kcal mol^{-1}) and $(SUA)(W)_6$ with DMA (-1.63 kcal mol^{-1}). The difference of amine reactivity between hydrated sulfuric acid and succinic acid likely originates from a higher hydrophilic property of sulfuric acid than that of succinic acid.[46] The dimethylamminium carboxylate ion pair is stabilized by its surrounding hydration shell. Although the Gibbs free energies of interaction of sulfuric and succinic acids with dimethylamine exhibit a large span, the average interaction of succinic acid with dimethylamine is weaker than that of sulfuric acid. This is consistent with the conformational analysis, since proton transfer occurs readily (without hydration) for sulfuric acid-dimethylamine cluster, while for succinic acid-dimethylamine clusters proton transfer requires more than 3 water molecules for hydration.

Table 3.6. Energy changes associated with the reaction of sulfuric acid with dimethylamine in both hydrate and anhydrate forms. Energies are in kcal mol^{-1}. Geometries and harmonic frequencies are calculated at PW91PW91/6-311++G(2d,2p) level of theory.

Reactions	ΔE(ZPE)	ΔH(298.15)	ΔG(298.15)	Nadykto et al.[40] ΔG(298.15)
SA+DMA⇔(SA)(DMA)	-21.15	-21.10	-11.13	-11.38
SA+(DMA)(W)⇔(SA)(DMA)(W)	-26.64	-26.51	-15.55	-15.55
(SA)(W)+DMA⇔(SA)(DMA)(W)	-22.37	-22.31	-11.96	-12.76
$SA+(DMA)(W)_2$⇔$(SA)(DMA)(W)_2$	-26.41	-26.62	-14.85	-19.02
$(SA)(W)+(DMA)(W)⇔(SA)(DMA)(W)_2$	-23.73	-23.53	-12.49	-15.16
$(SA)(W)_2+DMA⇔(SA)(DMA)(W)_2$	-19.57	-19.33	-9.01	-11.65
$SA+(DMA)(W)_3⇔(SA)(DMA)(W)_3$	-26.29	-25.85	-14.82	
$(SA)(W)+(DMA)(W)_2⇔(SA)(DMA)(W)_3$	-26.03	-25.72	-14.29	
$(SA)(W)_2+(DMA)(W)⇔ (SA)(DMA)(W)_3$	-23.45	-22.63	-12.05	
$(SA)(W)_3+DMA⇔(SA)(DMA)(W)_3$	-18.12	-16.76	-8.89	
$SA+(DMA)(W)_4⇔(SA)(DMA)(W)_4$	-26.74	-26.18	-14.00	
$(SA)(W)+(DMA)(W)_3⇔(SA)(DMA)(W)_4$	-23.44	-22.98	-11.68	
$(SA)(W)_2+(DMA)(W)_2⇔(SA)(DMA)(W)_4$	-23.28	-22.85	-11.26	
$(SA)(W)_3+(DMA)(W) ⇔(SA)(DMA)(W)_4$	-19.54	-18.09	-9.33	
$(SA)(W)_4+DMA⇔(SA)(DMA)(W)_4$	-13.86	-12.38	-4.52	
$SA+(DMA)(W)_5⇔(SA)(DMA)(W)_5$	-30.22	-30.28	-17.40	
$(SA)(W)+(DMA)(W)_4⇔(SA)(DMA)(W)_5$	-28.30	-28.30	-14.37	
$(SA)(W)_2+(DMA)(W)_3⇔(SA)(DMA)(W)_5$	-25.10	-25.09	-12.16	
$(SA)(W)_3+(DMA)(W)_2⇔(SA)(DMA)(W)_5$	-23.78	-23.29	-12.06	
$(SA)(W)_4+(DMA)(W) ⇔(SA)(DMA)(W)_5$	-19.69	-18.69	-8.49	
$(SA)(W)_5+DMA⇔(SA)(DMA)(W)_5$	-16.86	-16.23	-5.26	
$SA+(DMA)(W)_6⇔(SA)(DMA)(W)_6$	-30.90	-30.78	-18.59	
$(SA)(W)+(DMA)(W)_5⇔(SA)(DMA)(W)_6$	-29.89	-30.06	-16.47	

Table 3.6. Continued

Reactions	ΔE(ZPE)	ΔH(298.15)	ΔG(298.15)	Nadykto et al.[40] ΔG(298.15)
$(SA)(W)_2+(DMA)(W)_4 \Leftrightarrow (SA)(DMA)(W)_6$	-28.07	-28.08	-13.56	
$(SA)(W)_3+(DMA)(W)_3 \Leftrightarrow (SA)(DMA)(W)_6$	-23.71	-23.20	-11.67	
$(SA)(W)_4+(DMA)(W)_2 \Leftrightarrow (SA)(DMA)(W)_6$	-22.04	-21.56	-9.92	
$(SA)(W)_5+(DMA)(W) \Leftrightarrow (SA)(DMA)(W)_6$	-20.80	-20.20	-7.93	
$(SA)(W)_6+DMA \Leftrightarrow (SA)(DMA)(W)_6$	-17.62	-16.80	-6.54	

Table 3.7. Energy changes associated with the reaction of succinic acid with dimethylamine in both hydrate and anhydrate forms. Energies are in kcal mol^{-1}. Geometries and frequencies are calculated at PW91PW91/6-311++G(2d,2p) level of theory.

Reactions	ΔE(ZPE)	ΔH(298.15)	ΔG(298.15)
$SUA+DMA \Leftrightarrow (SUA)(DMA)$	-13.97	-14.20	-2.45
$SUA+(DMA)(W) \Leftrightarrow (SUA)(DMA)(W)$	-13.09	-13.29	0.10
$(SA)(W)+DMA \Leftrightarrow (SUA)(DMA)(W)$	-11.75	-11.87	-0.12
$SUA+(DMA)(W)_2 \Leftrightarrow (SA)(DMA)(W)_2$	-17.63	-17.96	-4.64
$(SUA)(W)+(DMA)(W) \Leftrightarrow (SUA)(DMA)(W)_2$	-17.87	-17.65	-6.09
$(SUA)(W)_2+DMA \Leftrightarrow (SUA)(DMA)(W)_2$	-15.48	-15.28	-4.57
$SUA+(DMA)(W)_3 \Leftrightarrow (SUA)(DMA)(W)_3$	-18.35	-18.83	-4.27
$(SUA)(W)+(DMA)(W)_2 \Leftrightarrow (SUA)(DMA)(W)_3$	-21.02	-21.48	-7.55
$(SUA)(W)_2+(DMA)(W) \Leftrightarrow (SUA)(DMA)(W)_3$	-20.21	-20.21	-7.26
$(SUA)(W)_3+DMA \Leftrightarrow (SUA)(DMA)(W)_3$	-17.71	-17.68	-7.05
$SUA+(DMA)(W)_4 \Leftrightarrow (SUA)(DMA)(W)_4$	-18.75	-19.65	-2.11
$(SUA)(W)+(DMA)(W)_3 \Leftrightarrow (SUA)(DMA)(W)_4$	-18.38	-19.22	-3.60
$(SUA)(W)_2+(DMA)(W)_2 \Leftrightarrow (SUA)(DMA)(W)_4$	-19.99	-20.91	-5.14
$(SUA)(W)_3+(DMA)(W) \Leftrightarrow (SUA)(DMA)(W)_4$	-19.08	-19.49	-6.17
$(SUA)(W)_4+DMA \Leftrightarrow (SUA)(DMA)(W)_4$	-15.60	-16.40	-2.65
$SUA+(DMA)(W)_5 \Leftrightarrow (SUA)(DMA)(W)_5$	-23.89	-25.35	-6.43
$(SUA)(W)+(DMA)(W)_4 \Leftrightarrow (SUA)(DMA)(W)_5$	-24.90	-26.15	-7.21
$(SUA)(W)_2+(DMA)(W)_3 \Leftrightarrow (SUA)(DMA)(W)_5$	-23.47	-24.76	-6.96
$(SUA)(W)_3+(DMA)(W)_2 \Leftrightarrow (SUA)(DMA)(W)_5$	-24.98	-26.30	-9.82
$(SUA)(W)_4+(DMA)(W) \Leftrightarrow (SUA)(DMA)(W)_5$	-23.09	-24.32	-7.54
$(SUA)(W)_5+DMA \Leftrightarrow (SUA)(DMA)(W)_5$	-18.21	-18.96	-4.74
$SUA+(DMA)(W)_6 \Leftrightarrow (SUA)(DMA)(W)_6$	-19.65	-19.97	-7.67
$(SUA)(W)+(DMA)(W)_5 \Leftrightarrow (SUA)(DMA)(W)_6$	-21.57	-22.02	-9.37
$(SUA)(W)_2+(DMA)(W)_4 \Leftrightarrow (SUA)(DMA)(W)_6$	-21.52	-21.86	-8.40
$(SUA)(W)_3+(DMA)(W)_3 \Leftrightarrow (SUA)(DMA)(W)_6$	-19.99	-20.32	-9.47
$(SUA)(W)_4+(DMA)(W)_2 \Leftrightarrow (SUA)(DMA)(W)_6$	-20.52	-21.30	-9.02
$(SUA)(W)_5+(DMA)(W) \Leftrightarrow (SUA)(DMA)(W)_6$	-17.23	-17.04	-7.46
$(SUA)(W)_6+DMA \Leftrightarrow (SUA)(DMA)(W)_6$	-12.03	-11.68	-3.70

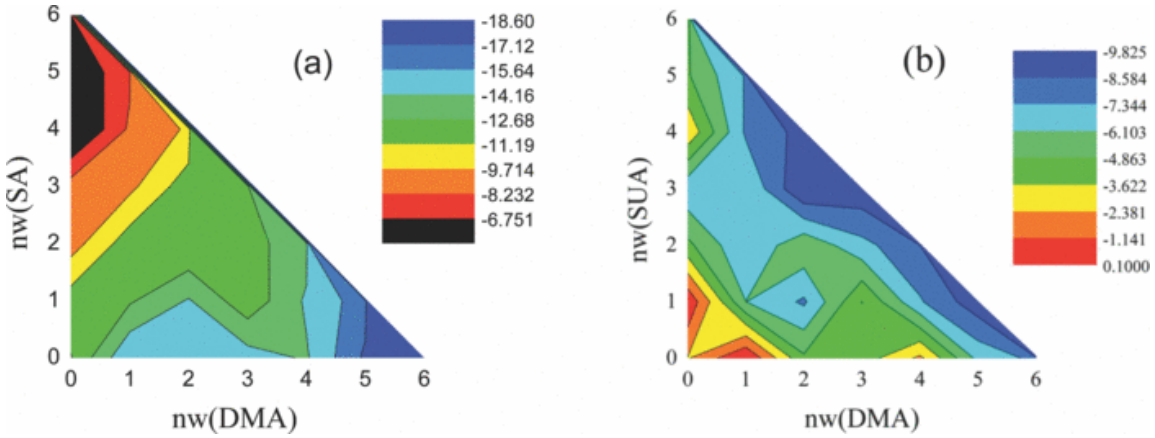

Figure 3.9. Contour plots of the free energies of reactions of sulfuric/succinic acid with dimethylamine hydrated clusters versus the number of water molecules in sulfuric/succinic acid and dimethylamine cluster.

The thermochemical analysis is subject to possible errors caused by applying simple harmonic oscillator approximation to anharmonic vibrations and internal rotations, which are more significant as the cluster size increases. Other possible source of errors may include the neglecting of many low-lying Gibbs free energy conformers of the molecular clusters. More accurate calculations perhaps require the Boltzmann averaging over all possible conformers. Our results show that the Gibbs free energies of interaction of dicarboxylic acids with amines in the presence of water are in the range from 0.10 to -9.93 kcal mol^{-1}. Compared with the free energy of interaction of dicarboxylic acids with sulfuric acid (-2.47 to -4.93 kcal mol^{-1}), dicarboxylic acids have stronger interaction with amines in the presence of hydration. Considering the ubiquity of dicarboxylic acids and amines in the atmosphere,[166] the interaction between dicarboxylic acids and amines can play an important role in the nucleation of nanoparticles.

3.4 Summary and conclusion

In this study, the hydrated succinic acid and dimethylamine clusters have been investigated to illustrate the interaction between dicarboxylic acids and amines. A two-step

calculation protocol has been developed. In the first step, the configuration space of molecular clusters is searched via the basin paving Monte Carlo (BPMC) method using the AMBER generalized force field and the force field parameter adapted from Loukonen *et al.*[32] The BPMC algorithm is validated using $(SA)(W)_2$ and $(SA)(W)_5$ clusters, by comparing with literature results. In the second step, the lowest energy conformers MM level are selected on the basis of the conformer structures obtained through BPMC sampling and higher level calculations are performed at PW91PW91/6-311++G(2d,2p) using the obtained structures of molecular cluster conformers. The clusters of sulfuric and succinic acids with dimethylamine containing hydration of up to 6 water molecules are studied. The results show that on the basis of the Gibbs free energy changes of reaction the hydration of sulfuric acid decreases its reactivity with dimethylamine from -11.13 to -6.54 kcal mol^{-1}, while the hydration of dimethylamine increases its reactivity with sulfuric acid from -11.13 to -18.59 kcal mol^{-1}. The decreasing reactivity of sulfuric acid after hydration is explained by pre-stabilization of sulfuric acid, while the increasing reactivity of sulfuric acid with hydrate dimethylamine is attributable to the stabilization of the product ions pair by water dipoles. The maximum Gibbs free energy change of the reaction is reached when the dimethylamine is hydrated with 6 molecules of water and sulfuric acid is anhydrated. For succinic acid, the maximum Gibbs free energy change of reaction is reached when both succinic acid and dimethylamine are hydrated by 3 molecules of water. The hydration of the succinic acid and dimethylamine increase the interaction free energy from -2.45 to -9.47 kcal mol^{-1}. Furthermore, hydration of dicarboxylic acids and dimethylamine cluster promotes the proton transfer from oxygen (dicarboxylic acid) to nitrogen (dimethylamine), suggesting the formation of stabilized dicarboxylate aminium ion pair. The results indicate that hydration plays an important role in the interaction of amines with sulfuric and dicarboxylic acids. The average interaction energy of succinic acids with dimethylamine

also indicates the dicarboxylic acids combine with amines in the atmosphere by forming aminium dicarboxylate ion pairs and contribute to nucleation of atmospheric nanoparticles.

Although sulfuric acid has been recognized as major nucleation species in the atmosphere,[51] it is well known that the atmospheric concentration of sulfuric acid alone is insufficient to explain the field observed nucleation rate and growth rate of nanoparticles.[82] Carboxylic acids, formed from photooxidation of anthropogenic and biogenic hydrocarbons,[102,103,167-170] have been suggested to participate in the aerosol nucleation process.[37,43] Because of its strong basicity, amines are also implicated to play an important role in formation and transformation of atmospheric aerosols.[31,32,40,46,97,171-173] Our present study shows there exists strong interactions between dicarboxylic acids and amines in hydrated clusters (-9.47 kcal mol^{-1}), suggesting that dicarboxylic acids and amines can participate in atmospheric aerosol nucleation by formation of aminium carboxylate ion pairs. It should be pointed that currently available theoretical methods may not guarantee that all the conformers of molecular clusters are surveyed in the configurational space. Our results suggest that the Boltzmann corrections unlikely change the conclusions of the strong interaction between hydrated clusters of dicarboxylic acids and amines. Future experimental studies are needed to study the synergetic effect of dicarboxylic acids and amines on the nucleation rate of the multi-component system consisting of sulfuric acid, dicarboxylic acids, amines, and water.

4. NUCLEATION ASSISTED BY DICARBOXYLIC ACIDS

4.1 Introduction

The formation and growth mechanisms of atmospheric aerosols have been the foci of atmospheric chemistry research during the past several decades, due to the importance of aerosols in affecting the Earth climate and human health.[51,57,59,81,171,174] Aerosols are known for affecting the Earth radiation budget in two ways, namely, directly reflecting or absorbing the incoming solar radiation and indirectly acting as cloud condensation nuclei (CCN) or ice nuclei (IN), which subsequently impact the development, lifetime, and albedo of clouds.[132,133] According to the IPCC report, the aerosol direct and indirect effects cause the largest uncertainties in the current model to predict the future climate.[57]

Atmospheric aerosols typically can be divided into two categories, i.e., primary and secondary, based on their origins in the atmosphere. Primary aerosols, such as soot and sea salts, are emitted directly into the atmosphere from various emission sources, while secondary aerosols, such as sulfate and nitrate aerosols, are formed in the gas-to-particle conversion processes. Although the mass concentration of primary aerosols is usually higher than that of secondary aerosols, the number concentration of secondary aerosols far exceeds that of the primary aerosols in the atmosphere due to the relatively small sizes, usually several nanometers, of secondary aerosols. The high number concentration and small size characteristics increase the importance of secondary aerosols, since it is easier for smaller aerosols particles to penetrate the human respiratory systems and harm human health.[175] It is well known that the gas-to-particle conversion process is composed of nucleation and growth stages, but the molecular level mechanism of the process still remains highly uncertain. The nucleation theorem has been

widely applied to interpret the experimental data and the connection between the exponent in equation (4.1) and number of molecules in critical nuclei has been established.[45,75,151]

$$J = J_0[C]^n \tag{4.1}$$

Where J is the nucleation rate, $[C]$ is the concentration of the nucleating species, and n is the number of nucleating molecules in the critical nuclei.

Sulfuric acid has been recognized as the major nucleating species in the atmosphere for a long time.[7,70,75,82,151,176] However, the value of exponent n for sulfuric acid concentration $[SA]$ is widely spread in the literature, ranging from 1 to 12, under a variety of nucleation conditions.[44,75,151] After a careful examination of the seemingly contradictory values of exponent n, it is indicated that the exponent value is sensitively dependent on the nucleation conditions. Many other species, such as organic acid, ammonia, and amines are known to affect the exponent n for sulfuric acid and enhance the nucleation rate to various extend. Numerous experimental studies have been carried out to measure the exponent.[44,71,75,83,151] All these experimental studies are devoted to measure the nucleation rate J and gaseous sulfuric concentration $[SA]$ simultaneously under various conditions of relative humidity (RH), temperature, and the concentrations of other gaseous species, including organic acids, ammonia, and amines. It is usually more convenient to rewrite equation (4.1) in logarithmic scale (Equation 4.2).

$$n = \frac{\partial \ln J}{\partial \ln[C]} \tag{4.2}$$

As a result of equation (4.2), the number of molecules of sulfuric acid in the critical nuclei is just the slope of lnJ versus $ln[SA]$.

The enhancement of the sulfuric acid and water binary nucleation by the addition of organic acids has been first proposed by Zhang and his coworkers in 2004 and widely tested

afterwards.[45,68] The organic acids studied in the 2004 work by Zhang *et al.* are all monocarboxylic acids, which can only bind to one sulfuric acid as suggested by theoretical studies.[47] Recently several studies have suggested that dicarboxylic acids might be more efficient in enhancing the nucleation rate of sulfuric acid and water binary system, considering the fact that dicarboxylic acids can bind to two sulfuric acid molecules and their saturation vapor pressure are usually much lower than the corresponding monocarboxylic acids with the same carbon number.[43,177,178]

In the current study, the sulfuric acid and water binary nucleation rate enhancement factor due to the addition of dicarboxylic acid is measured directly by monitoring the sulfuric acid ([*SA*]) or dicarboxylic acid ([*DCA*]) gaseous concentrations simultaneously with the nucleation rate. The sulfuric acid and dicarboxylic acid gaseous concentrations are measured via ion drift-chemical ionization mass spectrometry using $NO_3(HNO_3)^-$ and CO_3^-/CO_4^- reagent ions, respectively. The nucleation rate is obtained indirectly by dividing the measured total nanoparticle number concentration by the residence time of the nanoparticles in the flow tube. The newly nucleated nanoparticles are size magnified before entering the TSI UCPC3025A for counting by a home-built particle size magnifier (PSM), without which the nucleation rate might be underestimated.[75] The details of calibration of PSM and our experimental setup are given in the methods section.

4.2 Experimental methods

4.2.1 Construction and calibration of Particle Size Magnifier (PSM)

The detection of sub-3 nm particles has been achieved about a decade ago by using the particle size magnifier.[85,179] However, its application in laboratory nucleation studies only arises recently since it is believed that the size of critical nuclei in nucleation under atmospheric conditions is around 1.5 nm, which is below the size detection limit (3.0 nm) of the commercial

TSI 3025A ultrafine condensational particle counter.[69,75,83] In current studies, a home-build PSM was constructed based on the design described by Vanhanen *et al.* with several modifications.[86] The schematic diagram of the PSM is shown in Figure 4.1. The temperatures of the condenser (0 ^{o}C), saturator (80 ^{o}C), and inlet (16 ^{o}C) were controlled using a Honeywell thermal controller and thermoelectric cooling plate. The flow rates are 1.5, 0.7, 2.5, and 1.7 SLPM for the condenser, saturator, inlet, and liquid removal port, respectively. Diethylene glycol (DEG) was used as the working fluid in the saturator and the sizes of sub-3 nm particles were increase because of the condensing of super saturated vapor of DEG in the mixing zone and the condenser.

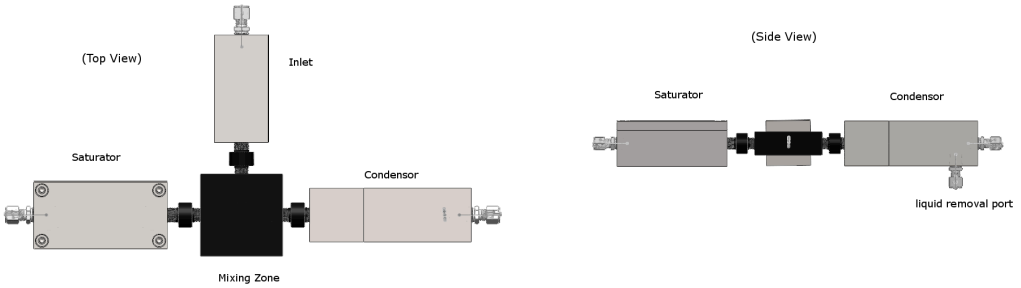

Figure 4.1. Schematic diagram of the home-built particle size magnifier (PSM) (a) Top view, (b) Side view.

To calibrate the performance of our PSM, an electrospray aerosol generator (ESAG) and aerosol electrometer (AEM) were constructed. The electrospray aerosol generator was made based on the design by Ude *et al.* with several modifications.[180] The schematic calibration setup

for PSM is shown in Figure 4.2. Briefly, the polydispersed tetrapropylammonium iodine (TPAI) nanoparticles were generated by electrospray aerosol generator and then size selected by a TSI nano differential mobility analyzer (n-DMA). The monodispersed nanoparticles flow was splitted into two, with one passing to AEM and the other to PSM. The basic component of AEM is a Faraday cup which captures the charged nanoparticles and produces electrical current. The current under our experimental conditions is on order of pico or sub-pico Ampere and the preamplifier was used to convert the pico or sub-pico electrical signal to voltage signal. The noise in the voltage signal was significantly reduced through an electrical filter and numerical averaging. The measured current can be used to calculate the absolute number concentration of charge nanoparticles (n_1) when the flow rate was given. The nanoparticle number concentration (n_2) was also measured by TSI UCPC 3025A after size magnification by PSM. The detection efficiency of PSM/UCPC was determined by taking the ratio of n_2 to n_1.

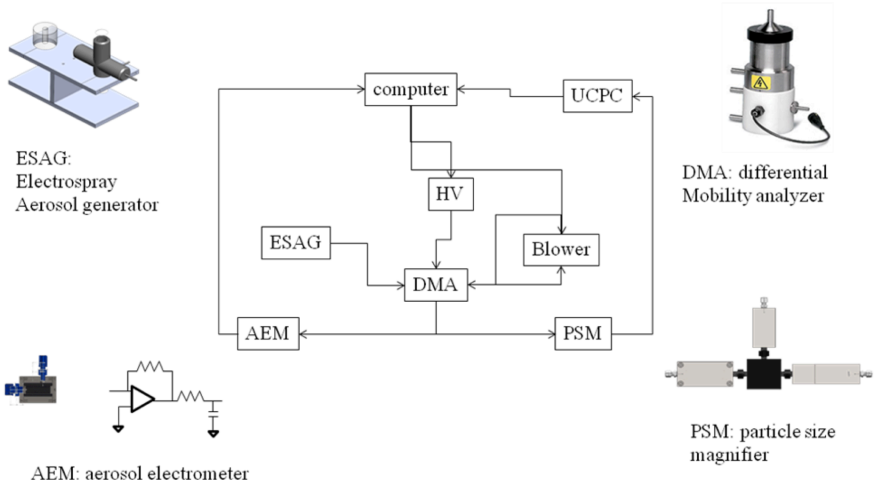

Figure 4.2. Schematic diagram of experimental setup for calibration of PSM.

4.2.2 Nucleation rate and gas concentration measurement

The nucleation experimental setup is shown in Figure 4.3. During the nucleation experiment, the concentrations of gaseous species, such as sulfuric acid and succinic acid a proxy for dicarboxylic acids, were measured online using ion drift chemical ionization mass spectrometer (ID-CIMS). Simultaneously, the nanoparticle concentration was measured at downstream of the flow tube by UCPC 3025A after size magnification by PSM. Sulfuric acid and succinic acid vapors were generated by passing dry nitrogen flow through a heated reservoir of sulfuric acid and succinic acid, respectively. The two vapor flows were then mixed with a humidified flow and pure dry nitrogen flow in the mixing zone which was kept at 110 ^{o}C during the experiment. The mass spectrometer pin hole was located in the mixing zone and the high temperature in the mixing zone prevented formation of nanoparticles, which might cause under estimation of the gaseous species concentration. After the mixing zone, nucleation started in a flow tube coated with circulating methanol flow which was maintained at 10 ^{o}C. Reagent ions $NO_3(HNO_3)^-$ and CO_3^-/CO_4^- were generated via ionization of the dry nitrogen flow doped with nitric acid and the oxygen flow doped with carbon dioxide using corona discharge, respectively. Initially the temperature of sulfuric acid and succinic acid reservoirs was kept at 25 ^{o}C and the RH is fixed. During the experiment, the temperature of either sulfuric acid reservoir or succinic acid reservoir was changed, while the rest of the conditions were kept constant.

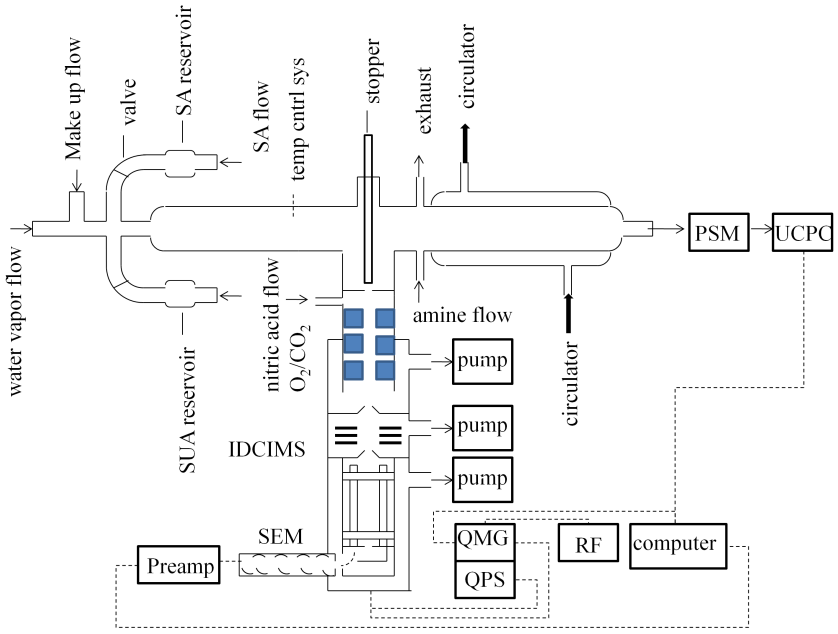

Figure 4.3. Schematic experimental setup for nucleation measurements.

4.3 Results and discussion

4.3.1 Calibration result of PSM using mobility standard

The mobility size spectrum of electrospray generated TPAI nanoparticles is shown in Figure 4.4. The peak size of the spectrum is about 1.23 nm, which is close to 1.16 nm measured by Ude *et al.*[180] However, our spectrum does not show fine structures as revealed by Ude *et al*, which is caused by either the broad transfer function or low resolution DMA used in the current study. The measured mobility size spectrum is the convolution of the actual spectrum and the transfer function of DMA. The mobility size spectrum from UCPC measurement is shown in Figure 4.5. The spectra with PSM on and off are compared with each other and it is shown that at least 1/3 of the 1.5 nm size TPAI nanoparticles are size magnified by PSM. Without PSM, 1.5

nm size TPAI nanoparticles can be barely detected by UCPC. Taking the diffusion loss of nanoparticles in the tubing into consideration, the detection efficiency of PSM-UCPC system at 1.5 nm particle size is around 50%.

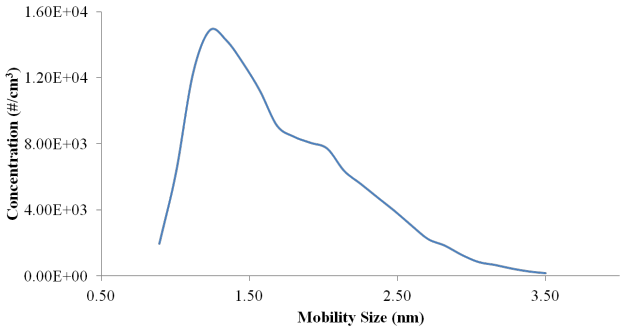

Figure 4.4. Mobility size spectrum of nanoparticles generated by electrospray of tetrapropylammonium iodine (TPAI) water solution.

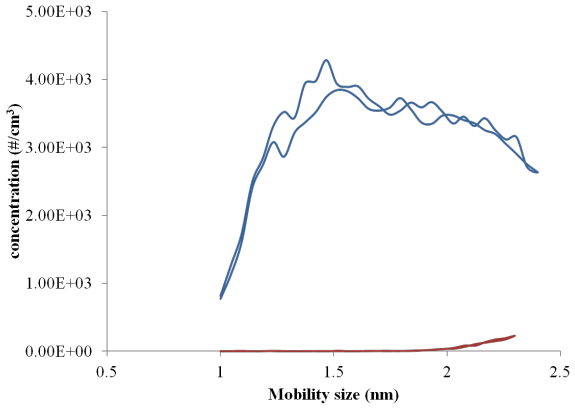

Figure 4.5. Mobility size spectrum of electrospray generated nanoparticles detected by ultrafine condensational particle counter (TSI, UCPC3025A) with (blue line) and without (red line) particle size magnifier (PSM).

4.3.2 Binary nucleation of sulfuric acid and water with addition of dicarboxylic acid

The typical reagent ion spectra of $NO_3(HNO_3)^-$ and CO_3^-/CO_4^- are presented in Figure 4.6(a) and 4.6(b), respectively. The reagent ions react with H_2SO_4 and carboxylic acid via the following equations,

$$NO_3^-\bullet(HNO_3)_n+H_2SO_4 \rightarrow HSO_4^-\bullet(HNO_3)_n+HNO_3 \quad (R1)$$

$$RCOOH+CO_4^- \rightarrow RCOOH\bullet O_2^-+CO_2 \quad (R2)$$

$$RCOOH+CO_4^- \rightarrow RCOO^-+HCO_4 \quad (R3)$$

where R denotes alkyl functional group. In the case for succinic acid, ions are detected at *m/e*=89, 117 ($RCOO^-$). The $RCOOH\bullet O_2^-$ ion at *m/e*=150 is not observed for succinic acid while $RCOOH\bullet O_2^-$ form of ions were observed for other carboxylic acid, such as cis-pinonic acid before.[45] The mass difference between *m/e*=89 and 117 is 28, which might be caused by a neutral loss of one CO group. The mechanism of neutral loss of one CO in succinic acid CIMS spectra is still unclear.

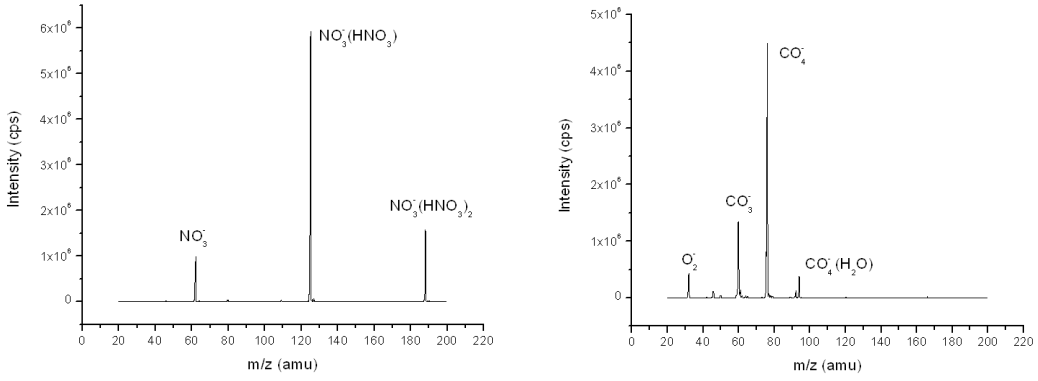

Figure 4.6. Reagent ion spectra of (a) CO_3^-/CO_4^- and (b) $[NO_3(HNO_3)]^-$ for detecting of succinic and sulfuric acids, respectively.

The concentration of the sulfuric acid and succinic acid can be calculated based on the equation of CIMS,

$$[A^{+/-}]=[R^{+/-}][A]k_p t_p \quad (4.3)$$

where $[A^{+/-}]$, $[R^{+/-}]$, and $[A]$ are the concentrations of product ion, reagent ion, and neutral analyte. The ion-molecule reaction constant is k_p and the travel time of reagent ion in the drift tube is t_p. For H_2SO_4, the ion-molecule reaction rate with $NO_3(HNO_3)^-$ is 1.86×10^{-9} cm^3 s^{-1}, which is the same for succinic acid ion-molecule reaction with CO_4^-. The travel times of reagent ions $NO_3(HNO_3)^-$ and CO_4^- in the drift tube in our experimental setup are about 2.03 and 1.53 ms, respectively. The *E/N* ratio, where *E* is the electric field strength and *N* is the number concentration of buffer gases in the drift tube, under our typical experimental conditions for negative reagent ions is about 10 Td (1Td=10^{17} V cm^2 $molecule^{-1}$), which is much lower than the *E/N* for positive reagent ions, such as hydronium (140 Td).[181,182] The concentration of analyte [*A*], therefore, can be determined from equation 4.3 without the necessity of calibration.

The temporal profile of sulfuric acid and nucleated nanoparticle concentrations are shown in Figure 4.7(a) when the succinic acid concentration and RH are both fixed. It is clearly shown that the nucleated nanoparticle concentration rises rapidly as the sulfuric signal increases. Figure 4.7(b) shows the temporal profile of succinic acid and nucleated nanoparticle concentrations as the sulfuric acid concentration and RH are both fixed. Unlike in the sulfuric acid case, nucleated nanoparticle concentration does not change rapidly with increasing succinic acid concentration. The nucleated nanoparticle concentration increases by 6 times from about 500 cm^{-3} to 3000 cm^{-3}, as the succinic acid concentration increases from about 0 ppt to 580 ppt. Figure 4.7(c) shows the nucleated nanoparticle number concentration as a function of succinic acid concentration at three different RHs, including 5%, 11%, and 19%. It is shown that as RH increases, the nucleated nanoparticle concentration increases. For 696, 493, and 349 ppt succinic

acid, the nucleated nanoparticle concentration increases from 21 cm^{-3} to 210 cm^{-3}, 9000 cm^{-3} to 20300 cm^{-3}, and 30600 cm^{-3} to 62200 cm^{-3} at 5%, 11%, and 19% RHs, respectively.

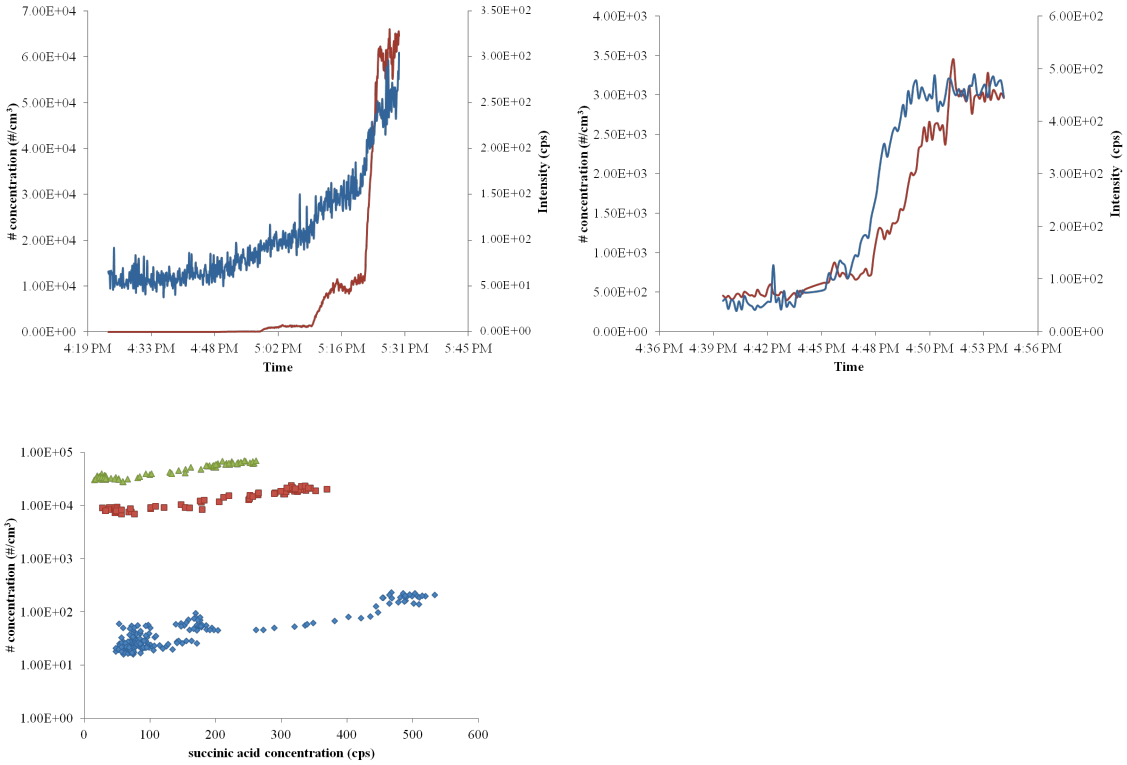

Figure 4.7. Temporal profile of nanoparticle and (a) sulfuric or (b) succinic acids concentrations; (c) the dependence of nanoparticle concentration on succinic acid concentration at fixed sulfuric acid concentration and RH of 5% (blue), 11% (red) and 19% (green).

According to classical nucleation theorem[10], the total nucleation rate of sulfuric acid (SA) – water system with the addition of succinic acid (SUA) can be written in the following form,

$$J = J_{s-w} + J_{org} \tag{4.4}$$

$$J_{s-w} = J_1[SA]^{n1}[RH]^{n2} \quad (4.4a)$$

$$J_{org} = J_2[SA]^{n3}[RH]^{n4}[SUA]^{n5} \quad (4.4b)$$

The nucleation rate can be calculated approximately through dividing the total nucleated nanoparticle concentration by the nucleation time in the flow tube. Since the nucleation rate and the gaseous concentrations of sulfuric acid and succinic acid are directly proportional to the nucleated nanoparticle concentration and product ion signal intensity, respectively, the nanoparticle concentration and product ion signal intensities are used directly in the double logarithmic plot. Figure 4.8(a), (b), and (c) show the nucleation rate dependence on the sulfuric acid, succinic acid concentrations, and RH, respectively, in double logarithmic scale. The slopes of the linear fit in the three plots are about 6.42, 1.19, and 5.61, respectively, indicating the critical nuclei contains 6 molecules of sulfuric acid, 1 molecule of succinic acid, and 5 molecules of water.[81] The results are different from that obtained in some previous laboratory nucleation measurements involving amines, which had a slope close to 1.0 for sulfuric acid.[83,151] Several theoretical calculations and chemical intuition have shown that the interaction of sulfuric acid with amines is stronger than that with ammonia or water.[31,32,40] As a result, it is expected that the slope of sulfuric acid in the double logarithmic plot decreases to about 1.0 with the addition of amines. In our current experiment, there are no amines and therefore, our current results are not in contradiction to the previous result in which amines are involved.

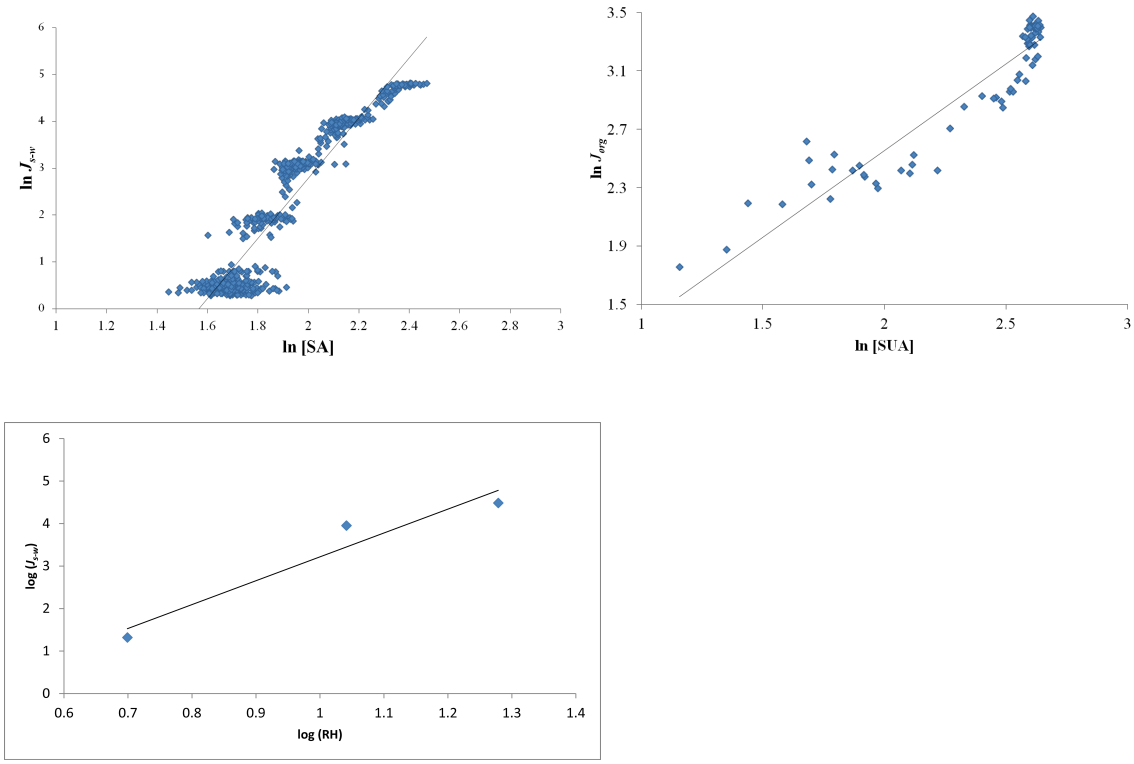

Figure 4.8. Power dependence of nucleation rate on (a) sulfuric and (b) succinic acid concentrations, and (c) RH.

4.4 Summary and conclusion

In this study, the enhancing effect of succinic acid, a proxy for dicarboxylic acids, in binary nucleation by sulfuric acid and water are investigated. The gaseous concentrations of sulfuric and succinic acids are monitored by ion drift chemical ionization mass spectrometry using $NO_3(HNO_3)^-$ and CO_3^-/CO_4^- reagent ions, respectively. The nucleated nanoparticle concentration is monitored simultaneously downstream of the nucleation tube using UCPC 3025A. Since the size detection limit of the UCPC 3025A is about 3.0 nm, the nanoparticle concentration will be underestimated if measured directly. As a result, the particle size magnifier is employed to push down the limit to about 1.5 nm. The performance of particle size magnifier

is calibrated by comparing the measured nanoparticle concentrations from two detection methods, Faraday cup measurement and PSM-UCPC measurement. The electrospray generated TPAI nanoparticles has a mobility spectrum peaked at about 1.5 nm and these nanoparticles are used in the calibration of PSM. A detection efficiency of 33% is obtained for 1.5 nm TPAI nanoparticles without the correction of diffusion loss of nanoparticles in the metal tubing. The double logarithmic plots of the nucleation experimental results show that the critical nuclei under our experimental conditions contain 6, 1, and 5 molecules of sulfuric acid, succinic acid, and water, respectively.

Although sulfuric acid has been recognized as the major contributor to the atmospheric nucleation, it is well known that binary nucleation of sulfuric acid and water alone is insufficient to explain the field observed nucleation rate.[51,82] Dicarboxylic acids, formed from photooxidation of volatile organic compounds (VOCs), have been previously suggested to participate in the nucleation process theoretically.[37,43] Although the enhancing effect of dicarboxylic acids to binary nucleation of sulfuric acid and water is not comparable to that of amines, the atmospheric concentration of total dicarboxylic acids are much higher than that of amines. Besides, the enhancing effect of amines is limited by the availability of non-neutralized sulfuric acid. Therefore, after taking the total concentration into consideration, both dicarboxylic acids and amines might be important in enhancing atmospheric nucleation rate. In addition, the interaction between dicarboxylic acids and amines might also contribute to atmospheric nucleation. Further experimental studies on nucleation involving both the dicarboxylic acids and amines are needed.

5. GROWTH OF FRESHLY NUCLEATED NANOPARTICLE BY EPOXIDE

5.1 Introduction

Atmospheric aerosols are ubiquitous and have consequential effects in many aspects, such as altering the radiation balance of the Earth's atmosphere, impairing visibility, modifying the microphysical properties of clouds, and affecting human health.[183] Currently, the direct and indirect forcings of aerosols represent the largest uncertainty in the projections of future climate. As a key component of atmospheric particulate matter, nanoparticles are frequently formed through gas-to-particle conversion under diverse environmental conditions, including urban, coastal, and forested areas. New particle formation in the atmosphere undergoes two consecutive steps, i.e., nucleation to form critical nuclei and growth of freshly nucleated particles to a larger size. The rate of the nucleation process is limited by a free energy barrier, which needs to be surmounted before growth becomes spontaneous. In addition, growth of nanoparticles is also restricted by the Kelvin (curvature) barrier, because of significantly elevated equilibrium vapor pressures. Several inorganic and organic species have been identified for their participations in the nucleation stage of new particle formation,[81], including sulfuric acid, ammonia, amines, and organic acids.[45,46,64] On the other hand, the growth stage of newly formed nanoparticles is less understood, because of the lack of knowledge in the chemical identities and mechanisms responsible for overcoming the Kelvin barrier to contribute to nanoparticle growth.

Currently, only a few species have been identified to enhance atmospheric nanoparticle growth. For example, previous experimental studies have demonstrated that glyoxal and 2-4 hexadienal enhance particle growth at 10 nm and larger sizes, but contribute negligibly to particle growth at the size smaller than 4 nm.[97,98] On the other hand, amines are shown to

contribute to nanoparticle growth down to the size of 4 nm. For glyoxal, amines, and 2,4-hexandienal, the experimentally measured growth factors (defined by the ratio of the particle diameters measured after and before organic vapor exposure) are dependent on relative humidity (RH) and particle size. The growth factor increases with increasing RH in the cases of glyoxal and amines, but decreases with RH in the case of 2,4-hexandienal. The distinct growth patterns of the different organic species on RH have been explained by different reaction mechanisms. Glyoxal reacts on nanoparticles via hydration and oligomerization that are dependent of water activity, while 2,4-hexandienal reacts via protonation and enolization followed by aldol condensation, which are acid-catalyzed. On the other hand, amines undergo the acid-base reactions, forming aminium sulfate, which might be hygroscopic.[97,173] The oligomerization and polymerization reactions of glyoxal and 2-4 hexadienal are of the second or higher order, but the acid–base reaction is of the first order, likely accounting for the distinct size dependences of the measured growth factors for glyoxal, amines, and 2,4-hexandienal.

Recently, epoxides have been identified as another key species to contribute to the growth of atmospheric particles.[184-186] The possible formation pathways of epoxides from isoprene in the atmosphere were suggested by Paulot *et al.*[187] Iinuma *et al.* carried out environmental chamber studies on the growth of 40-45 nm acidic (H_2SO_4/$(NH_4)_2SO_4$) and neutral (Na_2SO_4) particles exposed monoterpene oxide vapors.[184] Surratt *et al.* and Lin *et al.* investigated the growth of larger particles by isoprene epoxide (IEPOX) in an environmental chamber,[185,186] showing that particle growth was only observed on acidic particles by an acid catalyzed reaction mechanism involving organosulfate formation. In addition, the kinetics and products of hydrolysis and esterification of epoxides in the bulk phase have been studied.[184,188-191] Elrod *et al.* applied the ^{1}HNMR method to investigate the kinetics of hydrolysis and esterification of several epoxides using bulk samples, including non-atmospherically relevant

epoxides[188] and laboratory synthesized atmospherically relevant epoxides.[189] Their results indicate that the hydrolysis and esterification reactions of epoxides are of the second order in total and but of the first order with respect to the acid concentration. The hydrolysis and esterification products of epoxides in their study are identified as diols and organosulfates, respectively. Darer *et al.* found higher stabilities of organosulfate than organonitrate formed from isoprene derived epoxides, which likely explain the larger abundance of organosulfate than that of oganonitrate observed in ambient secondary organic aerosols.[190] Recently, Lal *et al.* employed an ion drift – chemical ionization mass spectrometry (ID-CIMS) flow tube technique and obtained the uptake coefficients (γ) on order of 10^{-2} for two model epoxides, isoprene oxide and α-pinene oxide, on concentrated (about 90 wt %) sulfuric acid solution surfaces. Their bulk ^{1}HNMR studies showed that the main products from the reactions of isoprene oxide and α-pinene oxide with sulfuric acid solutions are diols and organosulfates (for α-pinene)/acetals (for isoprene oxide) at low and high acidities, respectively.[191] The uptake of isoprene oxide, butadiene epoxide, and butadiene diepoxide on less concentrated sulfuric acid solution (0-30 wt %) surfaces was studied by Wang *et al.*[192], with the uptake coefficients (on the order of 10^{-4}) generally smaller than those reported by Lal *et al.* The most recent study by Bleier *et al.*[193] showed that α-pinene oxide reacts with aqueous aerosols quickly even under low acidic conditions and some of the products partition back into the gas phase. In the later study, no long-lived organosulfates nor products that retain the bicyclic carbon backbone were observed.[193]

In the present study we investigate the growth of sulfuric acid - water nanoparticles from heterogeneous reactions of epoxides. The size growth factors of 4-20 nm nanoparticles exposed to three model epoxides (isoprene oxide, α-pinene oxide, and butadiene diepoxides) and at various RH and reactant concentrations are measured using a nano-tandem differential mobility analyzer (n-TDMA). Chemical compositions of the 20 nm sulfuric acid - water nanoparticles

after epoxide exposure are analyzed by using a thermo desorption ion drift chemical ionization mass spectrometer (TD-ID-CIMS).[181,194] The details of n-TDMA and TD-ID-CIMS techniques are presented in the experimental section.

5.2 Results and discussion

The measured growth factors for 20 nm nanoparticles for isoprene oxide, *α*-pinene oxide, and butadiene diepoxides at 4% and 30% RHs are summarized in Table 5.1. As RH increases from 4% to 30%, the growth factors decrease from 1.15, 1.31, and 1.91 to 1.02, 1.02, and 1.50 for butadiene diepoxides, *α*-pinene oxide, and isoprene oxide, respectively. Figure 5.1 displays the growth factors for isoprene oxide at various particle mobility sizes and RHs. The decrease in the growth factor with increasing RH is likely attributable to decreasing (increasing) organosulfate (alcohols) production at lower acidity or higher water activity. It has been demonstrated previously by that alcohols contribute negligibly to nanoparticle growth.[98] At 30% RH and 298K, organosulfate formation from methanol takes about 96 h,[195] which is much longer than the exposure time scale (ca. 3 s) in our experiment.

Table 5.1. Growth factors of 20 nm sulfuric acid nanoparticle in epoxide vapors at various RHs. (The numbers in the parenthesis are the 2σ standard deviations.)

Epoxides	Butadiene diepoxide		*α*-pinene oxide		Isoprene oxide	
RH (%)	4	30	4	30	4	30
Growth factor	1.150(0.050)	1.020(0.020)	1.310(0.020)	1.020(0.010)	1.912(0.010)	1.500(0.090)

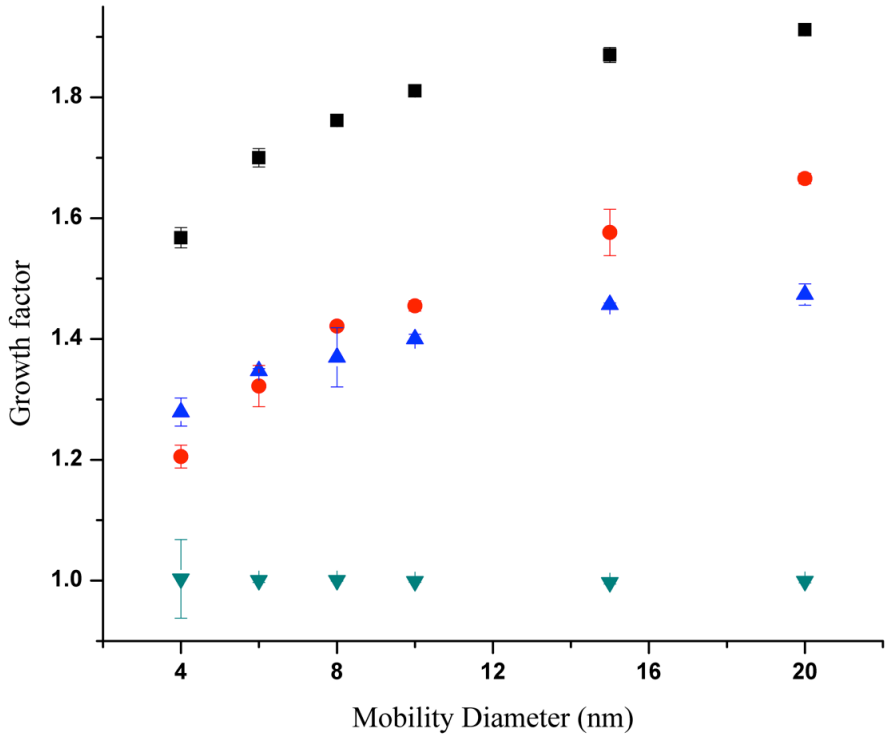

Figure 5.1. Growth factors of sulfuric acid nanoparticles of various sizes in isoprene oxide vapor (23.75 ppm) at 4%, 25%, 43%, and 68% RHs (black square for 4%, red dot for 25%, blue triangle for 43%, and dark cyan for 68%).

Figure 5.2 displays the growth factors of isoprene oxide at various particle mobility sizes and isoprene oxide concentrations. At a fixed concentration of 23.75 ppm, the growth factor increases monototically from 1.23, 1.28, 1.33, 1.36, 1.42, to 1.44 as the size increases from 4, 6, 8, 10, 15, to 20 nm, respectively. A significant notable growth factor is measured even at 4 nm (1.23). The increasing trend of the growth factor with size is explained by the Kelvin effect, since the equilibrium vapor pressure is significantly elevated on nanoparticles. Figure 5.3 also

shows an increase in the growth factors from 1.004, 1.119, 1.269, to 1.437 as the concentration for isoprene oxide increases from 0.24, 1.70, 7.00, to 23.75 ppm. Figure 5.4 shows the size dependent growth rate (nm/h/ppb) and accommodation coefficients (α_r) (see the supporting information for details). The accommodation coefficient for the planar surface (α_∞) and characteristic length for Kelvin effect (d_σ)[196] are obtained by nonlinear curve fitting, and these values are summarized in Table 5.2. The uptake coefficient of isoprene oxide on the planar sulfuric acid surface at 43% RH is estimated to be 1.24 x 10^{-3}, which is comparable to the values of 1 x 10^{-5} to 3 x 10^{-3} for 3 to 20 wt % H_2SO_4 solutions reported by Wang *et al.*,.[192] but smaller than the value of 1.7 x 10^{-2} reported by Lal *et al.* on concentrated sulfuric acid (90 wt H_2SO_4 %) surfaces.[191] Considering possibility of volatile products which may evaporate from nanoparticles, the uptake coefficient in the present study likely corresponds to a lower bound, compared to those previously measured on bulk solutions.[191]

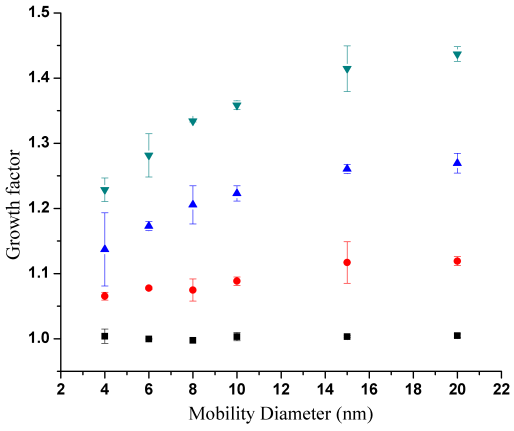

Figure 5.2. Growth factor of sulfuric acid nanoparticle in isoprene oxide vapor of various concentrations at 43% RH (dark cyan triangle for 23.75 ppm isoprene vapor, blue triangle for 7.00 ppm, red dot for 1.70 ppm, and black square for 0.24 ppm).

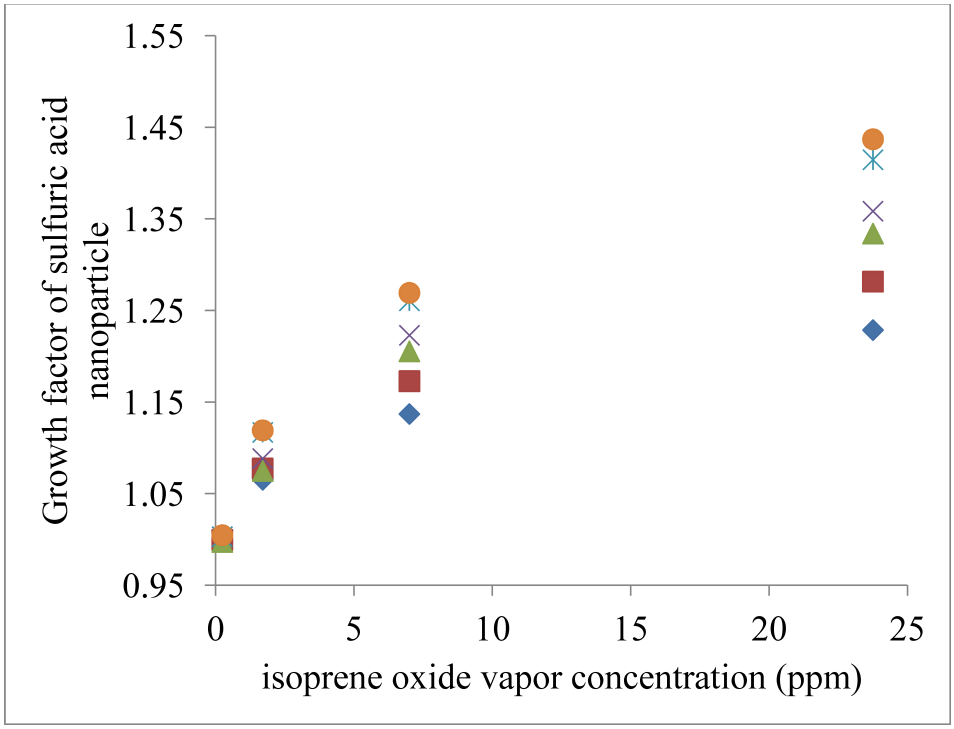

Figure 5.3. Growth factors versus the isoprene oxide concentrations at 43% RH for different sizes (From bottom to top are 4, 6, 8, 10, 15, and 20 nm particles)

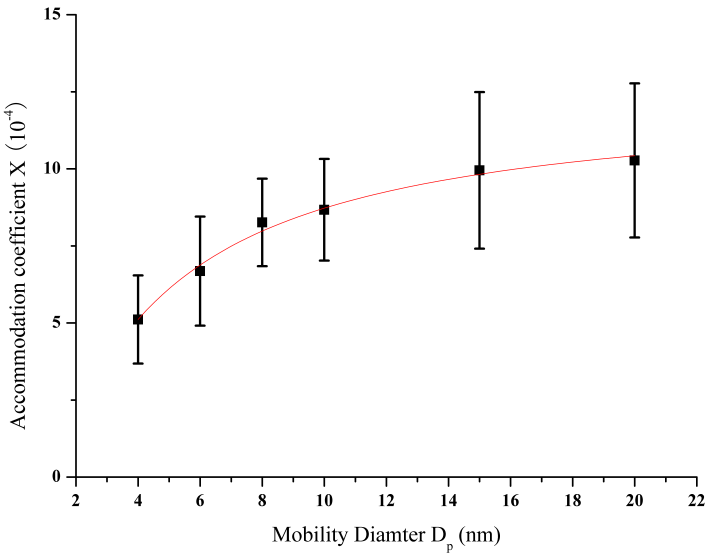

Figure 5.4. Size-dependent accommodation coefficients and fitted line using Kelvin effect equation.

Table 5.2. Size-dependent growth rates and accommodation coefficients α for isoprene oxide on sulfuric acid nanoparticle surface at 43% RH. Fitted parameters α_∞ (accommodation coefficient at planar surface) and d_σ (characteristic diameter for Kelvin effect) are also presented.

Size	4 nm	6 nm	8 nm	10 nm	15 nm	20 nm
Growth rate (nm/ppb/hour)	0.09(0.02)	0.17(0.05)	0.28(0.05)	0.37(0.07)	0.63(0.16)	0.87 (0.21)
Accommodation coefficient α ($\times 10^{-4}$)	5.11 (1.43)	6.68(1.77)	8.26 (1.42)	8.67(1.65)	9.95 (2.54)	10.27 (2.50)
Fitted parameters						
α_∞ ($\times 10^{-4}$)	12.46 (0.26)					
d_σ (nm)	3.56 (0.18)					

Figures 5.5, 5.6, and 5.7(b-c) depict the TD-ID-CIMS spectra of nanoparticles collected on a platinum filament after the exposure to isoprene oxide, *α*-pinene oxide, and butadiene diepoxides vapors, respectively. The major peaks in the mass spectra and their assignments are summarized in Table 5.3. The schematic reaction mechanisms for isoprene oxide, *α*-pinene oxide, and butadiene diepoxides are presented in Figure 5.5, 5.6, and 5.7(a), respectively. Organosulfates are not detected in the mass spectra for isoprene oxide, consistent with the results by Lal *et al.*[191] and explaining the differences in the behaviors of the growth factors among isoprene oxide, *α*-pinene oxide, and butadiene diepoxides at high RHs. At 30% RH, the growth factor for isoprene oxide is 1.500, which is much larger than 1.020 for *α*-pinene oxide and butadiene diepoxides. For *α*-pinene oxide and butadiene diepoxides, the reaction products that lead to nanoparticle growth are organosulfates, while for isoprene oxide, the product is isoprene oxide derived polymers, which are inferred from the peak assignments in Table 5.3. The reaction mechanism leading to the polymer formation from isoprene oxide is illustrated in Figure 5.5(a). The *α,β*-unsaturated ketone formed through 1,2-methanide shift polymerizes via the Michael addition in the presence of sulfuric acid,[197] and the resulting polymers are detected by the TD-ID-CIMS at *m/z* of 169, 253, 337, and 421 for dimer, trimer, tetramer, and pentamer, respectively. Organosulfates are not identified since polymerization consumes the reactants. The reaction mechanisms for *α*-pinene oxide (Figure 5.6(a)) and butadiene diepoxides (Figure 5.5(a)) are similar. Because of the absence of the double bond in *α*-pinene oxide and butadiene diepoxides, the *α,β*-unsaturated ketone formation from both species is implausible, and only organosulfates and dimer are detected .

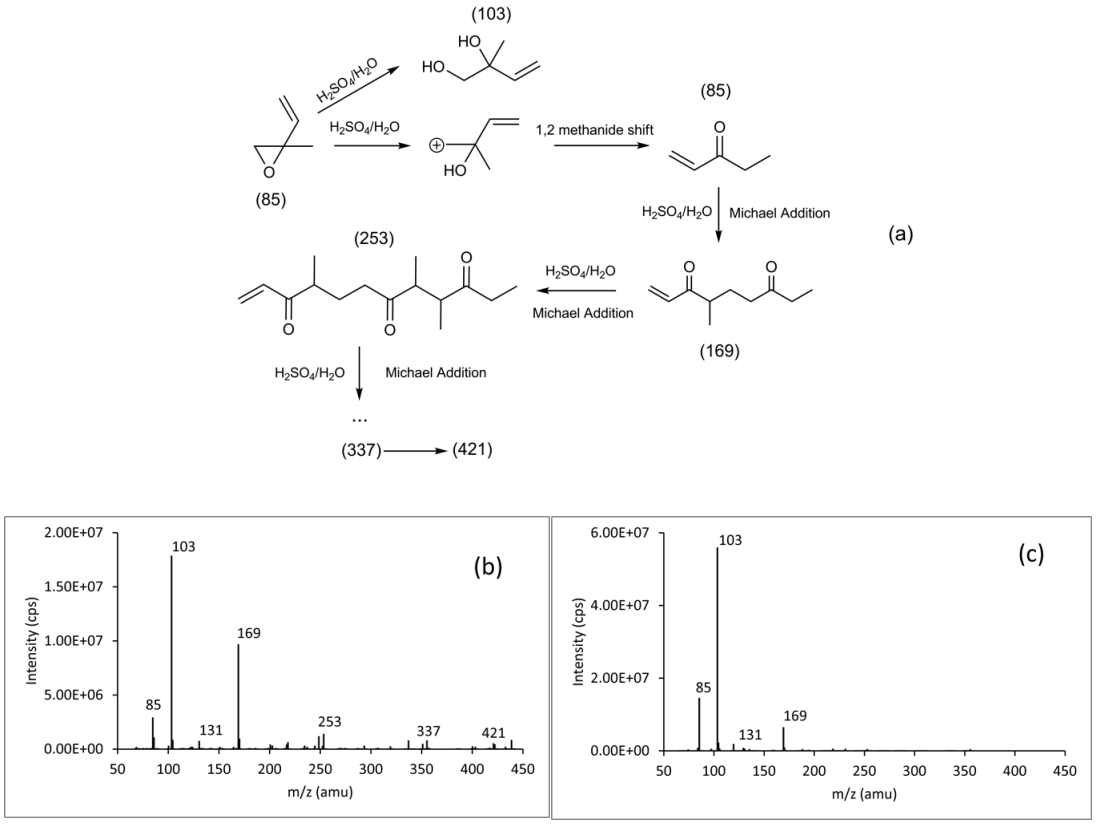

Figure 5.5. Reaction of isoprene oxide vapor on sulfuric acid nanoparticles of 20 nm. (a) Schematic reaction mechanism. (b-c) TD-ID-CIMS spectrum of 20 nm sulfuric acid nanoparticles after exposure to isoprene oxide vapor at 4 and 32% RHs, respectively.

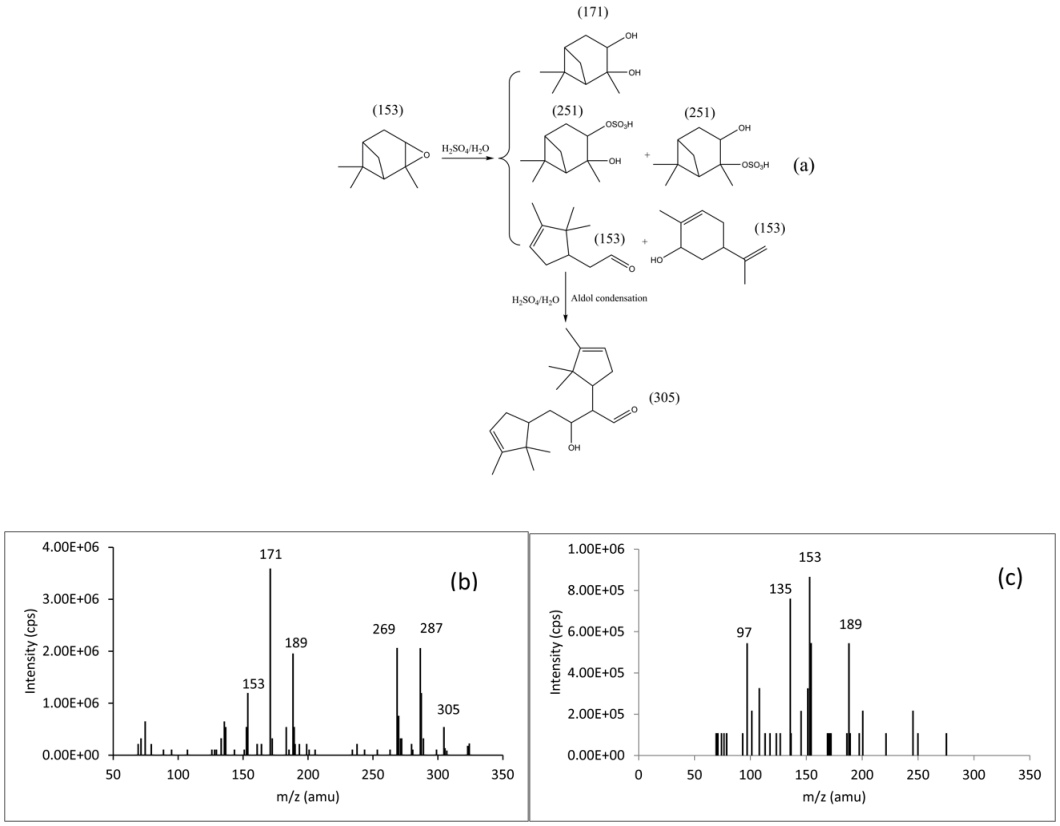

Figure 5.6. Reaction of α-pinene oxide vapor on sulfuric acid nanoparticles of 40 nm. (a) Schematic reaction mechanism. (b-c) TD-ID-CIMS spectrum of 40 nm sulfuric acid nanoparticles after exposure to α-pinene oxide vapor at 5 and 20% RHs, respectively.

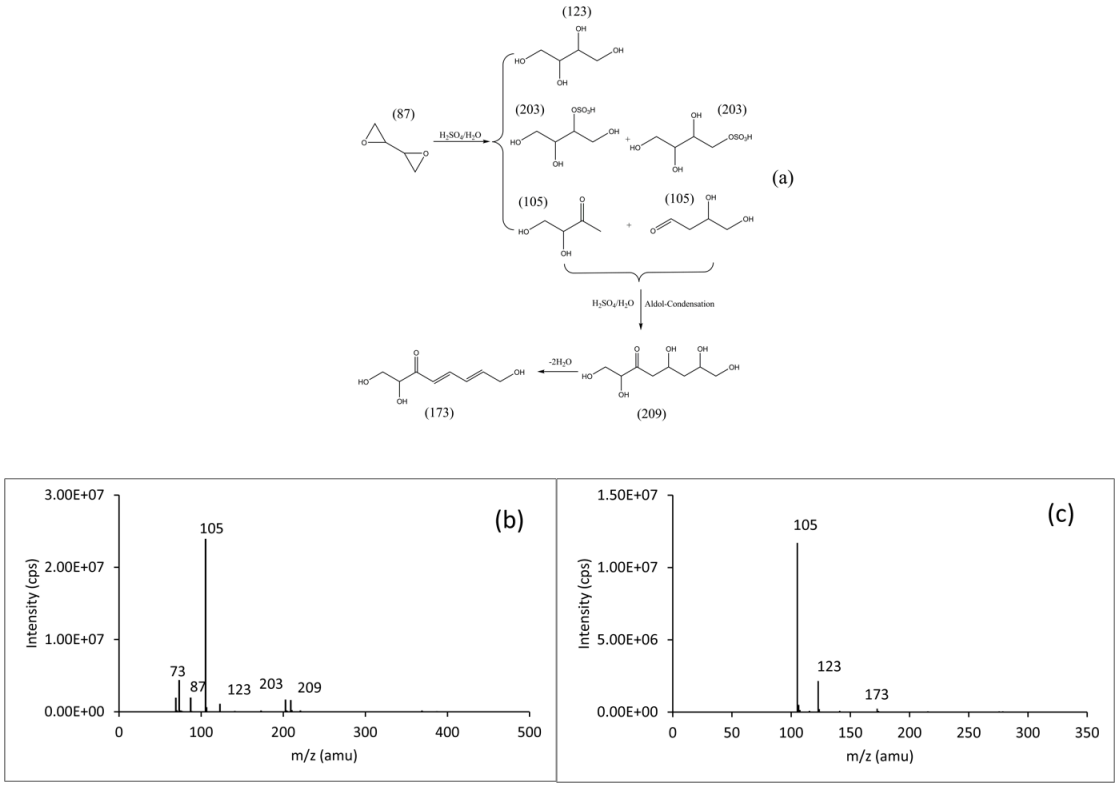

Figure 5.7. Reaction of butadiene diepoxides vapor on sulfuric acid nanoparticles of 40 nm. (a) Schematic reaction mechanism. (b-c) TD-ID-CIMS spectrum of 40 nm sulfuric acid nanoparticles after exposure to butadiene diepoxides vapor at 4 and 32% RHs, respectively.

Table 5.3. Assignment of major peaks in the mass spectrum.

Mass spectrum number	Peak position (m/e)	Structures ($[M \cdot H]^+$)
Isoprene oxide (a) and (b)	103	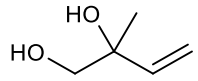
	169	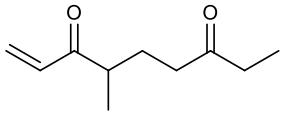
	85	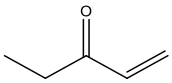
	337	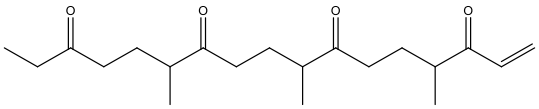
	421	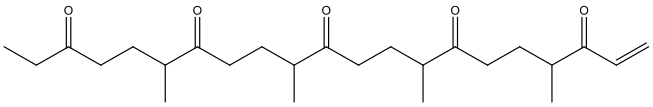
Alpha-pinene oxide[a] (c) and (d)	171	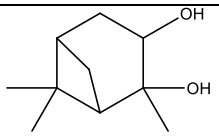
	269	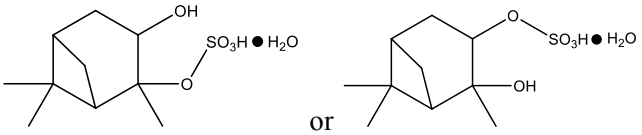
	153	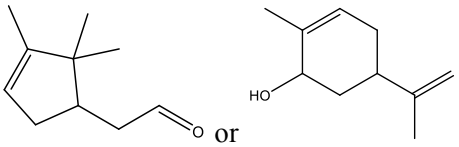
	189	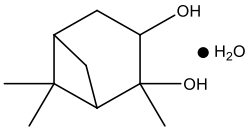

Table 5.3. Continued

Mass spectrum number	Peak position (m/e)	Structures ($[M \cdot H]^+$)
Butadiene diepoxide (e) and (f)	105	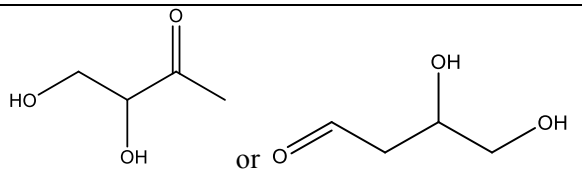
	123	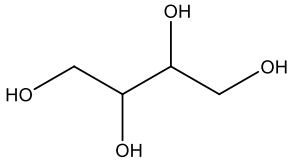
	203	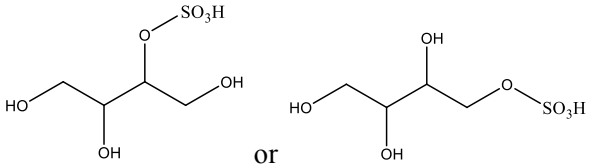
	209[b]	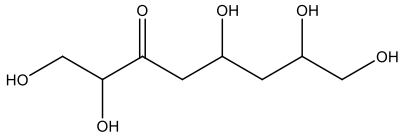
	173[b]	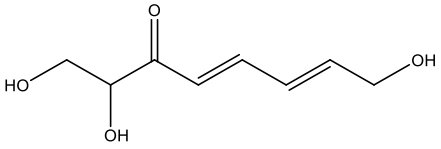

a. Possible structures taken from Iinuma et al.
b. Only one possible structure is presented.

5.3 Conclusion

In summary, we studied the growth magnitude and mechanisms for isoprene oxide, *α*-pinene oxide, and butadiene diepoxides. Our results show that of the classes of organics studied here epoxides are the only kind of species that significantly enhance nanoparticle growth at size

down to 4 nm. For comparable reactant concentrations (1ppb), our results show that the growth rate for isoprene oxide is 0.12 nm h^{-1}, which is much larger than 0.02, 0.008, and 0.008 nm h^{-1} for trimethylamine, glyoxal, and 2-4 hexandienal, respectively.[97] The unique growth properties at 4 nm make epoxide important in stabilization of the freshly nucleated nanoparticles. The growth factors for the three epoxides decrease with increasing RH. The size and concentration dependence studies for isoprene oxide at 43% RH show that at 1 ppb isoprene oxide concentration, the growth rates are 0.09, 0.17, 0.28, 0.37, 0.63 and 0.87 nm h^{-1} for 4, 6, 8, 10, 15, and 20 nm sulfuric acid nanoparticles, respectively. The positive correlation between particle sizes and uptake coefficients of isoprene oxide on sulfuric acid nanoparticles clearly reveals the presence of the Kelvin effect. By extrapolation, we obtained a lower bound (10^{-3}) on the uptake coefficient of isoprene oxide on planar sulfuric acid surface at 43% RH. The chemical composition analysis of sulfuric acid nanoparticles after epoxides exposure indicates that both α-pinene oxide and butadiene diepoxides form organosulfates with sulfuric acid nanoparticles, while isoprene oxide only forms oligomers. Both organosulfates and oligomers are non-volatile and hence contributive to nanoparticle growth. Organosulfates are only formed in low RH or high acidity conditions. In contrast, isoprene derived polymers are formed in both low and high RH conditions by acid catalyzation. The current study shows that epoxides play an important role in the atmospheric nanoparticle growth.

5.4 Methods

Sulfuric acid nanoparticles were produced either using a TSI atomizer or by homogeneous binary nucleation.[98] The freshly generated nanoparticles with broad size spectrum were subsequently charged by a ^{210}Po radioactive source. The charged particles were size selected by a nano differential mobility analyzer (n-DMA) and the resulting monodispersed nanoparticles were passed through a stainless steel reaction tube with an inner diameter of about

1.0 inch. The residence time for the mondispersed nanoparticles in the reaction tube was estimated to be about 3 s, considering about 3000 sccm for the flow rate. Epoxide vapors were added upstream of the reaction tube to be mixed with the nanoparticles. The sulfuric acid nanoparticles after epoxides exposure were passed into a second n-DMA, where size changes of sulfuric acid nanoparticles before and after epoxides exposure were detected.

The chemically modified sulfuric acid nanoparticles were also introduced into an electrostatic particle precipitator. As 6 kV was applied to the precipitator, the nanoparticles were collected on a platinum filament that was protected by a sheath flow of 400 sccm. After about 10 minutes of collection, the filament was pushed into the ID-CIMS evaporation port and a small AC voltage was applied to the filament to evaporate the nanoparticles by heating. Hydronium was used as the reagent ion in all ID-CIMS measurements. All ID-CIMS spectra were recorded in a range from 60 to 450 amu.

5.5 Supporting information

5.5.1 Size dependent growth rates & accommodation coefficients calculation

Since the largest particle is 20 nm which is much smaller than 100 nm, the kinetic regime growth mechanism is applicable.[87] The molar flux of epoxides (J_k) to the nanoparticle surface is shown in the equation below (R_p nanoparticle radius, ω thermal kinetic speed, α_r size dependent uptake coefficient, and $[A]$ concentration of epoxides).

$$J_k = \pi R_p^2 \omega \alpha_r [A] \tag{5.1}$$

Therefore, the growth rate of the nanoparticles can be derived from the mass conservation law (ρ_p the density of nanoparticles, and M_A the molecular mass of condensing species).

$$\rho_p 4\pi R_p^2 \frac{dR_p}{dt} \frac{1}{M_A} = J_k \tag{5.2}$$

Solving the above differential equation using the initial condition R_{p0} at 0, the time and concentration dependence of growth factor is obtained.

$$Gf = 1 + \frac{M_A \omega \alpha_r [A]}{4 \rho_p R_{p0}} t \tag{5.3}$$

According to equation (5.3), the growth factor is linearly dependent on the exposure time and the concentration of the condensing vapor. Fitting the data points in Figure 5.3 via the equation (5.3), the growth rates for sulfuric acid nanoparticles of various sizes in unit time (s) and epoxides concentration (ppm) were obtained. The thermal kinetic speed (ω) at 298.15 K is 274.13 m s^{-1} for isoprene oxide. The molecular mass of isoprene oxide (M_A) is 84 g mol^{-1}. Assuming 1 g cm^{-3} for the density of the nanoparticle, the size dependent uptake coefficients (α_r) can be obtained from the size dependent growth rates.

5.5.2 Planar surface accommodation coefficient & Kelvin effect characteristic length calculation

From the size dependent uptake coefficients, the uptake coefficient for planar surface (α_∞) and the Kelvin effect characteristic diameter (d_σ)[196] were extracted via nonlinear curve fitting using the following equation (see Figure 5.4).

$$\alpha_r = \frac{\alpha_\infty}{\exp(\frac{d_\sigma}{d})} \tag{5.4}$$

6. HYGROSCOPICITY AND CCN ACTIVITY OF NANOPARTICLES COMPOSED OF POLYMERS

6.1 Introduction

Aerosols have been the focus of atmospheric research for many years because of their importance in influencing the earth radiation budget, affecting human health, and changing the atmospheric chemistry pathways.[57-60,62,135] Aerosols are known to influence the earth radiation budget mainly in two ways, i.e., directly by absorbing or scattering the incoming sunlight or indirectly by changing the cloud coverage, lifetime, and albedo through acting as cloud condensation nuclei. Currently, the direct and indirect effects of aerosols represent the largest uncertainties in the projection of future climate,[57] which is mainly due to the highly elusive formation mechanism and complicated physicochemical properties of aerosols.[57]

It is known that aerosols can be formed via two pathways, primary emission and secondary formation. Primarily emitted aerosols are mainly composed of black carbon, sea salt, mineral dust, etc., while secondarily generated aerosols are mainly composed of sulfate, nitrate, ammonia, amines, organics, etc. Secondary aerosols constitute the largest portion of atmospheric aerosols. The physicochemical properties of aerosols, such as single scattering albedo (SSA), density, hygroscopicity, cloud condensation nuclei (CCN) activity, are all solely determined by their molecular compositions.[96] The molecular composition of aerosols also influences the partitioning of gas phase species into aerosol phase, which in return changes the molecular composition of aerosols.[88,89,93] As a result, the physicochemical properties of aerosols are not static but dynamically linked to the environment (volatile organic compounds VOCs) around the aerosols.

Recently, it is discovered that uptake of volatile organics, such as amines, glyoxal, 2-4 hexadienal, and epoxides, on aerosol surfaces enlarges the size of aerosols.[97,98] As the VOCs react with chemicals on/in aerosols, the molecular composition of aerosols are also changed. For instance, some high molecular weight species (oligomers) have been observed in the case of uptake of glyoxal and epoxides on aerosols composed of sulfuric acid and water.[97,98] Due to the high molecular weight of oligomers, the hygroscopicity (or kappa) and CCN activity of the aerosols are decreased. For the case of amines, aminium sulfate salts are formed after the uptake. It has been shown that the formation of aminium salts changes the deliquescence (or equivalently solubility) of aerosols.[171-173,198]

Therefore, in the present study, we try to mimic the real situation of the atmosphere in the lab, by generating aerosols composed of oligomers and study their hygroscopicity and CCN activity. Simply speaking, solutions of glyoxal in water, 2-4 hexadienal in dilute sulfuric acid, methylglyoxal in organic acid, or sucrose in water are atomized to generate poly-dispersed aerosols of a size spectrum from 20 to 300 nm. Subsequently, these poly-dispersed aerosols are sent to a hygroscopicity tandem differential mobility analyzer (h-TDMA) and CCN counter system, from which the information about hygroscopicity and CCN activity is obtained. More detailed information is presented in the methods and results sections.

6.2 Methods

The solution of glyoxal is made by adding glyoxal trimer dihydrate (GTD) (Sigma Aldrich, 97%) to 300 ml of distilled water. GTD is already in polymerized form and has a molecular weight of 210 g mol^{-1}. The solution of 2-4 hexadienal is made by adding 21 droplets of 2-4 hexadienal (Sigma Aldrich, 95%) and 15 droplets of concentrated sulfuric acid (Sigma Aldrich, 95.0%-98.0%) to 300 ml of distilled water. The solution of methylglyoxal with glycolic acid is made by premixing methylglyoxal with glycolic acid in a vial and then dissolving the

mixture in distilled water. The solution of sucrose is made simply by dissolve the table sugar in distilled water. Aerosols containing oligomers are generated using a TSI aerosol generator 3076 with the corresponding solutions. After the generation of poly-dispersed aerosols, a differential mobility analyzer (DMA) is used to scan the size spectrum of the aerosols and select a particular size. The mono-dispersed aerosols after the first DMA are exposed to various relative humidities, from 10% to 90% with a 10% increasing step. The size changes of the mono-dispersed aerosols are detected at the second DMA. Hygroscopic growth factor is defined as the ratio of the sizes detected at the second DMA to the first DMA.

For CCN measurement, the size spectrum (CN spectrum) of dry (RH<10%) poly-dispersed aerosols is obtained by scanning the voltage of the first DMA. Simultaneously, the size selected dry aerosols are sent to a DMT-CCN counter (Droplet Measurement Technology), inside which the mono-dispersed aerosols are either activated or non-activated, depending on their size, chemical composition, and supersaturation. Based on the CCN and CN spectrum, the CCN activation efficiency curve is obtained and Dp50 (defined as the size of aerosols with 50% activation efficiency at given supersaturation) is determined.

Based on the hygroscopic curves and Dp50, the average kappa values of the aerosols are derived and compared with the "bottom-up" molecular weight kappa calculation.

6.3 Results and discussion

Figure 6.1 displays the hygroscopic curve of aerosols generated by atomizing GTD solution. The figure shows that the hygroscopic growth factor does not vary much as the size changes, which is expect since at this large size the Kelvin effect is negligible and hygroscopicity is solely determined by the molecular composition. The hygroscopic curve of GTD does not show a clear deliquescence behavior, which indicates a high solubility of GTD in water. From the hygroscopic curves and using equation (1.45a), the kappa value of GTD

aerosols is derived from linear fit of experimental data, which are shown in Figure 6.2. The kappa value of GTD lies in the range of 0.17 to 0.25, which is low compared with 0.53 for ammonia sulfate.[96]

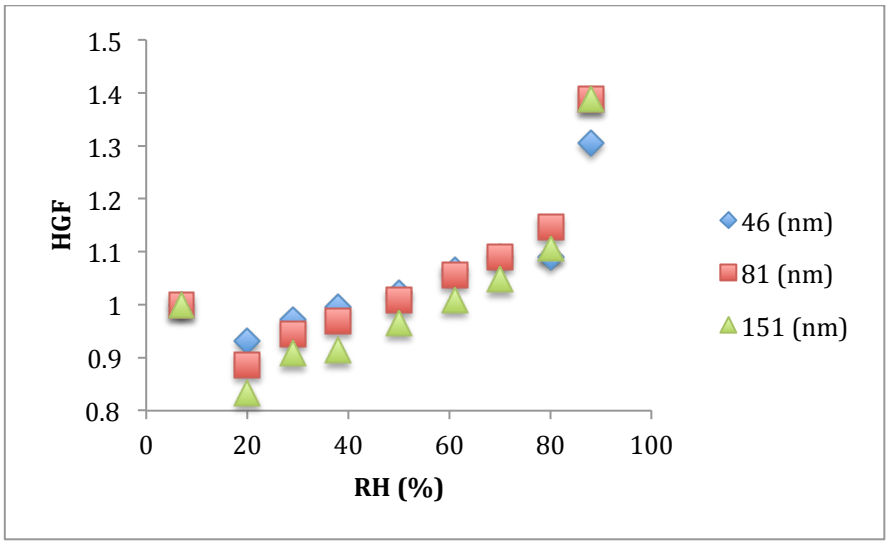

Figure 6.1. Hygroscopic curves of GTD aerosols with diameter of 46, 81, 151 nm.

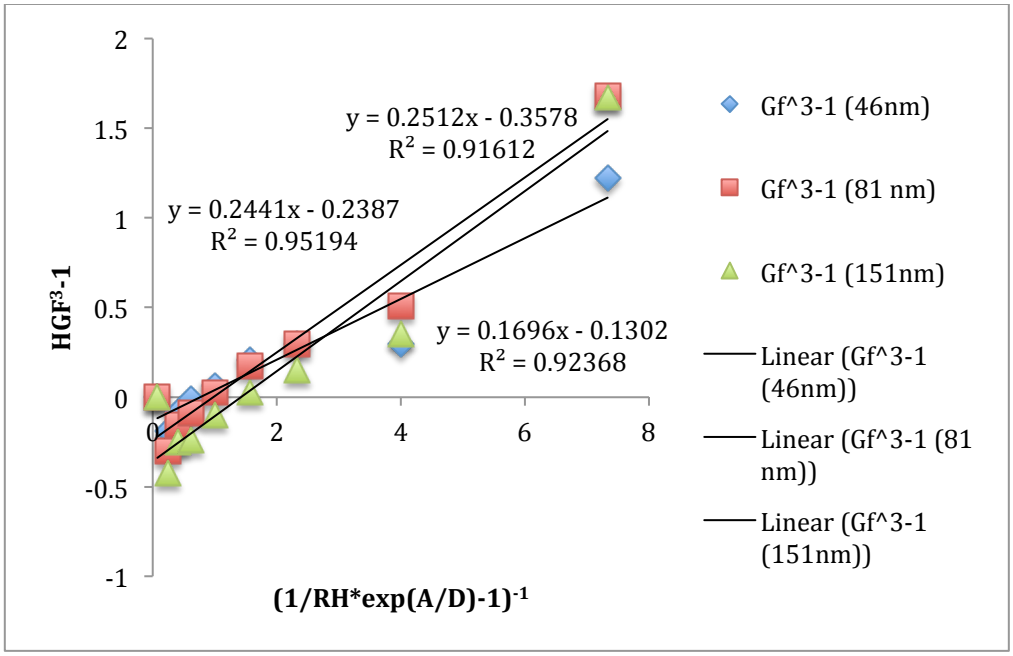

Figure 6.2. Kappa determination from hygroscopicity curves.

In addition to the hygroscopicity curves, Figure 6.3 displays the cloud nuclei (CN) and cloud condensation nuclei (CCN) spectra at three nominal supersaturation values of 0.2% (0.188%), 0.4% (0.316%), and 0.6% (0.516%). The CCN spectra show that smaller size aerosols have less activation efficiency compared with larger aerosols at given supersaturation. The activation efficiency of given size aerosols increases with increasing supersaturation. Using the CN and CCN spectra, the activation efficiency of GTD aerosols is calculated and presented in Figure 6.4. In the figure, the size of 50% activation efficiency are determined as 139, 82, and 59 nm, for supersaturation of 0.2%, 0.4%, and 0.6%, respectively. According to equation (1.43f), the kappa value of GTD aerosols is from 0.14 to 0.25, which is very close to the range obtained using hygroscopicity curve data.

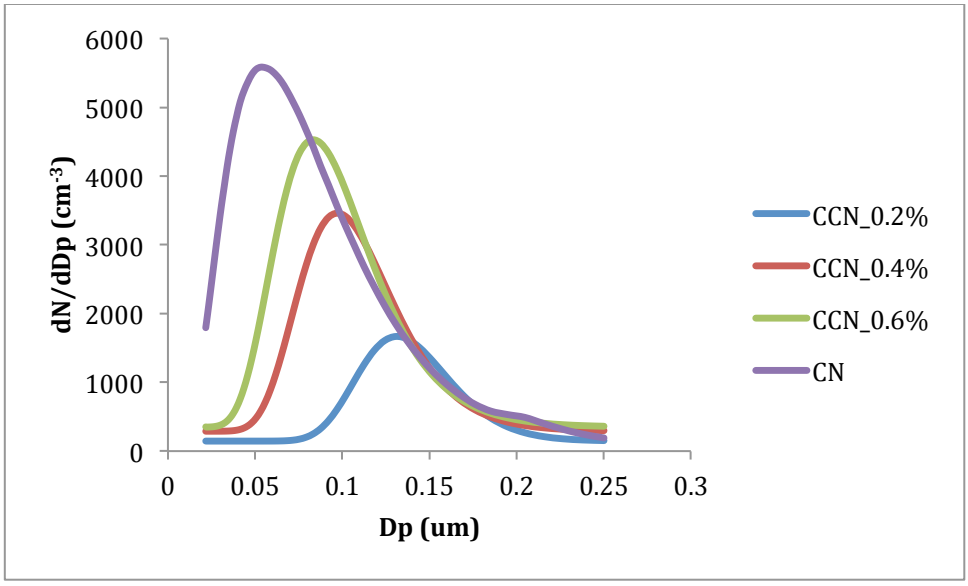

Figure 6.3. CN and CCN spectrum of GTD aerosols generated from atomizing.

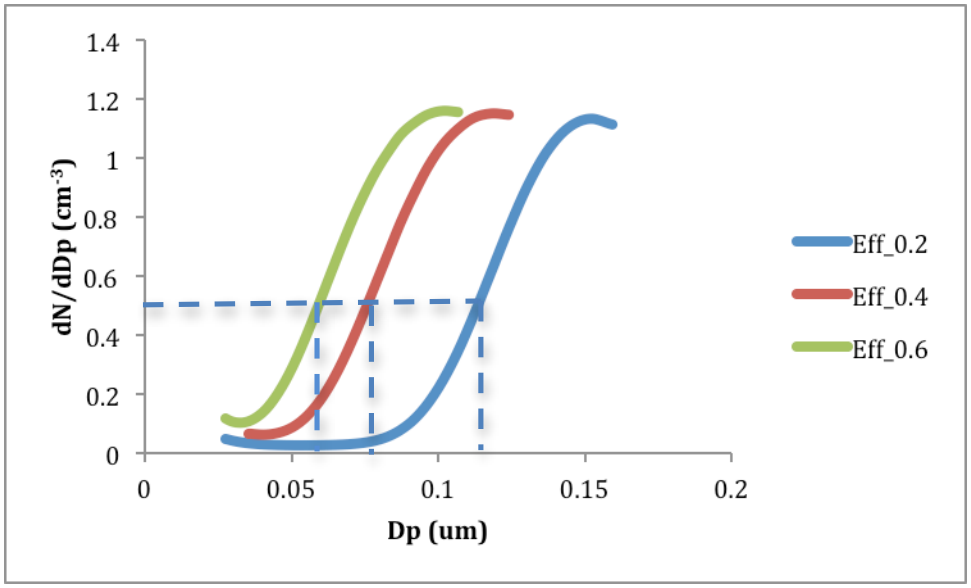

Figure 6.4. The dependence of CCN activation efficiency of GTD aerosols on the size and supersaturation.

The aforementioned two ways of kappa determination are categorized as the "top-down" approach, since the kappa value obtained is averaged over all the molecular compositions of the aerosols. From the molecular composition information of the aerosols, the kappa values can also be calculated using equations (1.39) and (1.41). For aerosols composed solely of GTD, the van Hoff factor is 1. Considering the molecular weight of 210 g mol^{-1} and density of 1.901 g cm^{-3} for GTD, the kappa value is calculated to be 0.16, which is close to or lies in the ranges of 0.17-0.25 and 0.14-0.25 obtained using "top-down" approaches.

For the aerosols composed of 2-4 hexadienal and sulfuric acid mixtures, the hygroscopic growth curves and CCN/CN spectra are shown in Figure 6.5 and 6.6, respectively. The ranges of kappa value derived from hygroscopic growth curves and CCN spectra are 0.513-0.951 and 0.110-0.116, respectively. The kappa values for sulfuric acid and 2-4 hexadienal (calculated based on equation 1.39) are 1.014 and 0.163, respectively. Surprisingly, the kappa value from the hygroscopic growth curve measurement are close to that of sulfuric acid, while the kappa value from CN/CCN spectra measurement are close to that of 2-4 hexadienal.

Using the similar analysis method, the kappa values for methylglyoxal in sulfuric acid, glycolic acid, and sucrose are obtained. The kappa values of the compounds in current study obtained using "hygroscopicity", "CCN", and "definition" methods are summarized in Table 6.1. The CCN, HTDMA, and definition methods agree with each other very well for the case of pure compounds, such as GTD and sucrose. For the case of mixture, since the actually composition of the particles are unknown, the kappa from definition only provides a range of possible values. For the case of methylglyoxal with glycolic acid, the CCN and HTDMA results agree well with each other, while for the case of methylglyoxal and 2-4 hexadienal with sulfuric acid, the CCN and HTDMA results do not agree with each other. The reason for the disagreement of kappa values from CCN and HTMDA involving sulfuric acid is still not clear. Possible explanation is

that the volume fractions (ε_i) of each individual compounds are different for CCN and HTDMA cases.

Table 6.1. Comparison of Kappa values measured using CCN and HTDMA with results from theoretical calculation.

Species	Kappa (definition)	Kappa (CCN)	Kappa (HTDMA)
GTD	0.163	0.189	0.222
GTD+GLA	(0.163, 0.337)	0.081	0.410
MG	0.087	0.053	0.142
MG+SA	(0.087[a],1.014[b])	0.116	0.900
MG+GLA	(0.087[a],0.337[c])	0.090	0.091
2-4-HEX+SA	(0.163[d],1.014[b])	0.114	0.951
2-4-HEX+GLA	(0.163[d], 0.337[c])	0.107	0.258
Sucrose	0.084	0.061	0.101

[a] Kappa value of 3 unit of methylglyoxal, [b] Kappa value of sulfuric acid.
[c] Kappa value of glycolic acid, [d] kappa value of 2-4-hexadienal.

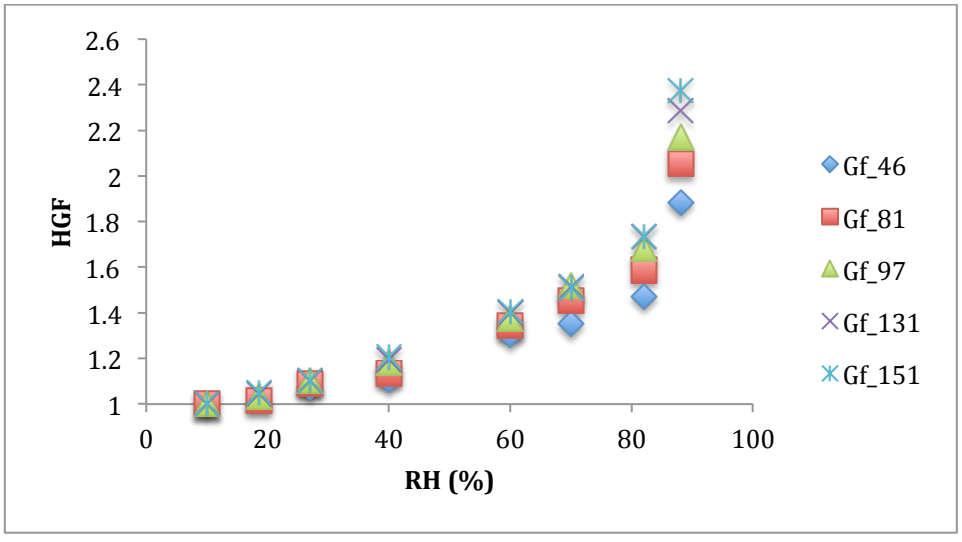

Figure 6.5. Hygroscopic growth curves of aerosols composed of 2-4 hexadienal and sulfuric acid mixture.

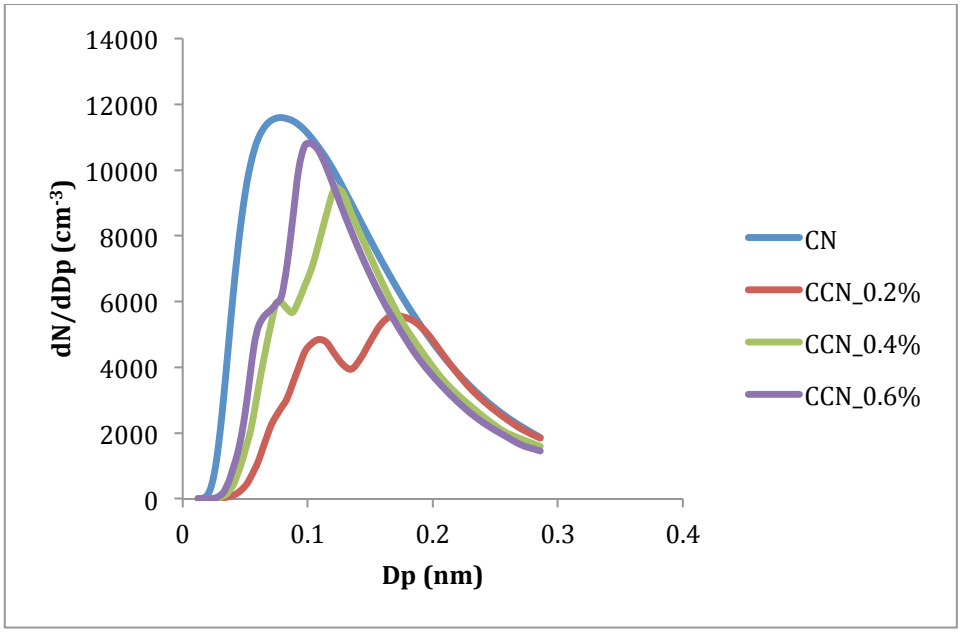

Figure 6.6. CN and CCN spectrum of 2-4 hexadienal/sulfuric acid aerosols generated from atomizing.

6.4 Conclusion

The physicochemical properties of atmospheric aerosols are largely determined by their size and molecular composition. Previous studies have shown that oligomers or polymers are formed after the uptake of certain VOCs on pre-existing aerosol surfaces. The results of current study indicate that the high molecular weight oligomers formed during uptake process reduce the hygroscopicity and CCN activity of aerosols. Therefore, the formation of oligomers in aerosol phase has great impact on the formation of clouds and the indirect effect on the Earth climate. Since in the present study only model compounds, such as GTD, 2-4 hexadienal in dilute sulfuric acid solution, and sucrose are used, it is more desirable that aged aerosols in the atmosphere are directly utilized in the measurement. More researches on the effect of polymers on physicochemical properties of aerosols, including optical properties, are needed in the future.

7. CONCLUDING REMARKS

Atmospheric aerosols have profound impact on the Earth climate, air quality, and human health. Unfortunately, the formation and growth mechanisms of atmospheric aerosols remain largely unknown, especially for secondary aerosols, which are formed through gas-to-particle conversion process. Numerous studies, including experimental and theoretical, have been carried out to elucidate the formation and growth mechanisms for secondary aerosols. It has been discovered that the formation process of secondary aerosols can be roughly divided into two stages, i.e., nucleation to form critical nuclei from gaseous species and subsequent growth of the freshly nucleated nanoparticles. Large uncertainties still exist in the identities of chemicals that participate in the nucleation and growth stages. These uncertainties prevent an accurate representation of secondary aerosols in climate models, which subsequently causes large errors in the output of climate predictions.

Current study concentrates on three aspects, i.e., the nucleation rate dependence on carboxylic acids, the growth of freshly nucleated nanoparticles by organics, and the physicochemical properties of secondary aerosols. These three aspects are interrelated with each other. Our results show that dicarboxylic acid, alike monocarboxylic acid, enhance the nucleation rate of binary sulfuric acid – water system by a factor of 6 to 20. Since carboxylic acids are important oxidation products of VOCs, which have a lager emission budget, the nucleation rate can be enhanced significantly. The increased number concentration of freshly nucleated nanoparticles, because of enhanced nucleation rate, results in higher secondary aerosol loading. These freshly nucleated nanoparticle can further grow to larger sizes by various organics, including amines, glyoxal, 2-4 hexadienal, and epoxide, as shown in this study. Our

results also show that high molecular weight species (polymers or oligomers) are formed in the growth stages, which in return affect the partitioning of gaseous species and hygroscopicity, CCN activity, and optical properties of secondary aerosols.

Although some chemical species that contribute to the nucleation and growth stages of secondary aerosol formation are identified in the current study, most of the identities of chemicals still remain uncertain. More researches are needed in the future to find these chemicals. In addition, the physical and chemical mechanisms of how these chemicals contribute to nucleation are still unclear from theoretical perspective. More theoretical chemistry studies are needed to unravel the mysterious mechanisms. Some additional effort can also be made to characterize the physicochemical properties of secondary aerosols using both existing and newly developed instrumentations.

REFERENCES

(1) Volmer, M.; Weber, A. *Physik. Chem.* **1925**, *119*, 277.

(2) Becker, R.; Doring, W. *Annalen Der Physik* **1935**, *24*, 719.

(3) Frenkel, J. *The Journal of Chemical Physics* **1939**, *7*, 200.

(4) Zeldovich, J. *Theoret. Phys. (U. S. S. R.)* **1942**, *12*, 525.

(5) Kashchiev, D. *Nucleation: Basic theory with applications*; Butterworth-Heinemann: Burlington, 2000.

(6) Stauffer, D. *Journal of Aerosol Science* **1976**, *7*, 319.

(7) Shugard, W. J.; Heist, R. H.; Reiss, H. *The Journal of Chemical Physics* **1974**, *61*, 5298.

(8) Trinkaus, H. *Physical Review B* **1983**, *27*, 7372.

(9) Reiss, H. *The Journal of Chemical Physics* **1950**, *18*, 840.

(10) McGraw, R.; Zhang, R. Y. *Journal of Chemical Physics* **2008**, *128*, 064508.

(11) Zeng, X. C.; Oxtoby, D. W. *Journal of Chemical Physics* **1991**, *95*, 5940.

(12) Zeng, X. C.; Oxtoby, D. W. *Journal of Chemical Physics* **1991**, *94*, 4472.

(13) Oxtoby, D. W. *Journal of Physics: Condensed Matter* **1992**, *4*, 7627.

(14) Talanquer, V.; Oxtoby, D. W. *Journal of Chemical Physics* **1994**, *100*, 5190.

(15) Nyquist, R. M.; Talanquer, V.; Oxtoby, D. W. *Journal of Chemical Physics* **1995**, *103*, 1175.

(16) Shen, Y. C.; Oxtoby, D. W. *Journal of Chemical Physics* **1996**, *105*, 6517.

(17) Lutsko, J. F. *Journal of Chemical Physics* **2011**, *134*.

(18) Lutsko, J. F. *Journal of Chemical Physics* **2008**, *129*.

(19) Chen, B.; Siepmann, J. I. *The Journal of Physical Chemistry B* **2000**, *104*, 8725.

(20) Chen, B.; Siepmann, J. I.; Oh, K. J.; Klein, M. L. *Journal of Chemical Physics* **2001**, *115*, 10903.

(21) Chen, B.; Siepmann, J. I.; Oh, K. J.; Klein, M. L. *Journal of Chemical Physics* **2002**, *116*, 4317.

(22) Chen, B.; Siepmann, J. I.; Klein, M. L. *The Journal of Physical Chemistry A* **2005**, *109*, 1137.

(23) Schenter, G. K.; Kathmann, S. M.; Garrett, B. C. *Physical Review Letters* **1999**, *82*, 3484.

(24) Kathmann, S. M.; Schenter, G. K.; Garrett, B. C. *Journal of Chemical Physics* **1999**, *111*, 4688.

(25) Kathmann, S. M.; Schenter, G. K.; Garrett, B. C. *The Journal of Chemical Physics* **2004**, *120*, 9133.

(26) Kathmann, S. M.; Schenter, G. K.; Garrett, B. C.; Chen, B.; Siepmann, J. I. *The Journal of Physical Chemistry C* **2009**, *113*, 10354.

(27) Crosby, L. D.; Kathmann, S. M.; Windus, T. L. *Journal of Computational Chemistry* **2009**, *30*, 743.

(28) Kurten, T.; Sundberg, M. R.; Vehkamaki, H.; Noppel, M.; Blomqvist, J.; Kulmala, M. *Journal of Physical Chemistry A* **2006**, *110*, 7178.

(29) Kurten, T.; Torpo, L.; Ding, C. G.; Vehkamaki, H.; Sundberg, M. R.; Laasonen, K.; Kulmala, M. *Journal of Geophysical Research-Atmospheres* **2007**, *112*.

(30) Kurten, T.; Vehkamaki, H. In *Advances in quantum chemistry, Vol 55: Applications of theoretical methods to atmospheric science*; Elsevier Academic Press Inc: San Diego, 2008; Vol. 55, p 407.

(31) Kurten, T.; Loukonen, V.; Vehkamaki, H.; Kulmala, M. *Atmospheric Chemistry and Physics* **2008**, *8*, 4095.

(32) Loukonen, V.; Kurten, T.; Ortega, I. K.; Vehkamaki, H.; Padua, A. A. H.; Sellegri, K.; Kulmala, M. *Atmospheric Chemistry and Physics* **2010**, *10*, 4961.

(33) Kurten, T.; Kuang, C. A.; Gomez, P.; McMurry, P. H.; Vehkamaki, H.; Ortega, I.; Noppel, M.; Kulmala, M. *Journal of Chemical Physics* **2010**, *132*.

(34) Kurtén, T. *Entropy* **2011**, *13*, 915.

(35) Nadykto, A. B.; Yu, F. Q. *Chemical Physics Letters* **2007**, *435*, 14.

(36) Nadykto, A. B.; Al Natsheh, A.; Yu, F. Q.; Mikkelsen, K. V.; Herb, J. In *Advances in Quantum Chemistry, Vol 55: Applications of Theoretical Methods to Atmospheric Science*; Elsevier Academic Press Inc: San Diego, 2008; Vol. 55, p 449.

(37) Xu, Y.; Nadykto, A. B.; Yu, F.; Herb, J.; Wang, W. *The Journal of Physical Chemistry A* **2009**, *114*, 387.

(38) Nadykto, A. B.; Yu, F.; Herb, J. *Chemical Physics* **2009**, *360*, 67.

(39) Xu, Y.; Nadykto, A. B.; Yu, F.; Jiang, L.; Wang, W. *Journal of Molecular Structure: THEOCHEM* **2010**, *951*, 28.

(40) Nadykto, A.; Yu, F.; Jakovleva, M.; Herb, J.; Xu, Y. *Entropy* **2011**, *13*, 554.

(41) Herb, J.; Nadykto, A. B.; Yu, F. *Chemical Physics Letters* **2011**, *518*, 7.

(42) Herb, J.; Xu, Y.; Yu, F.; Nadykto, A. B. *The Journal of Physical Chemistry A* **2012**, *117*, 133.

(43) Xu, W.; Zhang, R. *The Journal of Physical Chemistry A* **2012**, *116*, 4539.

(44) Zhao, J. Dissertation, 2007.

(45) Zhang, R.; Suh, I.; Zhao, J.; Zhang, D.; Fortner, E. C.; Tie, X.; Molina, L. T.; Molina, M. J. *Science* **2004**, *304*, 1487.

(46) Zhang, R. Y.; Wang, L.; Khalizov, A. F.; Zhao, J.; Zheng, J.; McGraw, R. L.; Molina, L. T. *Proceedings of the National Academy of Sciences of the United States of America* **2009**, *106*, 17650.

(47) Zhao, J.; Khalizov, A.; Zhang, R. Y.; McGraw, R. *Journal of Physical Chemistry A* **2009**, *113*, 680.

(48) Xu, W.; Zhang, R. *The Journal of Chemical Physics* **2013**, *139*, 064312.

(49) Strey, R.; Wagner, P. E.; Schmeling, T. *The Journal of Chemical Physics* **1986**, *84*, 2325.

(50) Anisimov, M. P.; Fominykh, E. G.; Akimov, S. V.; Hopke, P. K. *Journal of Aerosol Science* **2009**, *40*, 733.

(51) Zhang, R.; Khalizov, A.; Wang, L.; Hu, M.; Xu, W. *Chemical Reviews* **2011**, *112*, 1957.

(52) Yuan, W.; Pang, H.; Zeng, W.; Jia, J. *Statistics*; 2nd ed.; Higher Education Press, 2006.

(53) Peters, F.; Paikert, B. *The Journal of Chemical Physics* **1989**, *91*, 5672.

(54) Katz, J. L. *The Journal of Chemical Physics* **1970**, *52*, 4733.

(55) Vohra, V.; Heist, R. H. *The Journal of Chemical Physics* **1996**, *104*, 382.

(56) Strey, R.; Wagner, P. E.; Viisanen, Y. *The Journal of Physical Chemistry* **1994**, *98*, 7748.

(57) Solomon, S.; Qin, D.; Manning, M.; Chen, Z.; Marquis, M.; Averyt, K. B.; Tignor, M.; Miller, H. L. *In climate change 2007: The physical science basis.*; 4 ed.; Cambridge University Press: Cambridge, United Kingdom and New York, NY, USA, 2007.

(58) EPA *Air quality criteria for particulate matter*; U.S. Environmental Protection Agency, 2004.

(59) Zhang, R. Y.; Li, G. H.; Fan, J. W.; Wu, D. L.; Molina, M. J. *Proceedings of the National Academy of Sciences of the United States of America* **2007**, *104*, 5295.

(60) Molina, M. J.; Molina, L. T.; Zhang, R. Y.; Meads, R. F.; Spencer, D. D. *Geophysical Research Letters* **1997**, *24*, 1619.

(61) Zhang, R. Y.; Leu, M. T.; Molina, M. J. *Geophysical Research Letters* **1996**, *23*, 1669.

(62) Li, G. H.; Zhang, R. Y.; Fan, J. W.; Tie, X. X. *Journal of Geophysical Research-Atmospheres* **2005**, *110*, D23206.

(63) Fan, J. W.; Zhang, R. Y.; Collins, D.; Li, G. H. *Geophysical Research Letters* **2006**, *33*, L15802.

(64) Ball, S. M.; Hanson, D. R.; Eisele, F. L.; McMurry, P. H. *J. Geophys. Res.* **1999**, *104*, 23709.

(65) Young, L. H.; Benson, D. R.; Kameel, F. R.; Pierce, J. R.; Junninen, H.; Kulmala, M.; Lee, S. H. *Atmos. Chem. Phys.* **2008**, *8*, 4997.

(66) Yu, F.; Turco, R. P. *J. Geophys. Res.* **2001**, *106*, 4797.

(67) Lee, S.-H.; Reeves, J. M.; Wilson, J. C.; Hunton, D. E.; Viggiano, A. A.; Miller, T. M.; Ballenthin, J. O.; Lait, L. R. *Science* **2003**, *301*, 1886.

(68) Metzger, A.; Verheggen, B.; Dommen, J.; Duplissy, J.; Prevot, A. S. H.; Weingartner, E.; Riipinen, I.; Kulmala, M.; Spracklen, D. V.; Carslaw, K. S.; Baltensperger, U. *Proceedings of the National Academy of Sciences of the United States of America* **2010**, *107*, 6646.

(69) Kulmala, M.; Kontkanen, J.; Junninen, H.; Lehtipalo, K.; Manninen, H. E.; Nieminen, T.; Petäjä, T.; Sipilä, M.; Schobesberger, S.; Rantala, P.; Franchin, A.; Jokinen, T.; Järvinen, E.; Äijälä, M.; Kangasluoma, J.; Hakala, J.; Aalto, P. P.; Paasonen, P.; Mikkilä, J.; Vanhanen, J.; Aalto, J.; Hakola, H.; Makkonen, U.; Ruuskanen, T.; Mauldin, R. L.; Duplissy, J.; Vehkamäki, H.; Bäck, J.; Kortelainen, A.; Riipinen, I.; Kurtén, T.; Johnston, M. V.; Smith, J. N.; Ehn, M.; Mentel, T. F.; Lehtinen, K. E. J.; Laaksonen, A.; Kerminen, V.-M.; Worsnop, D. R. *Science* **2013**, *339*, 943.

(70) Brus, D.; Neitola, K.; Hyvärinen, A. P.; Petäjä, T.; Vanhanen, J.; Sipilä, M.; Paasonen, P.; Kulmala, M.; Lihavainen, H. *Atmos. Chem. Phys.* **2011**, *11*, 5277.

(71) Kirkby, J.; Curtius, J.; Almeida, J.; Dunne, E.; Duplissy, J.; Ehrhart, S.; Franchin, A.; Gagne, S.; Ickes, L.; Kurten, A.; Kupc, A.; Metzger, A.; Riccobono, F.; Rondo, L.; Schobesberger, S.; Tsagkogeorgas, G.; Wimmer, D.; Amorim, A.; Bianchi, F.; Breitenlechner, M.; David, A.; Dommen, J.; Downard, A.; Ehn, M.; Flagan, R. C.; Haider, S.; Hansel, A.; Hauser, D.; Jud, W.; Junninen, H.; Kreissl, F.; Kvashin, A.; Laaksonen, A.; Lehtipalo, K.; Lima, J.; Lovejoy, E. R.; Makhmutov, V.; Mathot, S.; Mikkila, J.; Minginette, P.; Mogo, S.; Nieminen, T.; Onnela, A.; Pereira, P.; Petaja, T.; Schnitzhofer, R.; Seinfeld, J. H.; Sipila, M.; Stozhkov, Y.; Stratmann, F.; Tome, A.; Vanhanen, J.; Viisanen, Y.; Vrtala, A.; Wagner, P. E.; Walther, H.; Weingartner, E.; Wex, H.; Winkler, P. M.; Carslaw, K. S.; Worsnop, D. R.; Baltensperger, U.; Kulmala, M. *Nature* **2011**, *476*, 429.

(72) Paasonen, P.; Nieminen, T.; Asmi, E.; Manninen, H. E.; Petaja, T.; Plass-Dulmer, C.; Flentje, H.; Birmili, W.; Wiedensohler, A.; Horrak, U.; Metzger, A.; Hamed, A.; Laaksonen, A.; Facchini, M. C.; Kerminen, V. M.; Kulmala, M. *Atmospheric Chemistry and Physics* **2010**, *10*, 11223.

(73) Vuollekoski, H.; Nieminen, T.; Paasonen, P.; Sihto, S. L.; Boy, M.; Manninen, H.; Lehtinen, K.; Kerminen, V. M.; Kulmala, M. *Atmospheric Research* **2010**, *98*, 229.

(74) Berndt, T.; Stratmann, F.; Sipila, M.; Vanhanen, J.; Petaja, T.; Mikkila, J.; Gruner, A.; Spindler, G.; Mauldin, R. L.; Curtius, J.; Kulmala, M.; Heintzenberg, J. *Atmospheric Chemistry and Physics* **2010**, *10*, 7101.

(75) Sipilä, M.; Berndt, T.; Petäjä, T.; Brus, D.; Vanhanen, J.; Stratmann, F.; Patokoski, J.; Mauldin, R. L.; Hyvärinen, A.-P.; Lihavainen, H.; Kulmala, M. *Science* **2010**, *327*, 1243.

(76) Herrmann, E.; Brus, D.; Hyvarinen, A. P.; Stratmann, F.; Wilck, M.; Lihavainen, H.; Kulmala, M. *Journal of Physical Chemistry A* **2010**, *114*, 8033.

(77) Nieminen, T.; Manninen, H. E.; Sihto, S. L.; Yli-Juuti, T.; Mauldin, R. L.; Petaja, T.; Riipinen, I.; Kerminen, V. M.; Kulmala, M. *Environmental Science & Technology* **2009**, *43*, 4715.

(78) Sihto, S. L.; Kulmala, M.; Kerminen, V. M.; Dal Maso, M.; Petaja, T.; Riipinen, I.; Korhonen, H.; Arnold, F.; Janson, R.; Boy, M.; Laaksonen, A.; Lehtinen, K. E. J. *Atmospheric Chemistry and Physics* **2006**, *6*, 4079.

(79) Napari, I.; Noppel, M.; Vehkamaki, H.; Kulmala, M. *Journal of Chemical Physics* **2002**, *116*, 4221.

(80) Viisanen, Y.; Kulmala, M.; Laaksonen, A. *The Journal of Chemical Physics* **1997**, *107*, 920.

(81) Zhang, R. Y. *Science* **2010**, *328*, 1366.

(82) Yue, D. L.; Hu, M.; Zhang, R. Y.; Wang, Z. B.; Zheng, J.; Wu, Z. J.; Wiedensohler, A.; He, L. Y.; Huang, X. F.; Zhu, T. *Atmospheric Chemistry and Physics* **2010**, *10*, 4953.

(83) Yu, H.; McGraw, R.; Lee, S.-H. *Geophys. Res. Lett.* **2012**, *39*, L02807.

(84) Sipila, M.; Lehtipalo, K.; Attoui, M.; Neitola, K.; Petaja, T.; Aalto, P. P.; O'Dowd, C. D.; Kulmala, M. *Aerosol Science and Technology* **2009**, *43*, 126.

(85) Kim, C. S.; Okuyama, K.; de la Mora, J. F. *Aerosol Science and Technology* **2003**, *37*, 791.

(86) Vanhanen, J.; Mikkila, J.; Lehtipalo, K.; Sipila, M.; Manninen, H. E.; Siivola, E.; Petaja, T.; Kulmala, M. *Aerosol Science and Technology* **2011**, *45*, 533.

(87) Seinfeld, J. H.; Pandis, S. N. *Atmospheric Chemistry and Physics - From Air Pollution to Climate Change*; 2nd ed.; John Wiley & Sons, 2006.

(88) Pankow, J. F. *Atmospheric Environment* **1994**, *28*, 185.

(89) Pankow, J. F. *Atmospheric Environment* **1994**, *28*, 189.

(90) Zuend, A.; Marcolli, C.; Luo, B. P.; Peter, T. *Atmos. Chem. Phys.* **2008**, *8*, 4559.

(91) Zuend, A.; Marcolli, C.; Booth, A. M.; Lienhard, D. M.; Soonsin, V.; Krieger, U. K.; Topping, D. O.; McFiggans, G.; Peter, T.; Seinfeld, J. H. *Atmos. Chem. Phys.* **2011**, *11*, 9155.

(92) Zuend, A.; Seinfeld, J. H. *Atmos. Chem. Phys.* **2012**, *12*, 3857.

(93) Donahue, N. M.; Robinson, A. L.; Stanier, C. O.; Pandis, S. N. *Environmental Science & Technology* **2006**, *40*, 2635.

(94) Donahue, N. M.; Epstein, S. A.; Pandis, S. N.; Robinson, A. L. *Atmos. Chem. Phys.* **2011**, *11*, 3303.

(95) Donahue, N. M.; Kroll, J. H.; Pandis, S. N.; Robinson, A. L. *Atmos. Chem. Phys.* **2012**, *12*, 615.

(96) Petters, M. D.; Kreidenweis, S. M. *Atmos. Chem. Phys.* **2007**, *7*, 1961.

(97) Wang, L.; Khalizov, A. F.; Zheng, J.; Xu, W.; Ma, Y.; Lal, V.; Zhang, R. Y. *Nature Geoscience* **2010**, *3*, 238.

(98) Wang, L.; Xu, W.; Khalizov, A.; Zheng, J.; Qiu, C.; Zhang, R. *Journal of Physical Chemistry A* **2011**, *115*, 8940.

(99) Zhang, R.; Khalizov, A.; Wang, L.; Hu, M.; Xu, W. *Chem. Rev.* **2011**.

(100) Kulmala, M.; Pirjola, L.; Makela, J. M. *Nature* **2000**, *404*, 66.

(101) Fan, J. W.; Zhang, R. Y. *Environmental Chemistry* **2004**, *1*, 140.

(102) Zhang, D.; Lei, W. F.; Zhang, R. Y. *Chemical Physics Letters* **2002**, *358*, 171.

(103) Lei, W. F.; Zhang, R. Y. *Journal of Physical Chemistry A* **2001**, *105*, 3808.

(104) Zhao, J.; Levitt, N. P.; Zhang, R. Y.; Chen, J. M. *Environmental Science & Technology* **2006**, *40*, 7682.

(105) Zhao, J.; Levitt, N. P.; Zhang, R. Y. *Geophysical Research Letters* **2005**, *32*.

(106) Hoffmann, T.; Bandur, R.; Marggraf, U.; Linscheid, M. *J. Geophys. Res.* **1998**, *103*, 25569.

(107) Kurtén, T.; Torpo, L.; Sundberg, M. R.; Kerminen, V. M.; Vehkamäki, H.; Kulmala, M. *Atmos. Chem. Phys.* **2007**, *7*, 2765.

(108) Sloth †, M.; Bilde ‡, M.; Mikkelsen *, K. V. *Molecular Physics* **2004**, *102*, 2361.

(109) Ehn, M.; Junninen, H.; Petäjä, T.; Kurtén, T.; Kerminen, V. M.; Schobesberger, S.; Manninen, H. E.; Ortega, I. K.; Vehkamäki, H.; Kulmala, M.; Worsnop, D. R. *Atmos. Chem. Phys.* **2010**, *10*, 8513.

(110) Paul A, M. *Atmospheric Environment* **2001**, *35*, 961.

(111) Chebbi, A.; Carlier, P. *Atmospheric Environment* **1996**, *30*, 4233.

(112) Frisch, M. J.; Trucks, G. W.; Schlegel, H. B.; Scuseria, G. E.; Robb, M. A.; Cheeseman, J. R.; Montgomery, J. A.; Vreven, T.; Kudin, K. N.; Burant, J. C.; Millam, J. M.; Iyengar, S. S.; Tomasi, J.; Barone, V.; Mennucci, B.; Cossi, M.; Scalmani, G.; Rega, N.; Petersson, G. A.; Nakatsuji, H.; Hada, M.; Ehara, M.; Toyota, K.; Fukuda, R.; Hasegawa, J.; Ishida, M.; Nakajima, T.; Honda, Y.; Kitao, O.; Nakai, H.; Klene, M.; Li, X.; Knox, J. E.; Hratchian, H. P.; Cross, J. B.; Bakken, V.; Adamo, C.; Jaramillo, J.; Gomperts, R.; Stratmann, R. E.; Yazyev, O.; Austin, A. J.; Cammi, R.; Pomelli, C.; Ochterski, J. W.; Ayala, P. Y.; Morokuma, K.; Voth, G. A.; Salvador, P.; Dannenberg, J. J.; Zakrzewski, V. G.; Dapprich, S.; Daniels, A. D.; Strain, M. C.; Farkas, O.; Malick, D. K.; Rabuck, A. D.; Raghavachari, K.; Foresman, J. B.; Ortiz, J. V.; Cui, Q.; Baboul, A. G.; Clifford, S.; Cioslowski, J.; Stefanov, B. B.; Liu, G.; Liashenko, A.; Piskorz, P.; Komaromi, I.; Martin, R. L.; Fox, D. J.; Keith, T.; Laham, A.; Peng, C. Y.; Nanayakkara, A.; Challacombe, M.; Gill, P. M. W.; Johnson, B.; Chen, W.; Wong, M. W.; Gonzalez, C.; Pople, J. A. Gaussian 03 Revision C.02, http://gaussian.com/, 2003

(113) Bader, R. F. W. *Atoms in Molecules: a quantum theory*; Clarendon Press: Oxford: New York, 1990.

(114) Biegler-König, F. *Journal of Computational Chemistry* **2000**, *21*, 1040.

(115) Biegler-König, F.; Schönbohm, J.; Bayles, D. *Journal of Computational Chemistry* **2001**, *22*, 545.

(116) Biegler-König, F.; Schönbohm, J. *Journal of Computational Chemistry* **2002**, *23*, 1489.

(117) Reed, A. E.; Curtiss, L. A.; Weinhold, F. *Chemical Reviews* **1988**, *88*, 899.

(118) Kuczkowski, R. L.; Suenram, R. D.; Lovas, F. J. *Journal of the American Chemical Society* **1981**, *103*, 2561.

(119) Huber, K. P.; Herzberg, G. *Constants of Polyatomic Molecules*; V. ed.; Van Nostrand Reinhold: New York, 1979.

(120) Shahat, M. *Acta Crystallogr* **1952**, *1952*.

(121) Derissen, J. L.; Smith, P. H. *Acta Crystallographica Section B* **1974**, *30*, 2240.

(122) Beyer, K. D.; Friesen, K.; Bothe, J. R.; Palet, B. *The Journal of Physical Chemistry A* **2008**, *112*, 11704.

(123) Price, D. J.; Roberts, J. D.; Jorgensen, W. L. *Journal of the American Chemical Society* **1998**, *120*, 9672.

(124) Koch, U.; Popelier, P. L. A. *The Journal of Physical Chemistry* **1995**, *99*, 9747.

(125) Wendler, K.; Thar, J.; Zahn, S.; Kirchner, B. *The Journal of Physical Chemistry A* **2010**, *114*, 9529.

(126) Hanson, D. R.; Lovejoy, E. R. *The Journal of Physical Chemistry A* **2006**, *110*, 9525.

(127) McClurg, R. B.; Flagan, R. C.; III, W. A. G. *The Journal of Chemical Physics* **1997**, *106*, 6675.

(128) McClurg, R. B. *The Journal of Chemical Physics* **1998**, *108*, 1748.

(129) Reiss, H.; Katz, J. L.; Cohen, E. R. *The Journal of Chemical Physics* **1968**, *48*, 5553.

(130) Zheng, J.; Hu, M.; Zhang, R.; Yue, D.; Wang, Z.; Guo, S.; Li, X.; Bohn, B.; Shao, M.; He, L.; Huang, X.; Wiedensohler, A.; Zhu, T. *Atmos. Chem. Phys. Discuss.* **2011**, *11*, 5019.

(131) Fan, J. W.; Zhang, R. Y.; Tao, W. K.; Mohr, K. I. *Journal of Geophysical Research-Atmospheres* **2008**, *113*, D08209.

(132) Fan, J. W.; Zhang, R. Y.; Li, G. H.; Tao, W. K. *Journal of Geophysical Research-Atmospheres* **2007**, *112*, D14204.

(133) Fan, J. W.; Zhang, R. Y.; Li, G. H.; Tao, W. K.; Li, X. W. *Journal of Geophysical Research-Atmospheres* **2007**, *112*, D04201.

(134) Zhang, R. Y.; Leu, M. T.; Keyser, L. F. *Geophysical Research Letters* **1995**, *22*, 1493.

(135) Zhang, R. Y.; Leu, M. T.; Keyser, L. F. *Journal of Physical Chemistry* **1996**, *100*, 339.

(136) Molina, M. J.; Zhang, R.; Wooldridge, P. J.; McMahon, J. R.; Kim, J. E.; Chang, H. Y.; Beyer, K. D. *Science* **1993**, *261*, 1418.

(137) Givan, A.; Larsen, L. A.; Loewenschuss, A.; Nielsen, C. J. *Journal of the Chemical Society, Faraday Transactions* **1998**, *94*, 827.

(138) Re, S.; Osamura, Y.; Morokuma, K. *The Journal of Physical Chemistry A* **1999**, *103*, 3535.

(139) Sugawara, S.; Yoshikawa, T.; Takayanagi, T.; Shiga, M.; Tachikawa, M. *The Journal of Physical Chemistry A* **2011**, *115*, 11486.

(140) Bandy, A. R.; Ianni, J. C. *The Journal of Physical Chemistry A* **1998**, *102*, 6533.

(141) Benson, D. R.; Erupe, M. E.; Lee, S. H. *Geophysical Research Letters* **2009**, *36*, L15818.

(142) Yu, F.; Wang, Z.; Luo, G.; Turco, R. *Atmos. Chem. Phys. Discuss.* **2007**, *7*, 13597.

(143) Nadykto, A. B.; Al Natsheh, A.; Yu, F.; Mikkelsen, K. V.; Ruuskanen, J. *Physical Review Letters* **2006**, *96*, 125701.

(144) Hazra, M. K.; Sinha, A. *Journal of the American Chemical Society* **2011**, *133*, 17444.

(145) Goken, E. G.; Castleman, A. W., Jr. *J. Geophys. Res.* **2010**, *115*, D16203.

(146) Bzdek, B. R.; Ridge, D. P.; Johnston, M. V. *Atmospheric Chemistry and Physics* **2010**, *10*, 3495.

(147) Bzdek, B. R.; Ridge, D. P.; Johnston, M. V. *Journal of Physical Chemistry A* **2010**, *114*, 11638.

(148) Bzdek, B. R.; Ridge, D. P.; Johnston, M. V. *Atmospheric Chemistry and Physics* **2011**, *11*, 8735.

(149) DePalma, J. W.; Bzdek, B. R.; Doren, D. J.; Johnston, M. V. *The Journal of Physical Chemistry A* **2011**, *116*, 1030.

(150) Erupe, M. E.; Viggiano, A. A.; Lee, S. H. *Atmos. Chem. Phys.* **2011**, *11*, 4767.

(151) Zollner, J. H.; Glasoe, W. A.; Panta, B.; Carlson, K. K.; McMurry, P. H.; Hanson, D. R. *Atmos. Chem. Phys.* **2012**, *12*, 4399.

(152) Hsieh, L. Y.; Kuo, S. C.; Chen, C. L.; Tsai, Y. I. *Atmospheric Environment* **2007**, *41*, 6648.

(153) Case, D. A.; Darden, T. A.; Cheatham, T. E.; Simmerling, C. L.; Wang, J.; Duke, R. E.; Luo, R.; Walker, R. C.; Zhang, W.; Merz, K. M.; Wang, B.; Hayik, S.; Roitberg, A.; Seabra, G.; Kolossvary, I.; Wong, K. F.; Paesani, F.; Vanicek, J.; Liu, J.; Wu, X.; Brozell, S. R.; Steinbrecher, T.; Gohlke, H.; Cai, Q.; Ye, X.; Hsieh, M. J.; Hornak, V.; Cui, G.; Roe, D. R.; Mathews, D. H.; Seetin, M. G.; Sagui, C.; Babin, V.; Luchko, T.; Gusarov, S.; Kovalenko, A.; Kollman, P. A.; Roberts, B. P. *Amber 11*; University of California, 2010.

(154) Wales, D. J.; Scheraga, H. A. *Science* **1999**, *285*, 1368.

(155) Zhan, L.; Chen, J. Z. Y.; Liu, W.-K. *Physical Review E* **2006**, *73*, 015701.

(156) Shanker, S.; Bandyopadhyay, P. *The Journal of Physical Chemistry A* **2011**, *115*, 11866.

(157) Wang, J.; Wang, W.; Kollmann, P.; Case, D. *Journal of Computational Chemistry* **2005**, *25*, 1157.

(158) Wang, J.; Wang, W.; Kollman, P. A.; Case, D. A. *Journal of Molecular Graphics and Modelling* **2006**, *25*, 247.

(159) Jorgensen, W. L.; Chandrasekhar, J.; Madura, J. D.; Impey, R. W.; Klein, M. L. *The Journal of Chemical Physics* **1983**, *79*, 926.

(160) Hanson, D. R.; Eisele, F. *The Journal of Physical Chemistry A* **2000**, *104*, 1715.

(161) Frisch, M. J.; Trucks, G. W.; Schlegel, H. B.; Scuseria, G. E.; Robb, M. A.; Cheeseman, J. R.; Scalmani, G.; Barone, V.; Mennucci, B.; Petersson, G. A.; Nakatsuji, H.; Caricato, M.; Li, X.; Hratchian, H. P.; Izmaylov, A. F.; Bloino, J.; Zheng, G.; Sonnenberg, J. L.; Hada, M.; Ehara, M.; Toyota, K.; Fukuda, R.; Hasegawa, J.; Ishida, M.; Nakajima, T.; Honda, Y.; Kitao, O.; Nakai, H.; Vreven, T.; Montgomery, J. A.; Peralta, J. E.; Ogliaro, F.; Bearpark, M.; Heyd, J. J.; Brothers, E.; Kudin, K. N.; Staroverov, V. N.; Kobayashi, R.; Normand, J.; Raghavachari, K.; Rendell, A.; Burant, J. C.; Iyengar, S. S.; Tomasi, J.; Cossi, M.; Rega, N.; Millam, J. M.; Klene, M.; Knox, J. E.; Cross, J. B.; Bakken, V.; Adamo, C.; Jaramillo, J.; Gomperts, R.; Stratmann, R. E.; Yazyev, O.; Austin, A. J.; Cammi, R.; Pomelli, C.; Ochterski, J. W.; Martin, R. L.; Morokuma, K.; Zakrzewski, V. G.; Voth, G. A.; Salvador, P.; Dannenberg, J. J.; Dapprich, S.; Daniels, A. D.; Farkas; Foresman, J. B.; Ortiz, J. V.; Cioslowski, J.; Fox, D. J. Gaussian 09 Revision B.01, http://gaussian.com/, 2009

(162) Ochterski, J., Thermochemistry in Gaussian, http://www.gaussian.com/g_whitepap/thermo.htm, 2000

(163) Temelso, B.; Morrell, T. E.; Shields, R. M.; Allodi, M. A.; Wood, E. K.; Kirschner, K. N.; Castonguay, T. C.; Archer, K. A.; Shields, G. C. *The Journal of Physical Chemistry A* **2012**, *116*, 2209.

(164) Schaftenaar, G.; Noordik, J. H. *J. Comput.-Aided Mol. Design* **2000**, *14*, 123.

(165) Maheshwary, S.; Patel, N.; Sathyamurthy, N.; Kulkarni, A. D.; Gadre, S. R. *The Journal of Physical Chemistry A* **2001**, *105*, 10525.

(166) Ge, X.; Wexler, A. S.; Clegg, S. L. *Atmospheric Environment* **2011**, *45*, 524.

(167) Lei, W. F.; Zhang, R. Y.; McGivern, W. S.; Derecskei-Kovacs, A.; North, S. W. *Chemical Physics Letters* **2000**, *326*, 109.

(168) Lei, W. F.; Zhang, R. Y.; McGivern, W. S.; Derecskei-Kovacs, A.; North, S. W. *Journal of Physical Chemistry A* **2001**, *105*, 471.

(169) Shen, X.; Zhao, Y.; Chen, Z.; Huang, D. *Atmospheric Environment* **2013**, *68*, 297.

(170) Zhao, J.; Zhang, R. Y.; Misawa, K.; Shibuya, K. *Journal of Photochemistry and Photobiology a-Chemistry* **2005**, *176*, 199.

(171) Wang, L.; Lal, V.; Khalizov, A. F.; Zhang, R. Y. *Environmental Science & Technology* **2010**, *44*, 2461.

(172) Qiu, C.; Wang, L.; Lal, V.; Khalizov, A. F.; Zhang, R. *Environmental Science & Technology* **2011**, *45*, 4748.

(173) Qiu, C.; Zhang, R. *Environmental Science & Technology* **2012**, *46*, 4474.

(174) Kulmala, M. *Science* **2003**, *302*, 1000.

(175) EPA *Environmental protection agency* **1996**, *EPA/600/P-95/001cF*.

(176) Doyle, G. J. *Journal of Chemical Physics* **1961**, *35*, 795.

(177) Hou, G.-L.; Lin, W.; Deng, S. H. M.; Zhang, J.; Zheng, W.-J.; Paesani, F.; Wang, X.-B. *The Journal of Physical Chemistry Letters* **2013**, *4*, 779.

(178) Weber, K. H.; Morales, F. J.; Tao, F.-M. *The Journal of Physical Chemistry A* **2012**, *116*, 11601.

(179) Kim, C. S.; Okuyama, K.; de la Mora, J. F. *Aerosol Science and Technology* **2004**, *38*.

(180) Ude, S.; de la Mora, J. F. *Journal of Aerosol Science* **2005**, *36*, 1224.

(181) Fortner, E. C.; Zhao, J.; Zhang, R. Y. *Analytical Chemistry* **2004**, *76*, 5436.

(182) Zheng, J.; Khalizov, A.; Wang, L.; Zhang, R. Y. *Analytical Chemistry* **2010**, *82*, 7302.

(183) Solomon, S. et al. IPCC Climate Change 2007: The Physical Science Basis (Cambridge Univ. Press, 2007).

(184) Iinuma, Y.; Boge, O.; Kahnt, A.; Herrmann, H. P*hysical Chemistry Chemical Physics* 2**009,** 1*1,* 7985.

(185) Surratt, J. D.; Chan, A. W. H.; Eddingsaas, N. C.; Chan, M. N.; Loza, C. L.; Kwan, A. J.; Hersey, S. P.; Flagan, R. C.; Wennberg, P. O.; Seinfeld, J. H. P*roceedings of the National Academy of Sciences of the United States of America* 2**010,** 1*07,* 6640.

(186) Lin, Y.-H.; Zhang, Z.; Docherty, K. S.; Zhang, H.; Budisulistiorini, S. H.; Rubitschun, C. L.; Shaw, S. L.; Knipping, E. M.; Edgerton, E. S.; Kleindienst, T. E.; Gold, A.; Surratt, J. D. E*nvironmental Science & Technology* 2**011,** 4*6,* 250.

(187) Paulot, F.; Crounse, J. D.; Kjaergaard, H. G.; Kürten, A.; St. Clair, J. M.; Seinfeld, J. H.; Wennberg, P. O. S*cience* 2**009,** 3*25,* 730.

(188) Elrod, M. J.; Minerath, E. C. E*nvironmental Science & Technology* 2**009,** 4*3,* 1386.

(189) Elrod, M. J.; Cole-Filipiak, N. C.; O'Connor, A. E. E*nvironmental Science & Technology* 2**010,** 4*4,* 6718.

(190) Darer, A. I.; Cole-Filipiak, N. C.; O'Connor, A. E.; Elrod, M. J. E*nvironmental Science & Technology* 2**011,** 4*5,* 1895.

(191) Lal, V.; Khalizov, A. F.; Lin, Y.; Galvan, M. D.; Connell, B. T.; Zhang, R. T*he Journal of Physical Chemistry A* 2**012.**

(192) Wang, T.; Liu, Z.; Wang, W.; Ge, M. A*tmospheric Environment* 2**012,** 5*6,* 58.

(193) Bleier, D. B.; Elrod, M. J. T*he Journal of Physical Chemistry A* 2**013.**

(194) Voisin, D.; Smith, J. N.; Sakurai, H.; McMurry, P. H.; Eisele, F. L. A*erosol Science and Technology* 2**003,** 3*7,* 471

(195) Minerath, E. C.; Casale, M. T.; Elrod, M. J. E*nvironmental Science & Technology* 2**008,** 4*2,* 4410.

(196) Lewis, E. R. J*ournal of Aerosol Science* 2**006,** 3*7,* 1605.

(197) Morrison, R.; Boyd, R. O*rganic Chemistry;* 6 ed.; Prentice Hall: Upper Saddle River, New Jersey, 1992.

(198) Clegg, S. L.; Qiu, C.; Zhang, R. A*tmospheric Environment* 2**013,** 7*3,* 145.